NTNU
Norwegian University of
Science and Technology

Nonlinear Laser-induced Deformations and Forces at Liquid-Liquid Interfaces near the critical Point.

Nina Sasaki Aanensen

Master of Science in Physics and Mathematics
Submission date: July 2011
Supervisor: Ingve Simonsen, IFY
Co-supervisor: Iver Brevik

Norwegian University of Science and Technology
Department of Physics

Abstract

The theory of laser-induced liquid-liquid interface deformation has been presented and used to derive a differential equation describing the shape of the deformation. The differential equation has been investigated and solved numerically, and the results have been compared to the experimental results of the Bordeaux group [24]. A model describing the maximum depth of the deformation based on the theory of a sphere in an electric field has also been investigated.

The deformations from the numerical solutions of the differential equation are too wide compared to the experimental results. The shoulder-shape that has been observed in the experiments is not present in the numerical solutions. There is reason to believe that the differential equation may be too simple in order to describe the liquid-liquid interface deformation for nonlinear cases. There may be thermal effects that changes the liquid properties due to local temperature variations induced by the laser, causing the liquid parameters to change along the deformation.

The model used to estimate the deformation depth does not give reasonable results, as it leads to a deformation that is more than 100 times larger than what is observed in the corresponding experiments. The assumptions made for this model may not be valid, and a discussion on what should be done in order to improve the model is included in this text.

Preface

After four and a half years of exploring the many subjects and sides of the world of Physics and Mathematics, there I was: Only one semester left before I could claim my M.Sc. degree and my life as a student would come to an end. In other words, the master thesis would perhaps be my last chance to solve integrals and work with heart breaking equations on full-time. It became apparent that the right man to ask for a suitable task was professor Iver Brevik. Reproducing highly nonlinear liquid-liquid interface deformations, that have been observed in experiments, from theory turned out to be just perfect, and sometimes almost more than what I asked for.

I would like to thank both my supervisors for this M.Sc. thesis: professor Iver Brevik at the Department of Energy and Process Engineering, and professor Ingve Simonsen at the Department of Physics. Iver, I have really enjoyed our weekly conversations and discussions on the many problems I have encountered. I have great respect for your knowledge and experience in almost every subject. Ingve, thank you for showing interest in my work and taking time to hear what I have to say, even the times when it has nothing to do with the thesis. I know that you have a lot more important work to do. There is no coincidence that so many students have asked you to be their supervisor. I hope to keep in touch with both of you in the years to come, and I wish you all the best.

Nina Sasaki Aanensen, Trondheim, July 2011.

Contents

List of Figures

List of Tables

Chapter 1

Introduction

The idea that light carries momentum goes back to Kepler and Newton, and this idea was later confirmed by Maxwell [1]. When the laser was invented, the momentum could finally be used for practical applications. Today, there is a wide range of research areas who use the laser pressure as an important laboratory tool, such as quantum optics, trapping of atoms and biological particles, deformation of single cells, manipulation of DNA, nanofabrication and microfluidic sorting [2].

In order to find new and improve existing applications, it is important not only to perform experiments, but also to fully understand the theory behind the experiments. This text will try to bring some of the laser radiation pressure theory closer to the corresponding experimental observations.

The Bordeaux group

At the University of Bordeaux (Centre National de la Recherche Scientifique, France), a group of scientists have performed experiments on liquid-liquid interface deformations induced by radiation pressure from a laser. By using a near-critical phase-separated liquid mixture, the surface tension becomes weak [17]. The result is that even moderate laser powers can lead to deformations of several tens of micrometers. Several types of experiments have been performed using this low surface tension system, including liquid bridge experiments [3], liquid optical fibre experiments [4], laser-related droplet (or jet) experiments [6], [5], [7] as well as linear and nonlinear liquid-liquid interface bending experiments (laser beam incoming from below) [24], [12], [17]. Many more articles and other publications than those mentioned here have been released on the work by the Bordeaux group.

Not all the observations and results that are found during these experiments have been completely understood, not to mention reproduced from theory. This present text will try to do just that; to describe some of the laser induced nonlinear liquid-liquid interface deformations that have been observed by Casner, Delville et al. But first, a short

description of this type of experiment will be given.

Description of the interface bending experiment

A more detailed description of this experiment can be found in Casner's doctoral thesis [24] (French), or [17]. A laser beam with assumed Gaussian intensity distribution is used to create the interface deformation. The intensity of the beam depends on the laser power, P, and the beam waist, ω_0 (characteristic beam width). The interface is made from two liquids with a difference in mass density, $\Delta\rho$, and refractive index Δn. The size of these differences can be adjusted by varying the temperature. The laser beam is placed below the two liquids, meaning that it will propagate from the medium with highest mass density (and lowest refractive index) to the less denser medium. Due to the radiation pressure from the laser beam, the interface will be bended downwards. The force from the surface tension and the buoyancy will try to counteract the force from the laser. Depending on the intensity of the laser beam (with given liquid mixture parameters), the shape of the liquid-liquid interface deformation can be divided into two types, linear and nonlinear deformation. The linear type occurs for low values of P. The linear deformation is not as deep as the nonlinear deformations, and the shape is simpler (see figure 1.1a and 1.1b). The system during this experiment is assumed to be stationary.

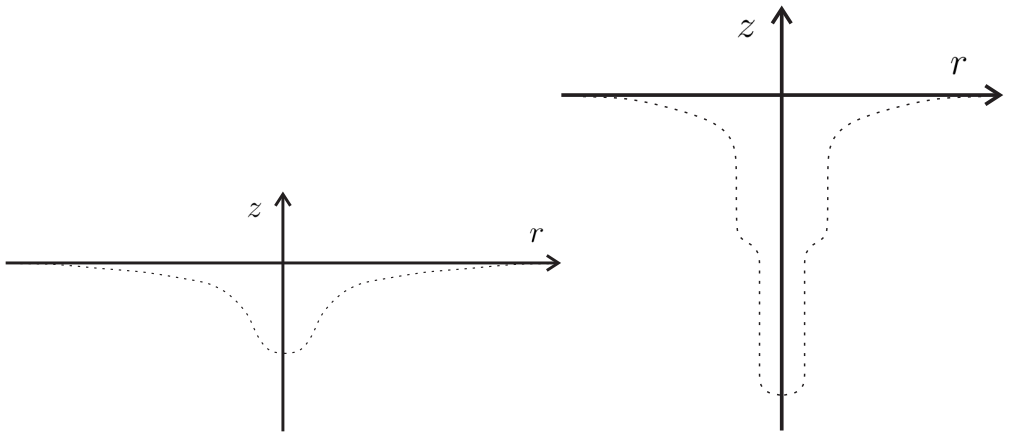

(a) Linear deformation

(b) Nonlinear deformation with "shoulder"

Figure 1.1: Figure showing qualitative sketches of linear and nonlinear liquid-liquid interface deformations. The nonlinear deformation is deeper and has a more complicated shape than linear deformations.

Theoretical description of the interface bending experiment

Several articles describing the theory of these experiments have been published. In 2002, Alex Casner delivered his doctoral thesis on the work of radiation pressure experiments. Among others, Iver Brevik, professor at the Norwegian University of Science and Technology, has later cooperated with the Bordeaux team in order to fully describe the theory behind the deformations [12], [17].

In 2003, Aslak Hallanger wrote his M.Sc. thesis [16] (with Iver Brevik as supervisor) about the linear and nonlinear liquid-liquid interface deformations. He was able to find a numerical solution to the differential equation that described the deformation, using the theoretical description of Brevik, Casner and Delville. The numerical results showed good agreement for the case of small deformations (low power P), but not for larger deformations. The solution did not fit the nonlinear shoulder-shaped deformations that has been observed for large laser power. Hallanger concluded that the differential equation (which is highly nonlinear) may have several solutions, and that he only found one of them. The numerical results of Hallanger have been reproduced several times [15], [8], but no one have obtained the shape of the nonlinear interface deformations.

The present text

In this text, the search for the shoulder-shaped nonlinear solution of the differential equation describing the interface deformation will continue. The focus will not only be on the computational calculations and the solution itself, but also to get some information from the differential equation before it is solved. As will be seen later, the differential equation is too complicated in order to be solved analytically, but it may be possible to simplify the equation for special cases, and perhaps make some analytical approximations. A discussion of the theoretical challenges with unknown parameters will also be included.

The second chapter contains a description of the different pressure forces that are involved in the liquid-liquid interface deformation system. First, each force will be presented separately and adjusted in order to be described by the shape of the deformation. Then, the forces will be put together in order to form a differential equation for the liquid-liquid interface deformation.

Chapter 3 includes some preparations for the numerical solving. The differential equation has to be made dimensionless and boundary conditions need to be found before the differential equation can be solved numerically. This chapter also contains a discussion of the nonlinear "shoulder" that have been observed in the Bordeaux experiments, and how this shape can be understood qualitatively from the differential equation and the forces involved. An attempt to predict the depth of the deformation from theory by using an adjusted model for spheres in an electromagnetic field is also included in this chapter.

The fourth chapter is called Numerical solution and contains some of the computational

calculations that have been performed during the semester (Spring, 2011). First, a trial solution will be put together from the analytical approximations achieved in chapter 3. Then, the attempts to solve the differential equation numerically will be presented parallel to error estimates of the input trial solution for each parameter set. By doing this, the hypothesis of Hallanger, that the shoulder-shape is an undiscovered solution to the differential equation, will be investigated further.

Lastly, a summary and the conclusions from each chapter will be presented and discussed shortly. Hopefully, some results will be achieved and certainly, some new questions will arise.

There are two appendices included in this text. The first contains some of the extensive and sometimes unpleasant calculations from chapter 2 and 3. The second contains the theory of the model used in chapter 3. This model was developed by Iver Brevik during the Spring 2011, and has not yet been investigated thoroughly or published.

Chapter 2

Theory

This chapter includes the theory of laser-induced liquid-liquid interface deformation. First, each force is presented separately. Then, they are rewritten and put together in order to form a differential equation that describes the shape of the deformation. The following theory is assumed to be valid for both linear and nonlinear stationary liquid-liquid interface deformations.

2.1 Buoyancy

The pressure inside a liquid depends on the mass density. If the pressure at a given height h_0 in the liquid is p_0, then the pressure at a height (or depth) h below h_0 is

$$p(h_0 + h) = p_0 + \rho g h, \tag{2.1}$$

where ρ is the mass density of the liquid and g is the gravitational acceleration (see figure 2.1). Note that h points in negative z-direction.

When a liquid-liquid system is under deformation, as is the case when the interface is illuminated by a laser, there will be a pressure difference between the inner and the outer medium (liquid) along the deformation due to the difference in mass density.

The pressure difference can be written as

$$\Delta p = (\rho_{out} - \rho_{in}) g h, \tag{2.2}$$

where ρ_{out} is the mass density of medium *out* and ρ_{in} is the mass density of medium in [24] (see figure 2.2). This force is often called the buoyancy and always points normal to the surface towards the medium of less mass density (medium in). The force is growing with larger h.

In the experiments performed by the Bordeaux group, the different parameters and liquid properties can be altered. For instance, the mass density difference $\Delta\rho = (\rho_{out} - \rho_{in})$ depends on the temperature difference $T - T_c$:

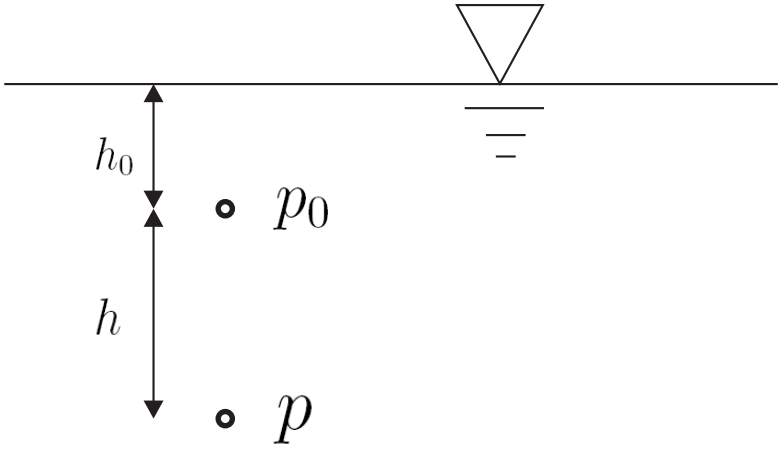

Figure 2.1: The pressure inside a liquid increases with the depth, h, by a factor ρg, where ρ is the mass density of the liquid and g is the gravitational acceleration.

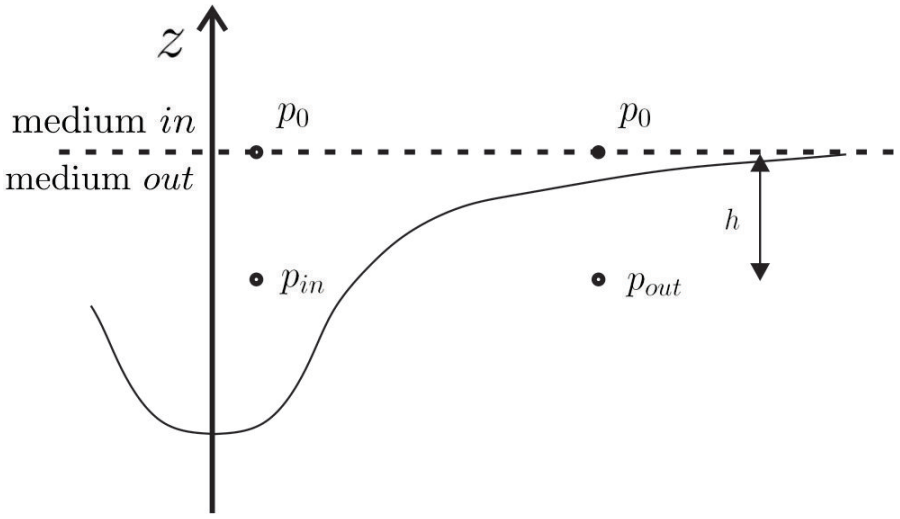

Figure 2.2: Under interface deformation, the pressure at a given height (or depth), h, below the surface is different inside and outside the deformation due to different mass densities.

$$\Delta\rho = (\Delta\rho)_0 \Big(\frac{T - T_c}{T}\Big)^{\beta}, \tag{2.3}$$

where the constant $(\Delta\rho)_0 = 285 \frac{\text{kg}}{\text{m}^3}$, $\beta = 0.325$, $T_c = 308.15$ K and T is the temperature of the system [24]. The temperature T_c is the critical temperature at which the surface tension goes to zero (the two liquids are the same). With $T - T_c$ varying from 1.5 – 25 K in the experiments of Casner and Delville [16], the difference in mass density $\Delta\rho$ varies

from 50 – 125 $\frac{\text{kg}}{\text{m}^3}$.

2.2 Surface tension

In addition to the buoyancy, the surface tension also plays an important role for the shape of the deformation. At liquid-liquid interfaces, the molecules of one liquid have only half as many neighbours of the same type as the molecules inside the liquid (the other half are molecules from the other liquid). The result is that the surface is in tension [9].

The surface tension depends on several parameters and on the properties of the two fluids involved. For instance, the surface tension at air-water interfaces is larger than for air-soap water. The two liquids in the Bordeaux group experiments are chosen such that the surface tension is small. By using two types of oil with low surface tension, it is possible to achieve nonlinear deformations with the use of moderate laser powers [17]. The surface tension is also dependent on temperature and the curvature of the surface. Surface tension can be expressed as a pressure difference:

$$\Delta p_{s.t.} = \sigma\Big(\frac{1}{R_1} + \frac{1}{R_2}\Big), \tag{2.4}$$

where σ is the coefficient of the surface tension in $\frac{\text{N}}{\text{m}}$, and R_1 and R_2 describes the shape of the deformation in meters (principal radii of curvature at a given point of the surface [16]). When there is no deformation of the surface, both R_1 and R_2 are infinitely large, and the pressure difference goes to zero.

The coefficient of surface tension σ is a function of the temperature [24]:

$$\sigma = \sigma_0\Big(\frac{T - T_c}{T_c}\Big)^{2\nu}. \tag{2.5}$$

Here, $\sigma_0 = 1.04 \cdot 10^{-4}\ \frac{\text{N}}{\text{m}}$ (dependent of the two liquids), $\nu = 0.63$ and $T_c = 308.15$ K [15]. As mentioned before, in the experiments of Casner and Delville, the temperature difference $T - T_c$ varies between 1.5 – 25.0 K [16].

The expression $\left(\frac{1}{R_1} + \frac{1}{R_2}\right)$ can be replaced by an expression of the height (or depth) of the deformation, h, the distance r from the laser beam center to a point on the interface and the corresponding angle of r, θ [17].

$$\frac{1}{R_1} + \frac{1}{R_2} = -\frac{1}{r}\frac{\partial}{\partial r}\left(\frac{r h_r}{\sqrt{1 + h_r^2 + \frac{1}{r}h_\theta^2}}\right) - \frac{1}{r}\frac{\partial}{\partial \theta}\left(\frac{h_\theta}{\sqrt{1 + h_r^2 + \frac{1}{r}h_\theta^2}}\right) \tag{2.6}$$

where $h_r \equiv \frac{\text{d}h}{\text{d}r}$ and $h_\theta \equiv \frac{\text{d}h}{\text{d}\theta}$. The system, both the incoming laser beam and the deformation, is assumed to be azimuthally symmetric. Therefore, $h_\theta = 0$ and equation

(2.6) can be simplified to:

$$\frac{1}{R_1} + \frac{1}{R_2} = -\frac{1}{r}\frac{\mathrm{d}}{\mathrm{d}r}\left(\frac{rh_r}{\sqrt{1+h_r^2}}\right). \tag{2.7}$$

Then, the pressure difference coming from the surface tension can be written as

$$\Delta p_{s.t.} = -\frac{\sigma}{r}\frac{\mathrm{d}}{\mathrm{d}r}\left(\frac{rh_r}{\sqrt{1+h_r^2}}\right). \tag{2.8}$$

2.3 Radiation force

Radiation force density

The force that causes the liquid-liquid deformation is the electromagnetic force from the laser beam. In order to find the magnitude of this force, the general expression of electromagnetic force per volume in an isotropic and non-conducting medium [17] will be the starting point:

$$\vec{f}_{e.m.} = -\frac{1}{2}\vec{E}^2\nabla\epsilon + \frac{1}{2}\nabla\big(E^2\rho(\frac{\partial\epsilon}{\partial\rho})_T\big) + \frac{\epsilon_r - 1}{c^2}\frac{\partial}{\partial t}(\vec{E}\times\vec{H}) \tag{2.9}$$

where $\vec{E}$ is the electric field vector, $\epsilon = \epsilon_0\epsilon_r$ is the permittivity, $\vec{H}$ is the magnetic field vector and ρ is the mass density of the medium.

The first term of equation (2.9) is called the Abraham-Minowski term [14], because it appears in both Abraham's and Minowski's formulation of the electromagnetic energy momentum tensor. This term is zero except where the permittivity changes, e.g. at liquid-liquid interfaces.

The second term of equation (2.9) represents electrostriction. The elastic deformation of a dielectric under the forces exerted by an electrostatic field is called electrostriction [10]. This force may or may not be detectable in real experiments depending on the circumstances. One important parameter is the speed of the sound. If the elastic pressure has enough time to build up, as is the case here, the electrostriction force is not detecable [13]. The electrostriction force can therefore be neglected.

The last term of equation (2.9) is called the Abraham term after Abraham's electromagnetic energy momentum tensor for isotropic, non-conducting bodies [14]. For optical frequencies, as are dealt with in the laser induced liquid-liquid interface deformation experiments, this term is not detectable (the frequencies are too high) [17]. In addition, stationary conditions are assumed.

This means that only the first term of equation (2.9), the Abraham-Minowski term re-

mains. Then, the electromagnetic force acting on the liquid-liquid surface is:

$$\vec{f}^{AM} = -\frac{1}{2}E^2\nabla\epsilon. \tag{2.10}$$

Here, $E = |\vec{E}|$ is the length of the electric field vector. The field vector can be expressed by two vector components, E_T and E_N, where E_T is the component of the electric field that is parallel to the surface and E_N is the component of the electric field that is normal to the surface. Then, $E^2 = E_T^2 + E_N^2$. The force only acts where there is a change in ϵ, i.e. at liquid-liquid interfaces, air-water interfaces etc. As can be seen from equation (2.10), the radiation force acts towards the medium with lower permittivity. In the Delville and Casner experiments, the upper fluid has the highest permittivity and the lowest mass density, ρ. This is different for the case of air-water interfaces, where the air (upper fluid) has both lowest density and permittivity. Notice also that the direction of the deformation does not depend on whether the incoming laser beam is propagating from below or above.

Radiation force per surface area

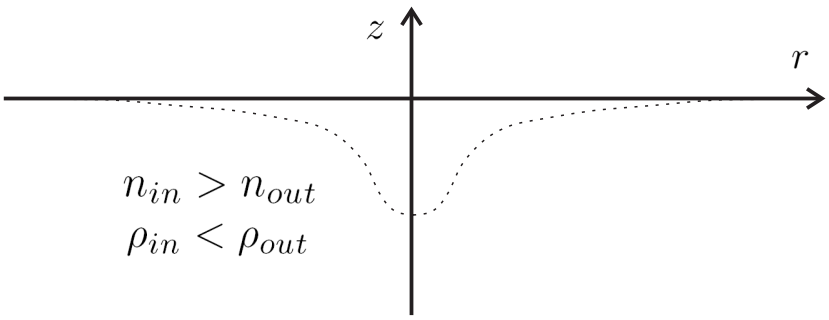

Figure 2.3: Figure showing the coordinate system used when integrating the radiation force per volume across the surface of the liquid-liquid interface. The undisturbed interface is located at $z = 0$. The inner medium (above) has lower mass density, but a larger refractive index. The laser beam comes from below, propagating in positive z-direction.

The next step towards finding the force balance causing the deformation of the liquid-liquid interface is to find the radiation force per surface area. In order to find the radiation force per area, $\vec{f}^{AM}$ can be integrated across the surface boundary from medium *out* to

medium in, with respect to the surface normal unit vector $\vec{n}$:

$$\begin{aligned}\sigma^{AM} &= \int_{-}^{+} f^{\vec{AM}}\,\mathrm{d}\vec{n} = -\int_{out}^{in}\frac{1}{2}E^2\frac{\mathrm{d}\epsilon}{\mathrm{d}n}\,\mathrm{d}n = -\frac{\epsilon_0}{2}\int_{out}^{in}(E_T^2+E_N^2)\,\mathrm{d}\epsilon_r \\ &= -\frac{\epsilon_0}{2}\int_{out}^{in}\Big[E_T^2+\frac{D_N^2}{\epsilon_0^2\epsilon_r^2}\Big]\,\mathrm{d}\epsilon_r = -\frac{\epsilon_0}{2}\Big[E_T^2\epsilon_r-\frac{D_N^2}{\epsilon_0^2\epsilon_r}\Big]_{out}^{in} \\ &= -\frac{\epsilon_0}{2}\Big[E_T^2(\epsilon_{rin}-\epsilon_{rout})+\frac{D_N^2}{\epsilon_0^2}(\frac{\epsilon_{rin}-\epsilon_{rout}}{\epsilon_{rin}\epsilon_{rout}})\Big] \\ &= -\frac{\epsilon_0}{2}(\epsilon_{rin}-\epsilon_{rout})\Big(E_T^2+\frac{D_N^2}{\epsilon_0^2\epsilon_{rin}\epsilon_{rout}}\Big)\end{aligned} \tag{2.11}$$

In medium in, D_N^2 can be written as $D_{Nin}^2 = \epsilon_0^2\epsilon_{rin}^2E_{Nin}^2$. Also, in a nonmagnetic medium, $n_i = \sqrt{\epsilon_{ri}\mu_{ri}} = \sqrt{\epsilon_{ri}}$. The indices n_{in} and n_{out} should not be confused with the surface normal vector $\vec{n}$. Then,

$$\begin{aligned}\sigma^{AM} &= -\frac{\epsilon_0}{2}(\epsilon_{rin}-\epsilon_{rout})\big(E_T^2+\frac{\epsilon_{rin}}{\epsilon_{rout}}E_N^2\big) \\ &= -\frac{\epsilon_0}{2}(n_{in}^2-n_{out}^2)\big(E_T^2+\frac{n_{in}^2}{n_{out}^2}E_N^2\big)\end{aligned} \tag{2.12}$$

Electric field components

Now, the radiation force per surface area is expressed as a function of the electric field components $\vec{E}_T$ and $\vec{E}_N$ in medium in. The goal is to set up a differential equation which describes the deformation of the liquid-liquid interface. Therefore, it will be more convenient to find the radiation force per surface area as a function of the variables describing the deformation itself in x-, y- and z-direction (see figure 2.4).

The electric field $\vec{E}$ in medium in can be decomposed into two other components than is used above. If $\vec{E}_\parallel$ is defined as the part of the electric field in the plane of incidence (the xz-plane) and $\vec{E}_\perp$ is the part of the electric field that is normal to the plane of incidence, then:

$$\begin{aligned}E_\parallel^2 &= E_x^2+E_z^2, \\ E_\perp^2 &= E_y^2.\end{aligned} \tag{2.13}$$

By using the geometry of the system as shown in figure 2.4 and figure 2.5, $\vec{E}_T$ and $\vec{E}_N$ can be rewritten as functions of the new components $\vec{E}_\parallel$ and $\vec{E}_\perp$. The angle θ_t is the angle of the transmitted beam relative to the surface normal.

$$\begin{aligned}E_T^2 &= E_\parallel^2\cos^2\theta_t + E_\perp^2 \\ E_N^2 &= E_\parallel^2\sin^2\theta_t\end{aligned} \tag{2.14}$$

Recalling Snell's law:

$$n_{out}\sin\theta_i = n_{in}\sin\theta_t, \tag{2.15}$$

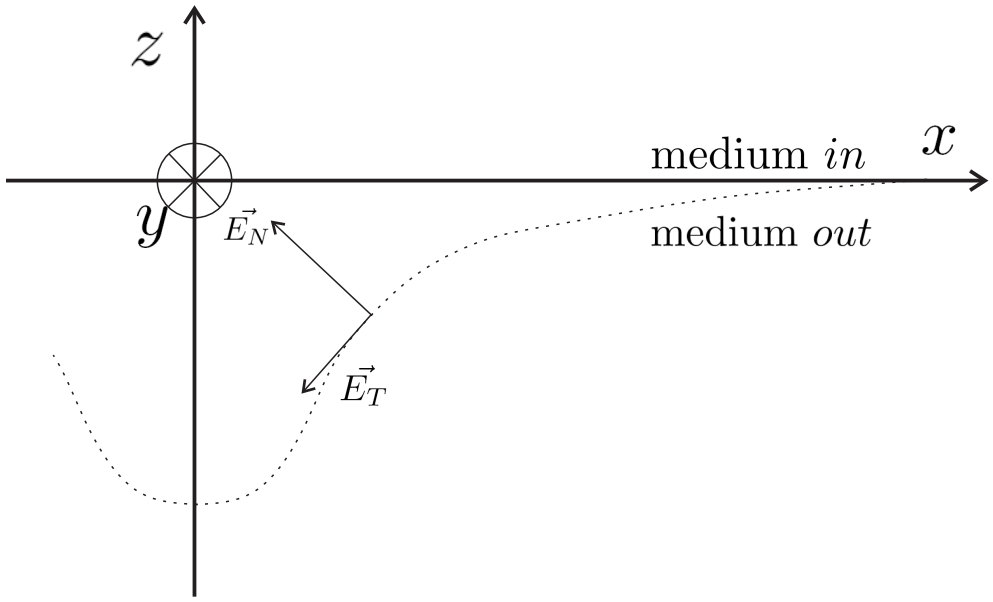

Figure 2.4: The electric field components $\vec{E}_T$ and $\vec{E}_N$ shown in a cartesian coordinate system. The field component $\vec{E}_T$ is the part of the electric field $\vec{E}$ that is parallel to the surface and $\vec{E}_N$ is the part of $\vec{E}$ that is normal to the surface.

with θ_i being the angle of the incoming laser beam relative to the surface normal, the radiation pressure force per area from equation (2.12) can then be written as:

$$\begin{aligned}\sigma^{AM} &= -\frac{\epsilon_0}{2}(n_{in}^2 - n_{out}^2)\Big[E_\parallel^2 \cos^2\theta_t + E_\perp^2 + \Big(\frac{n_{in}}{n_{out}}\Big)^2 E_\parallel^2 \sin^2\theta_t\Big] \\ &= -\frac{\epsilon_0}{2}(n_{in}^2 - n_{out}^2)\big[(\cos^2\theta_t + \sin^2\theta_i)E_\parallel^2 + E_\perp^2\big].\end{aligned} \tag{2.16}$$

The next step is to replace $E_\parallel$ and $E_\perp$ with more convenient variables which describe the shape of the deformation. The components $E_\parallel$ and $E_\perp$ describe the electric field in medium *in*. However, when performing experiments, it is actually the incoming electric field that is known. From Stratton [10], the energy transmission coefficients of the electric field are:

$$T_\perp = \frac{n_{in}}{n_{out}}\frac{\cos\theta_t}{\cos\theta_i}\Big(\frac{E_\perp^{(t)}}{E_\perp^{(i)}}\Big)^2 = \frac{\sin(2\theta_i)sin(2\theta_t)}{\sin^2(\theta_i+\theta_t)} \tag{2.17}$$

and

$$T_\parallel = \frac{n_{in}}{n_{out}}\frac{\cos\theta_t}{\cos\theta_i}\Big(\frac{E_\parallel^{(t)}}{E_\parallel^{(i)}}\Big)^2 = \frac{\sin(2\theta_i)sin(2\theta_t)}{\sin^2(\theta_i+\theta_t)\cos^2(\theta_i-\theta_t)}. \tag{2.18}$$

As with the electric field components, $T_\parallel$ represents the transmission coefficient in the case when the incoming electric field is lying in the plane of incidence, whereas $T_\perp$ is

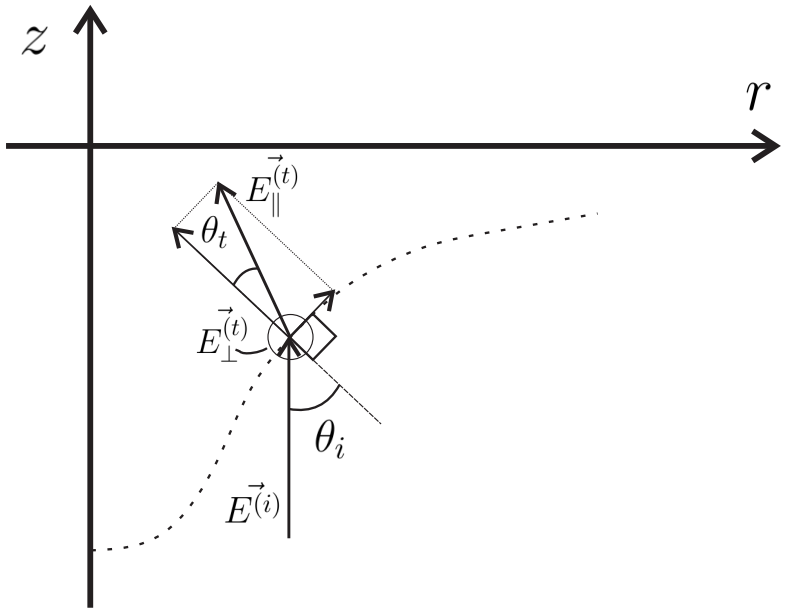

Figure 2.5: The electric field components E_T and E_N relative to the components $E_{\parallel}$ and $E_{\perp}$.

the transmission coefficient for case when the incoming electric field is perpendicular to the plane of incidence. The superscripts (i) and (t) denotes the incoming electric field and the transmitted electric field, respectively. Let a be an expression for the relation between the two refractive indices, $a \equiv \frac{n_{out}}{n_{in}}$. Using this definition and the rules for cosine and sine, the last terms of equation (2.17) and (2.18) can be rewritten as:

$$T_{\parallel} = 4a \frac{\cos\theta_i \cos\theta_t}{(\cos\theta_t + a\cos\theta_i)^2(\cos\theta_i\cos\theta_t + a\sin^2\theta_i)^2} \tag{2.19}$$

and

$$T_{\perp} = 4a \frac{\cos\theta_i \cos\theta_t}{(\cos\theta_t + a\cos\theta_i)^2}. \tag{2.20}$$

Moreover, $E_{\perp}$ and $E_{\parallel}$ can be expressed as

$$E_{\perp}^2 = \frac{n_{out}}{n_{in}} \frac{\cos\theta_i}{\cos\theta_t} T_{\perp} E_{\perp}^{(i)2}, \quad E_{\perp}^{(i)2} = E^{(i)2}\sin^2\alpha \tag{2.21}$$

and

$$E_{\parallel}^2 = \frac{n_{out}}{n_{in}} \frac{\cos\theta_i}{\cos\theta_t} T_{\parallel} E_{\parallel}^{(i)2}, \quad E_{\parallel}^{(i)2} = E^{(i)2}\cos^2\alpha, \tag{2.22}$$

where α is the angle between the incoming electric field vector $\vec{E}^{(i)}$ and the plane of incidence (see figure 2.6). With these new expressions, the radiation force per surface

area from equation (2.16) can be rewritten to:

$$\begin{aligned}\sigma^{AM} &= -\frac{\epsilon_0}{2}(n_{in}^2 - n_{out}^2)\left[(\cos^2\theta_t + \sin^2\theta_i)T_{\parallel}\cos^2\alpha + T_{\perp}\sin^2\alpha\right]\frac{n_{out}}{n_{in}}\frac{\cos\theta_i}{\cos\theta_t}E^{(i)2} \\ &= -\frac{\epsilon_0 E^{(i)2}}{2}\frac{(n_{in}^2 - n_{out}^2)}{n_{in}}n_{out}\frac{\cos\theta_i}{\cos\theta_t}\left[(\cos^2\theta_t + \sin^2\theta_i)T_{\parallel}\cos^2\alpha + T_{\perp}\sin^2\alpha\right]. \quad (2.23)\end{aligned}$$

Now, the radiation force per surface area σ^{AM} is given as a function of the incoming electric field and the angles of the system.

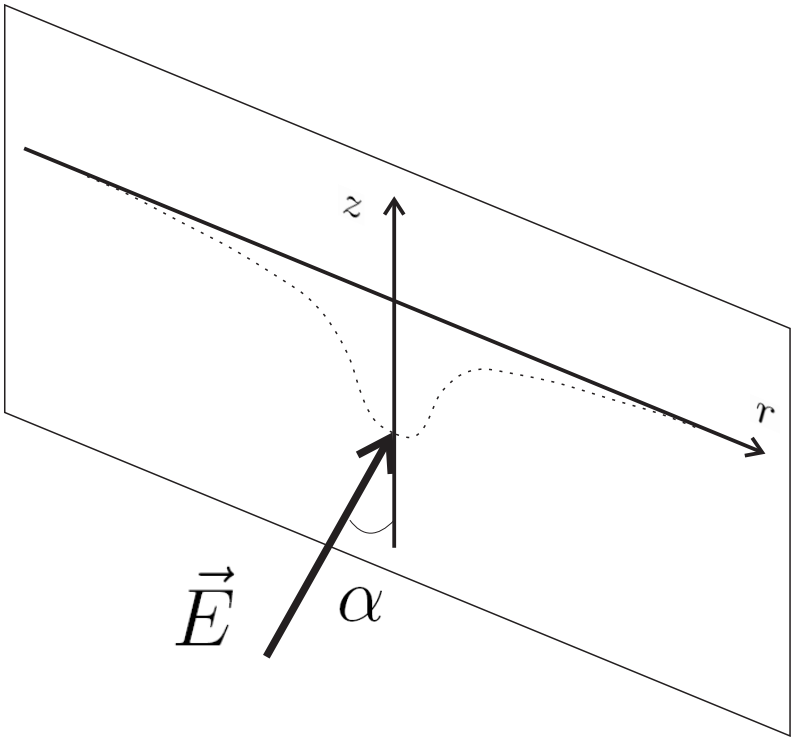

Figure 2.6: Figure showing the angle α between the incoming electric field and the plane of incidence.

The laser beam intensity

The intensity I of a monochromatic wave (as is the case for the incoming laser beam) is given by [11]:

$$I = \epsilon_0 nc\langle E^2\rangle. \quad (2.24)$$

This means that the modulus of the incoming electric field can be written as

$$E^{(i)2} = \frac{I}{\epsilon_0 n_{out} c}. \quad (2.25)$$

Inserting this into equation (2.23) results in a new expression for the radiation force per surface area σ^{AM}:

$$\sigma^{AM} = -\frac{I}{2c}\frac{n_{in}^2 - n_{out}^2}{n_{in}}\frac{\cos\theta_i}{\cos\theta_t}\left[(\cos^2\theta_t + \sin^2\theta_i)T_{\parallel}\cos^2\alpha + T_{\perp}\sin^2\alpha\right] \tag{2.26}$$

The intensity is assumed to be Gaussian and circularly polarised, i.e. azimuthally symmetric. It is also assumed to be independent of z, as the deformations of Casner and Delville are not more than about 80 μm for laser powers P up to 1 200 mW [16]. The intensity then reduces to a function of the radius r [17]:

$$I(r,z) = I(r) = \frac{2P}{\pi\omega_0^2}e^{-\frac{2r^2}{w_0^2}} \tag{2.27}$$

where P is the power of the laser and ω_0 is the laser beam waist. Typical values for P in the Casner and Delville experiments that give nonlinear deformations are P: 300 – 1 200 mW [16]. The beam waist ω_0 of the laser is from a couple of microns to some tens of microns.

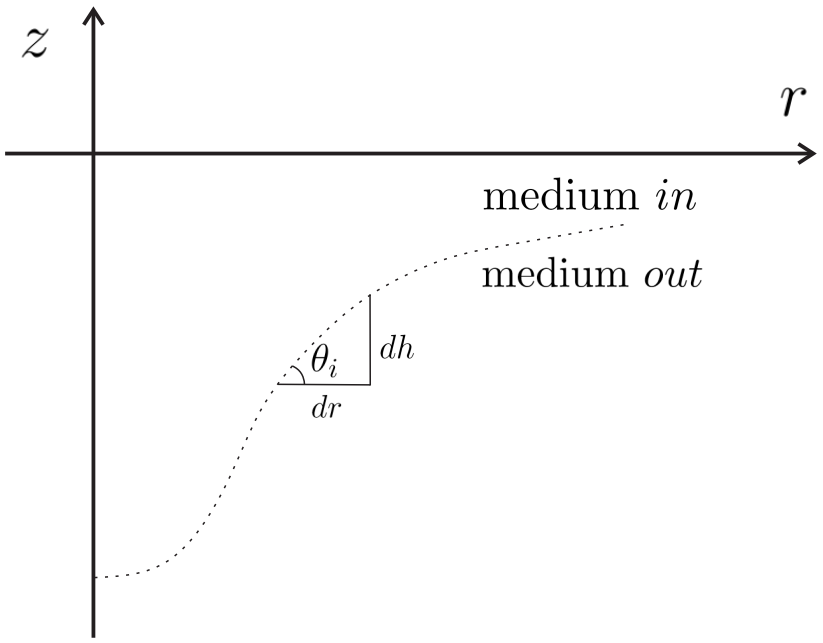

Figure 2.7: Figure showing how the expressions for $\cos\theta_i$ and $\sin\theta_i$ can be replaced with expressions for the shape of the deformation. the height (or depth), h, is pointing in negative z-direction.

Equation (2.26) contains the angles θ_i and θ_t. By using the geometry of the system, as

can be seen in figure 2.7, $\cos\theta_i$ and $\sin\theta_i$ can be written as:

$$\cos\theta_i = \frac{1}{\sqrt{1+h_r^2}} \qquad \sin\theta_i = \frac{h_r}{\sqrt{1+h_r^2}}. \tag{2.28}$$

Expressions for $\cos\theta_t$ and $\sin\theta_t$ can also be achieved by using Snell's law and that $\sin^2\theta_t + \cos^2\theta_t = 1$.

$$\sin\theta_t = \frac{ah_r}{\sqrt{1+h_r^2}} \qquad \cos\theta_t = \frac{\sqrt{1+h_r^2(1-a^2)}}{\sqrt{1+h_r^2}}. \tag{2.29}$$

Inserting the expressions for $T_\parallel$ and $T_\perp$ from equation (2.19) and (2.20) in addition to the expressions for the angles, the radiation pressure force per surface area from equation (2.26) can be expressed as a function of a, h_r and α:

$$\begin{aligned}
\sigma^{AM} &= -\frac{I}{2c}\frac{n_{in}^2 - n_{out}^2}{n_{in}}\frac{\cos\theta_i}{\cos\theta_t}\Big[(\cos^2\theta_t + \sin^2\theta_i)T_\parallel\cos^2\alpha + T_\perp\sin^2\alpha\Big] \\
&= -\frac{I}{2c}\frac{n_{in}^2 - n_{out}^2}{n_{in}}\frac{4a\cos^2\theta_i}{(\cos\theta_t + a\cos\theta_i)^2}\left[\frac{\cos^2\theta_t + \sin^2\theta_i}{(\cos\theta_i\cos\theta_t + \sin\theta_i\sin\theta_t)^2}\cos^2\alpha + \sin^2\alpha\right] \\
&= -\frac{2I}{c}\frac{n_{in}^2 - n_{out}^2}{n_{in}^2}\frac{n_{out}}{\left(a+\sqrt{1+h_r^2(1-a^2)}\right)^2}\times \\
&\times\left[\frac{1+(3-a^2)h_r^2+(2-a^2)h_r^4}{\left(ah_r^2+\sqrt{1+h_r^2(1-a^2)}\right)^2}\cos^2\alpha + \sin^2\alpha\right]
\end{aligned} \tag{2.30}$$

For a full calculation of equation (2.30), see appendix A. To simplify the expression above, f can be defined as a function of a, h_r and α:

$$f(a,h_r,\alpha) = \frac{(1+a)^2}{\left(a+\sqrt{1+h_r^2(1-a^2)}\right)^2}\left[\frac{1+(3-a^2)h_r^2+(2-a^2)h_r^4}{\left(ah_r^2+\sqrt{1+h_r^2(1-a^2)}\right)^2}\cos^2\alpha + \sin^2\alpha\right]. \tag{2.31}$$

Then, the radiation force per surface area σ^{AM} can be written as:

$$\sigma^{AM} = -\frac{2I}{c}\Big(\frac{n_{in}-n_{out}}{n_{in}+n_{out}}\Big)n_{out}f(a,h_r,\alpha) \tag{2.32}$$

As mentioned before, the laser beam is assumed to be circularly polarised. The angle α depends on the polarisation of the incoming laser beam. With circular polarisation, $\cos\alpha$ and $\sin\alpha$ can be averaged over α.

$$\langle\cos^2\alpha\rangle = \langle\sin^2\alpha\rangle = \frac{1}{2} \tag{2.33}$$

This reduces the function $f(a,h_r,\alpha)$ from equation (2.31) to a function of only two variables:

$$f(a,h_r) = \frac{(1+a)^2\Big[1+(2-a^2)h_r^2+h_r^4+ah_r^2\sqrt{1+h_r^2(1-a^2)}\Big]}{\left(a+\sqrt{1+h_r^2(1-a^2)}\right)^2\left(ah_r^2+\sqrt{1+h_r(1-a^2)}\right)^2} \tag{2.34}$$

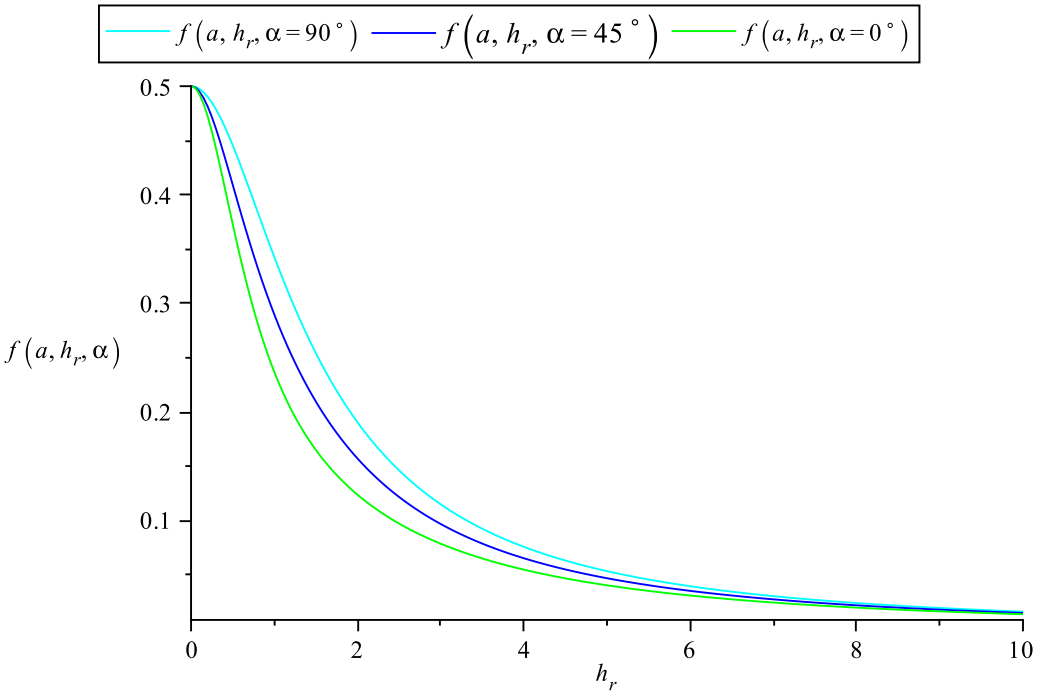

Figure 2.8: The function $f(a, h_r, \alpha)$ as a function of h_r. The angle α between the incoming electric field and the plane of incidence is varying from 0° to 90°. The constant a is 0.996 for all three cases.

The full calculation from equation (2.31) to (2.34) can be found in appendix A.

Comment: What if the laser beam is not circularly polarised? How much will the function $f(a, h_r, \alpha)$ change if α is not 45°? Figure 2.8 shows the function $f(a, h_r, \alpha)$ as a function of h_r, with three different values of α, namely 0°, 45° and 90°. The constant a is set to 0.996, which is a reasonable value for $T - T_c \approx 2.5$ K (see discussion in section 3.4). As can be seen from figure 2.8, the function $f(a, h_r, \alpha)$ the regions of $h_r \ll 1$ and $h_r > 7$ are not depending on the value of α. The middle region (h_r from 0.25 to 6), however, is varying more as α changes.

Comment: What if the system is not stationary? Only stationary liquid-liquid interface deformations will be discussed in this present text. But also non-stationary experiments have been performed by the Bordeaux team (see for instance Casner's Ph.D. thesis [24]). Then, a laser beam pulse is used to give non-stationary deformations. The intensity changes from $I(r)$ to $I(r, t) = I(r) \cdot I(t)$, it becomes time-dependent. With varying intensity, the radiation force will change with time, and so will the deformation. For further reading see, for instance, [16], [19] or [24].

2.4 Putting the differential equation together

Now, the three forces that play an important role in the case of deforming liquid-liquid interfaces with a laser beam have been presented. It is time to put the force terms together in order to find a differential equation that describes the deformation. The next step will be to solve the differential equation assuming nonlinear conditions, i.e. for large incoming laser powers P, small beam waists ω_0 and near critical liquid conditions ($T - T_c$ small).

It is important to keep in mind that the coordinate system that is used has z pointing upwards from medium *out* to medium *in*, whereas the height of the deformation, h, is pointing downwards. This has to be taken into account when balancing the forces.

The right hand side of the differential equation

The radiation force from the laser beam is causing the deformation. Without this force, h would be equal to zero for all r. Since medium *out* has a lower permittivity than medium *in*, this force will act along the surface normal towards medium *out*. The intensity is assumed to have a Gaussian distribution, which means that the force will be stronger for low r-values, hence larger deformations.

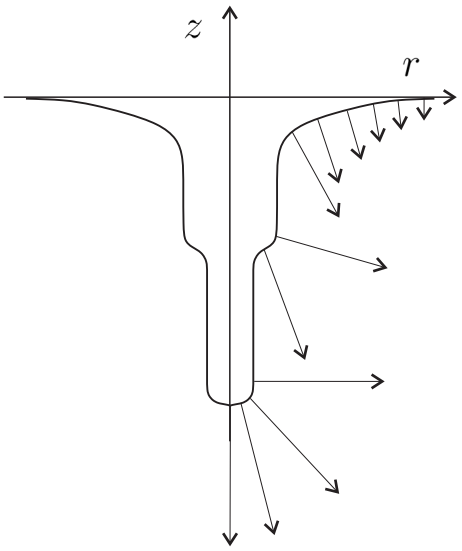

Figure 2.9: Qualitative sketch of the laser force acting on the surface under non-linear deformation. The intensity of the laser beam is assumed to have a Gaussian distribution with respect to the radius r. This means that the force from the laser beam is larger for smaller values of r. When r goes to infinity, the force from the laser beam goes to zero. The direction of the laser beam force is outwards from medium *in* to medium *out* because $n_{in} > n_{out}$.

The left hand side of the differential equation

The two other forces, namely the buoyancy and the surface tension will (in principal, but this turns out to be more complicated for nonlinear cases) try to counterbalance the force from the laser beam.

The buoyancy term is larger for increasing h, or for more negative z-values. It points inwards, from medium *out* to medium *in*, due to a denser medium *out* ($\rho_{out} > \rho_{in}$). A qualitative sketch can be seen in figure 2.10.

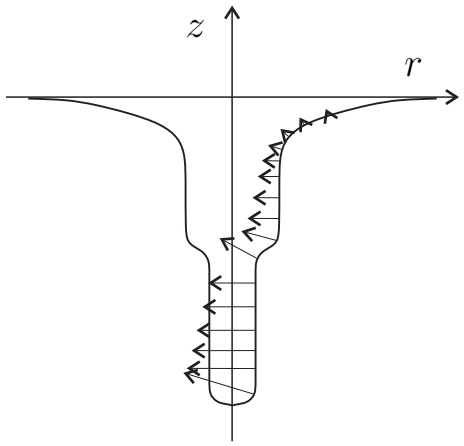

Figure 2.10: Qualitative sketch of the buoyancy force acting on the surface under nonlinear deformation. The buoyancy increases linearly with larger values of h (more negative z-values). The direction of the force is inwards, from medium *out* to medium *in*.

The surface tension is directed towards medium *in* when the surface is convex and towards medium *out* when the surface is concave, as can be seen in figure 2.11. Putting all this

Figure 2.11: Qualitative sketch of the surface tension direction depending on the shape of the surface.

together with the laser pressure force on the right hand side and the other two on the left hand side of the equation results in

$$(\rho_{out} - \rho_{in})h - \frac{\sigma}{r}\frac{\mathrm{d}}{\mathrm{d}r}\Big(\frac{rh_r}{\sqrt{1+h_r^2}}\Big) = -\frac{2I}{c}\Big(\frac{n_{in}-n_{out}}{n_{in}+n_{out}}\Big)n_{out}f(a,h_r). \tag{2.35}$$

Equation (2.35) is the differential equation describing the deformation of a liquid-liquid interface under illumination of an incoming laser beam. The system is assumed to be cylindrical symmetric and stationary with a Gaussian laser beam intensity distribution.

2.5 Changing the free variable

One of the challenges when Hallanger solved this equation in his M.Sc. thesis [16] was that h_r grew to infinity in the middle region of r for high laser powers P. This may be one of the reasons why Hallanger was not able to find shoulder-shape solutions of the differential equation for nonlinear cases. To avoid numerical problems when h_r goes to infinity, an attempt will be made to solve the differential equation with respect to r. In other words,

$$h(r) \to h \qquad r \to r(h). \tag{2.36}$$

Then, the derivative of h with respect to r, h_r, can be expressed differently.

$$h_r = \frac{1}{\mathrm{d}r/\mathrm{d}h} = \frac{1}{r_h} \tag{2.37}$$

Instead of h_r growing to infinity in some of the middle region, there are now regions where r_h is zero. This should eliminate the numerical difficulties of infinite values when solving the differential equation. The free variable is now h, and the differential equation must be rewritten so it can be solved with respect to r. Inserting this change into equation (2.34) results in

$$f(a,h_r) \to f(a,r_h) = \frac{(1+a)^2 r_h^4 \left[r_h^4 + (2-a^2)r_h^2 - a r_h \sqrt{(r_h^2+1-a^2)} + 1\right]}{\left(a r_h^2 - r_h\sqrt{(r_h^2+1-a^2)}\right)^2 \left(a - r_h\sqrt{(r_h^2+1-a^2)}\right)^2}. \tag{2.38}$$

The full calculation from $f(a,h_r)$ to $f(a,r_h)$ in equation (2.38) can be found in appendix A. By changing the free variable on the left hand side of the differential equation, the new left hand side becomes

$$\begin{aligned} &\Delta\rho g h - \frac{\sigma}{r}\frac{\mathrm{d}}{\mathrm{d}r}\Big(\frac{r h_r}{\sqrt{1+h_r^2}}\Big) \\ &= \Delta\rho g h - \frac{\sigma}{r\sqrt{r_h^2+1}} - \frac{2\sigma r_{hh}}{(r_h^2+1)^{\frac{3}{2}}}. \end{aligned} \tag{2.39}$$

Also this calculation can be found in appendix A. Combining equation (2.38) and (2.39) gives the differential equation for $r(h)$.

$$\Delta\rho g h - \frac{\sigma}{r\sqrt{r_h^2+1}} - \frac{2\sigma r_{hh}}{(r_h^2+1)^{\frac{3}{2}}} = -\frac{2I}{c}\frac{n_{in}-n_{out}}{n_{in}+n_{out}} n_{out} f(a,r_h) \tag{2.40}$$

Equation (2.40) is the differential equation for the surface deformation of a liquid-liquid interface that will be tried solved in order to match the shape of the deformations in

the experiments of Delville et al. The focus will be on the nonlinear deformations, that occurs at $P > 300\ \mu m$ [24]. The shoulder-shape of these nonlinear deformations has not yet been reproduced from theory.

Due to the complexity of the differential equation (2.40), no attempt will be made in order to solve it analytically. Before trying to solve it numerically, a couple of adjustments need to be made. The differential equation must be made dimensionless, and the boundary conditions may require some further adjustments. This will be discussed in the next chapter.

Chapter 3

Analysis of the differential equation

This chapter contains further investigations on the differential equation for the liquid-liquid system. The differential equation needs some adjustments before it can be solved numerically with a computer. Also, by studying the different elements of the equation, some information can be obtained directly without needing to solve it. Discussions on the boundary values, the challenges with unknown parameters and the difference between linear and nonlinear deformations are also included in this chapter.

3.1 Dimensionless equation

The first step towards solving the differential equation numerically is to make the variables and the parameters dimensionless. This can be achieved by introducing two new dimensionless variables to replace the radius r and the height h:

$$R = \frac{r}{\omega_0} \qquad H = \frac{h}{l_c}, \tag{3.1}$$

where $l_c = \sqrt{\sigma/(g\Delta\rho)}$ is the capillary length and ω_0 is the beam waist of the incoming laser beam. The dimensionless variables R and H are the same as used by Hallanger, Brevik, Haaland and Sollie [15]. Inserting these two dimensionless variables into equation (2.40) results in a new expression for the left hand side of the differential equation.

$$\begin{aligned} &\Delta\rho g h - \frac{\sigma}{r\sqrt{r_h^2+1}} - \frac{2\sigma r_{hh}}{(r_h^2+1)^{\frac{3}{2}}} \\ &= \frac{\sigma l_c}{\omega_0^2} \cdot \Big[B_0 H - \frac{1}{R\sqrt{R_H^2 + \frac{1}{B_0}}} - \frac{2R_{HH}}{(R_H^2 + \frac{1}{B_0})^{\frac{3}{2}}} \Big] \end{aligned} \tag{3.2}$$

Here, the Bond number $B_0 \equiv (\omega_0/l_c)^2$ has been introduced. Replacing r_h in the function $f(a, r_h)$ gives:

$$\begin{aligned} f(a, r_h) &= \frac{(1+a^2)r_h^4\left[r_h^4 + (2-a^2)r_h^2 - ar_h\sqrt{(r_h^2+1-a^2)} + 1\right]}{\left(ar_h^2 - r_h\sqrt{(r_h^2+1-a^2)}\right)^2\left(a - r_h\sqrt{(r_h^2+1-a^2)}\right)^2} \\ &= \frac{(1+a^2)\frac{1}{B_0}R_H^4\left[B_0^2R_H^4 + (2-a^2)B_0R_H^2 - aB_0R_H\sqrt{\left(R_H^2 + \frac{(1-a^2)}{B_0}\right)} + 1\right]}{\left(aR_H^2 - R_H\sqrt{\left(R_H^2 + \frac{(1-a^2)}{B_0}\right)}\right)^2\left(\frac{a}{B_0} - R_H\sqrt{\left(R_H^2 + \frac{(1-a^2)}{B_0}\right)}\right)^2} \\ &= f(a, B_0, R_H) \end{aligned} \tag{3.3}$$

The full calculation is presented in appendix A. For convenience, a new function $f'(a, B_0, R_H)$ is introduced as:

$$f'(a, B_0, R_H) = B_0 f(a, B_0, R_H). \tag{3.4}$$

Using this new function $f'(a, B_0, R_H)$ together with the rest of the radiation pressure force results in a new expression for the right hand side of the differential equation:

$$\sigma^{AM} = -\frac{2I}{cB_0}\frac{n_{in} - n_{out}}{n_{in} + n_{out}} n_{out} f'(a, B_0, R_H), \tag{3.5}$$

with $f('a, B_0, R_H)$ given in equation (3.4). Then, the dimensionless differential equation with the gravity force and the surface tension force on the left hand side and the radiation pressure force on the right hand side yields

$$B_0 H - \frac{1}{R\sqrt{R_H^2 + \frac{1}{B_0}}} - \frac{2R_{HH}}{(R_H^2 + \frac{1}{B_0})^{\frac{3}{2}}} = -\frac{AN}{B_0} e^{-2R^2} f'(a, B_0, R_H). \tag{3.6}$$

Here, $A \equiv \frac{4P}{\pi c \sigma l_c}$ and $N \equiv \left(\frac{n_{in}-n_{out}}{n_{in}+n_{out}}\right) n_{out}$ is used to simplify the equation.

3.2 Boundary conditions

The boundary conditions of the differential equation in (3.6) has not yet been discussed. Therefore, the next step is to determine the boundary conditions of the system. The boundary conditions can be found both by studying the experimental results of the Bordeaux group and by studying the force terms from theory. The two boundaries correspond to R (or r) $\to 0$ and $R \to \infty$.

The boundary at $R \to \infty$

It is the laser beam that is causing the deformation of the liquid-liquid interface. Without it, the deformation height H would be zero for all R. The laser beam intensity distribution is assumed to be Gaussian, and is therefore stronger for low values of R. As R grows

to infinity, the intensity goes to zero (zero intensity corresponds to no laser beam). In other words, $H \to 0$. Since there is no change in the height H for large R-values, also $H_R \to 0$. In short we therefore have:

$$\lim_{R\to\infty} H = 0, \quad \lim_{R\to\infty} H_R = 0. \tag{3.7}$$

The last condition in (3.7) can be rewritten as:

$$\lim_{R\to\infty} (R_H)^2 = \lim_{R\to\infty} \Big(\frac{1}{H_R}\Big)^2 = \infty \tag{3.8}$$

Starting from equation (2.35), an analytical approximation for this region will be searched for. As R grows, H_R becomes smaller and smaller. Therefore, H_R^2 (and h_r^2) will be assumed to be even smaller and set to zero. On the right hand side of (2.35), the term $\exp(-2r^2/\omega_0^2)$ in the expression for the intensity will bring the whole right hand side to zero:

$$\begin{aligned}
\lim_{r\to\infty} \quad \Delta\rho g h - \frac{\sigma}{r}\frac{\mathrm{d}}{\mathrm{d}r}\Big(\frac{r h_r}{\sqrt{1+h_r^2}}\Big) &= -\frac{2I}{c}\Big(\frac{n_{in}-n_{out}}{n_{in}+n_{out}}\Big) n_{out} f(a, h_r) \\
\Delta\rho g h - \frac{\sigma}{r}\frac{\mathrm{d}}{\mathrm{d}r}(r h_r) &= 0 \\
B_0 H - \frac{1}{R}\frac{\mathrm{d}}{\mathrm{d}R}(R H_R) &= 0 \\
B_0 H - \frac{H_R}{R} - H_{RR} &= 0.
\end{aligned} \tag{3.9}$$

The differential equation in (3.9) is known as the modified Bessel's differential equation. The general solution to equation (3.9) is

$$H(R) = c_1 I_0(\sqrt{B_0}R) + c_2 K_0(\sqrt{B_0}R), \tag{3.10}$$

where c_1 and c_2 are constants and I_0 and K_0 are the 0th order of modified Bessel function, first and second type, respectively. The modified Bessel function of second type, $K_n(x)$ is also known as the Basset function. Since $H \to 0$ as $R \to \infty$, only the Basset function, and not the first type of the modified Bessel function, is interesting, as this converges to 0 for large R-values. For large values of R:

$$H(R) = c_2 K_0(\sqrt{B_0}R), \tag{3.11}$$

and the constant c_2 needs to be found. If the differential equation (3.6) can be approximated to (adapted from previous work by Iver Brevik) $B_0 H = -\frac{AN}{2B_0} = -F$, then $H(R=1) \approx -\frac{F}{B_0}$. Then,

$$H(R) \approx -\frac{F}{B_0}\frac{K_0(\sqrt{B_0}R)}{K_0(R)} \tag{3.12}$$

for large values of R.

$$H(R) \sim \frac{K_0(\sqrt{B_0}R)}{K_0(R)} \tag{3.13}$$

The Basset function $K_0(x)$ can be written as [20]

$$K_0(x) = \frac{e^{-x}}{\sqrt{x}}\big(1.25331 - \frac{0.7862 \cdot 2}{x} + ...\big) \tag{3.14}$$

for $x \geq 2$. Inserting this into equation (3.13) (only including the first term) results in

$$H(R) \sim \frac{e^{-\sqrt{B_0}R}}{\sqrt{R}}. \tag{3.15}$$

In order to check whether the approximations made are acceptable, $H(R)$ from equation (3.15) is put back into the modified Bessel differential equation in (3.9).

$$H = \frac{e^{-\sqrt{B_0}R}}{\sqrt{R}}, \quad H_R = -\Big(\frac{1}{2R} + \sqrt{B_0}\Big)H, \quad H_{RR} = \left(\frac{1}{2R^2} + \Big(\frac{1}{2R} + \sqrt{B_0}\Big)^2\right)H \tag{3.16}$$

into equation (3.9):

$$B_0 H - \frac{1}{R}\Big(\frac{1}{2R} + \sqrt{B_0}\Big)H - \Big(\frac{1}{2R^2} + \frac{1}{4R^2} + \frac{\sqrt{B_0}}{R} + B_0\Big)H = -\frac{H}{4R^2}. \tag{3.17}$$

This is an acceptable approximation when $H \to 0$ and $R \to \infty$, as the term $-H/(4R^2)$ goes to zero. The approximative solution for $H(R)$ when R grows to infinity is then

$$H(R) = \frac{1}{\sqrt{R}} e^{-\sqrt{B_0}R}. \tag{3.18}$$

In order to rearrange this to a function $R(H)$, the Lambert function needs to be introduced [21], [22]. The Lambert W-function is defined as the inverse of

$$f(W) = We^W, \tag{3.19}$$

so that

$$R(H) = \frac{1}{2\sqrt{B_0}} W\Big(\frac{2\sqrt{B_0}}{H^2}\Big), \tag{3.20}$$

for $H \to 0$.

The boundary at $R \to 0$

The next boundary condition to be introduced is the case when $R \to 0$. As discussed earlier, the laser beam intensity has its maximum at this boundary. It is therefore reasonable to assume maximum deformation at this point. If H has its maximum (or most negative z-value at $R = 0$, then H_R must be equal to zero.

$$\lim_{R\to 0} H = H_{max}, \quad \lim_{R\to 0} H_R = 0 \tag{3.21}$$

The last term of equation (3.21) can, as before, be reformulated to

$$\lim_{R\to 0} \big(R_H^2\big)^2 = \lim_{R\to 0} \Big(\frac{1}{H_R}\Big)^2 = \infty. \tag{3.22}$$

The boundary conditions at both ends, $R \to \infty$ and $R \to 0$, are in good agreement with the experimental results of Casner and Delville.

Using the boundary conditions at the region of small R-values, an analytical approximation may be found. The $\exp(-2R^2)$ term on the right hand side of equation (3.6) has a limit value of

$$\lim_{R\to 0} e^{-2R^2} = 1. \tag{3.23}$$

The function $f'(a, B_0, R_H)$ becomes:

$$\lim_{R_H^2\to\infty} f'(a, B_0, R_H) = \frac{(1+a^2)R_H^2 \cdot B_0 R_H^4}{(1+a)^2 R_H^2 \cdot R_H^4} = \frac{(1+a^2)}{(1+a)^2} B_0^2. \tag{3.24}$$

The constant a is the relationship between the two refractive indices n_{out}/n_{in}. The difference in the two refractive indices Δn varies between $6 \cdot 10^{-3}$ and $2 \cdot 10^{-2}$ so that $0.989 < a$ 0.996 [16]. Therefore, a will be assumed to be unity.

$$\lim_{R_H^2\to\infty} f'(a, B_0, R_H) \approx \frac{1}{2} B_0^2 \tag{3.25}$$

Then the right hand side of equation (3.6) has the limiting value

$$-\frac{\Delta n P B_0}{\pi c \sigma l_c} \tag{3.26}$$

Here, also the term $N = \frac{(n_{in}-n_{out})}{(n_{in}+n_{out})} n_{out}$ has been simplified by assuming $a = 1$ and $n_{in} - n_{out} = \Delta n$. Also the left hand side of equation (3.6) can be simplified near the boundary of $R \to 0$.

$$\lim_{R\to 0}\left(B_0 H - \frac{1}{R\sqrt{R_H^2 + \frac{1}{B_0}}} - \frac{2R_{HH}}{\left(R_H^2 + \frac{1}{B_0}\right)^{\frac{3}{2}}}\right) = B_0 H - \frac{1}{R R_H}, \tag{3.27}$$

which then gives the following differential equation for $R \to 0$:

$$B_0 H - \frac{1}{R R_H} = -C, \tag{3.28}$$

where $C \equiv (\Delta n P B_0)/(\pi c \sigma l_c)$. This differential equation is separable and can be integrated directly:

$$\begin{aligned} B_0 H - \frac{1}{R R_H} &= -C \\ R dR &= \frac{dH}{B_0 H + C} \\ \frac{1}{2} R^2 &= \ln(B_0 H + C) + \ln(c_0) \end{aligned} \tag{3.29}$$

The constant c_0 can be determined by using the boundary condition $H(R=0) = H_{max}$. Then,

$$R = \sqrt{2 \ln \left(\frac{B_0 H + C}{B_0 H_{max} + C} \right)} \tag{3.30}$$

or written more conveniently:

$$R(H) = \sqrt{2 \left| \ln \left(\frac{B_0 H + C}{B_0 H_{max} + C} \right) \right|} \tag{3.31}$$

as H only has negative z-values. (This last step may be considered as somewhat strange, but keep in mind that the shape of this function indeed fit the experimental results of Casner and Delville [24].)

Now, the two boundaries at $R \to \infty$ and $R \to 0$ have been investigated. Putting the two approximate solutions for $R(H)$ together results in the deformation shown in figure 3.1, which at least qualitatively is in good agreement with the experimental results of Casner and Delville for linear cases [24].

However, these two solutions do not cover the middle region for the nonlinear cases, where an "shoulder" appears. Further investigations for this middle region is therefore needed.

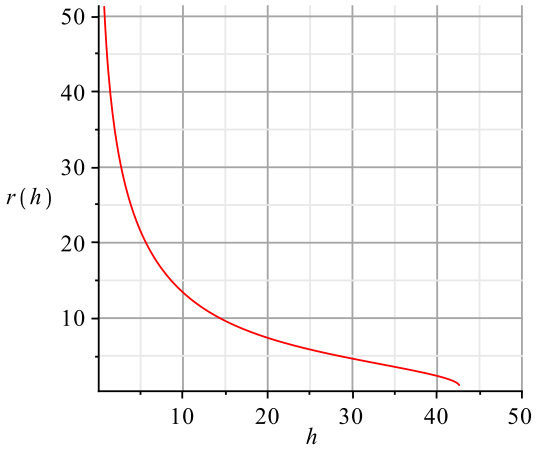

Figure 3.1: The approximative analytical functions for the two boundaries $H \to 0$ and $H \to H_{max}$ put together. The case of $P = 600$ mW, $\omega_0 = 4.8\,\mu$m and $T - T_c = 2.5$ K is used, and H_{max} is approximated to be 42.5 μm (Casner [24]). Note that these parameters correspond to a nonlinear deformation with a "shoulder", but the shape of the two functions put together does not include this complex middle region.

3.3 Discussions of the middle region for nonlinear cases

In the cases where the laser beam power P is relatively weak (typically below 300 mW), the deformation is so-called linear (see figure 1.1). Here, the surface tension and the buoyancy are always pointing inwards, from medium *out* to medium *in*. The radiation force is pointing outwards. But what happens when the laser beam power increases? Suddenly, the middle region changes its shape by the appearance of a "shoulder". The direction of the buoyancy and the radiation force is still the same, as these forces depend on the difference in mass density and the refractive indices, respectively. The surface tension, however, has direction depending on the shape of the surface (figure 2.11). This means that in the nonlinear cases, the surface tension is pointing outwards in the middle region.

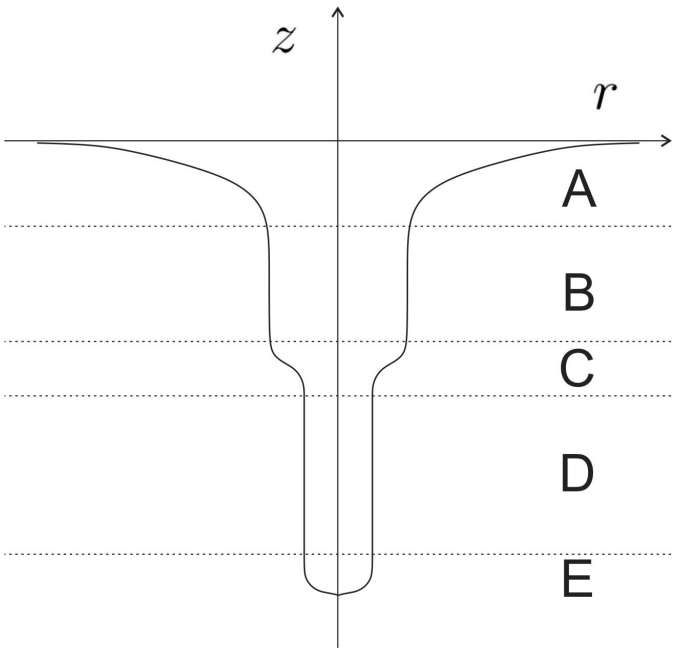

Figure 3.2: Figure showing the nonlinear liquid-liquid interface deformations with the shoulder-shaped divided into five sections.

What is causing this change in surface tension direction (and hence causing the shape to change so dramatically)? As discussed in section 2.4, the buoyancy increases linearly with the depth of the deformation, H. The laser beam intensity is assumed to have a Gaussian distribution depending only on the radius, R, and not the z-component (H). This means that in the regions B and D, as shown in figure 3.2, the force from the laser is almost constant (as R is the same for varying H), while the buoyancy is increasing along the deformation. The surface tension is also constant (and $\to 0$), due to the straight line (neither concave nor convex). It is therefore quite easy to imagine that at some

point, the buoyancy grows so large that the force form the laser beam is no longer able to pull the liquid-liquid interface downwards with the same width as the B-region has. Therefore, the shape changes to the form of region C, where the radiation force and the surface tension act outwards and the buoyancy inwards. Now, the radius R is decreasing, which means that the radiation force is increasing until it (again) is able to withstand the buoyancy without "help" from the surface tension. Note that this explanation is a qualitatively guess based on the experimental observations.

In the cases of small deformations (low power P), the height of the deformation is probably not large enough for the buoyancy to dominate and cause a change in the direction of the surface tension.

The challenge with the middle region (B, C and D), that is characteristic for the nonlinear deformations, is that there are no analytical approximations for this area. As will be seen later, in chapter 4, as well as in the results of Hallanger [16], there are some numerical solutions for the cases of high laser beam intensity (in the nonlinear region). But these solutions do not include the shoulder (although they satisfy the differential equation). One probably needs some more information concerning the middle region of nonlinear cases before being able to find the numerical solutions that match the experiments.

Comment: What if the laser beam impinges from above? As discussed earlier, the direction on the radiation force does not depend on the direction of the laser beam (if it is illuminating the surface from above or below), but on the refractive indices of the two liquids. This does not mean, however, that the shape of the deformation is the same for the two cases. In fact, if the laser beam is pointing downwards, from medium *in* to medium *out*, much larger deformations can be obtained (long liquid column that emits droplets or optical fiber-like deformations). The reason for this asymmetry may be total reflection of the laser beam. For further reading, see for instance [17], [12], [18], [7] or [23].

3.4 Estimating the value of h_{max} and discussion of the bottom radius

As found in section 3.2, the boundary condition for $r \to 0$ is $h \to h_{max}$ (or $H \to H_{max}$). Unfortunately, the maximum deformation h_{max} is an unknown parameter. It can be estimated by measuring the photographs taken during the experiments of Casner and Delville [24], but a theoretical model which gives h_{max} for a given laser power P and beam waist ω_0 is not available. The fact that one of the boundaries contains an unknown parameter complicates the process of finding a numerical solution of the differential equation (3.6).

To find some estimated values of h_{max}, the results from the doctoral thesis of Alex Casner

[24] can be consulted. The values in table 3.1 are measured from the pictures included in Casner's thesis, so an inaccuracy of at least a couple of micrometers should in principle be taken into account. These values are in other words (and as mentioned earlier) just estimates, and should be used qualitatively rather than quantitatively, e.g. to check whether numerical results are reasonable or not.

$T - T_c$ [K]	ω_0 [μm]	P [mW]	h_{max} [μm]	a_0 [μm]
2.5	6.3	1 200	70	3.2
2.5	6.3	600	40	3.8
2.5	4.8	1 200	72	2.5
2.5	4.8	600	42.5	2.6

Table 3.1: Measured values of the deformation h_{max} and half of the width a of the bottom part of the deformation at given beam waists, temperature and laser powers. The values are measured from the experiments from Casner's doctoral thesis [24] with an inaccuracy of a couple of micrometers. The deformation increases with larger laser power and narrower laser beam.

As can be seen from table 3.1, the deformation h_{max} increases with larger beam power P. In addition, it seems like a narrower beam (smaller beam waist) also results in a larger deformation.

Estimating the h_{max}– a_0 dependence.

The bottom part of the liquid-liquid interface deformation can be assumed to have the shape of a hemisphere. The radius of the hemisphere is a_0 (see table 3.1). Then, by considering this hemisphere under illumination by a laser beam and balancing with the surface tension and buoyancy, an expression containing the two parameters h_{max} and a_0 can be found. The difference between what is already done previously when searching for the differential equation of this system and this case is that the shape of the deformation is now known. By considering general expressions of the incoming and transmitted electric an magnetic field components of plane waves, an expression for the laser force on the hemisphere can be derived. Appendix B includes the work of Iver Brevik (Spring 2011) on this particular case. It has not yet been published as an article, and is therefore included as a whole (copied and translated from working notes). The model is based on previous theoretical work by Brevik et al. on forces on a sphere from an electromagnetic field (see, for instance [13] or [26]).

In this section, the results from appendix B will be investigated in order to estimate the value of the maximum deformation h_{max} for a given bottom radius a_0 (and given laser power, beam waist and temperature) and vice versa. The results can be compared to the measured values from table 3.1. If the results are reasonable, it means that the maximum

deformation h_{max} can be predicted from theory, not only taken from experimental results.

The force balance for a hemisphere under illumination is (appendix B, equation (B.8)):

$$(\rho_{out} - \rho_{in})g\pi a_0^2 h + (\rho_{out} - \rho_{in})\frac{2}{3}g\pi a_0^3 + 2\pi\sigma a_0 = |F_{RAD}|, \tag{3.32}$$

where ρ_{out} and ρ_{in} are the mass densities of medium *out* and medium *in*, respectively, a_0 is the radius of the hemisphere and h is the depth of the deformation (see figure B.1). The right hand side of equation (3.32) is the absolute value of the radiation force from the laser. This can be expressed as (before equation (B.95)):

$$F_{RAD} = Q\epsilon_0 E_0^2 a_0^2 \tag{3.33}$$

The electric field amplitude E_0 can be written as a function of the laser intensity, as done previously. The factor Q is in fact a quite complicated sum deduced from the expressions for the electric field components. From Brevik (equation (B.96)):

$$Q = -\frac{1}{8}(n_{12}^2 - 1)\sum_{l=1}^{\infty}\frac{2l+1}{l(l+1)}\Big\{n_1^2|c_{l1}|^2[\alpha^2(\psi_l(n_{12}\alpha)')^2 I_t + \big(l(l+1)\big)^2(\psi_l(n_{12}\alpha))^2 I_r] + \\ + \alpha^2|d_{l1}|^2(\psi_l(n_{12}\alpha)^2 I_t\Big\} \tag{3.34}$$

An explanation of all the parameters and variables included in the expression for Q is given in table 3.2. The expression for Q can be evaluated numerically, by calculating the series with the help of a computer (using software like Maple or similar). But first, the case of $l = 1$ will be investigated analytically in order to get an idea of the size of each term in Q.

Special case, $l = 1$.

The associated Legendre function for $l = 1$ can be written as $P_1^1(x) = -\sqrt{1 - x^2}$. Then, the integrals I_t and I_r become

$$I_t = \int_0^1 (x^2 + 1)x\,\mathrm{d}x = \Big[\frac{1}{4}x^4 + \frac{1}{2}x^2\Big]_0^1 = \frac{3}{4}, \tag{3.35}$$

and

$$I_r = \int_0^1 (1 - x^2)x\,\mathrm{d}x = \Big[\frac{1}{2}x^2 - \frac{1}{4}x^4\Big]_0^1 = \frac{1}{4}. \tag{3.36}$$

The Riccati-Bessel functions of $l = 1$ are (from Appendix B) read:

$$\psi_1(x) = xj_1(x) = \frac{\sin x}{x} - \cos x, \tag{3.37}$$

and

$$\xi_1^{(1)}(x) = xh_1(x) = -\Big(1 + \frac{i}{x}\Big)e^{ix}. \tag{3.38}$$

Symbol	Expression	About	Equation.
n_1	n_{in}	Refractive index of medium *in*.	fig. B.1
n_{12}	$\frac{n_{in}}{n_{out}}$	Ratio of refractive indices.	(B.17)
c_{l1}	$\frac{i \cdot A_{l1}}{n_{12}^2 \psi(n_{12}\alpha)\xi_l^{(1)'}(\alpha) - n_{12}\psi_l'(n_{12}\alpha)\xi_l^{(1)}(\alpha)}$	Coefficient in the expression for the electromagnetic field. Determined by the boundary conditions of the system.	(B.71)
A_{l1}	$\frac{i^{l+1}}{\alpha^2}\sqrt{\frac{4\pi(2l+1)}{l(l+1)}}$	Coefficient from the incoming electromagnetic field.	(B.71)
α	$n_{out}\frac{\omega a_0}{c} = \frac{2\pi a}{\lambda_{out}}$	λ_{out} is the wavelength of the electromagnetic wave in medium *out*.	bef. (B.17)
ψ_l	$x \cdot j_l(x)$	Riccati-Bessel function.	(B.21)
ψ_l'	$\frac{\mathrm{d}}{\mathrm{dx}}(x \cdot j_l(x))$	Derivative of ψ_l.	
$\xi_l^{(1)}(x)$	$x \cdot h_l^{(1)}(x)$	Riccati-Bessel function.	(B.21)
$\xi_l^{(1)'}(x)$	$\frac{\mathrm{d}}{\mathrm{dx}}(x \cdot h_l^{(1)}(x))$	Derivative of $\xi_l^{(1)}$	
I_t	$\int_0^1 \left[(1-x^2)\left(\frac{\mathrm{d}P_l^1}{\mathrm{dx}}\right)^2 + \frac{(P_l^1)^2}{1-x^2}\right] x \,\mathrm{d}x$	Integral containing the associated Legendre function P_l^1.	(B.93)
I_r	$\int_0^1 (P_l^1)^2 x \,\mathrm{d}x$		(B.93)
d_{l1}	$\frac{i \cdot B_{l1}}{\psi(n_{12}\alpha)\xi_l^{(1)'}(\alpha) - n_{12}\psi_l'(n_{12}\alpha)\xi_l^{(1)}(\alpha)}$	Coefficient in the expression for the electromagnetic field. Determined by the boundary conditions of the system.	(B.73)
B_{l1}	$\frac{i^l}{\alpha^2}\sqrt{\frac{4\pi(2l+1)}{l(l+1)}}$	Coefficient from the incoming electromagnetic field.	(B.73)

Table 3.2: Table contaning the elements of equation (3.34).

The derivatives of the Riccati-Bessel functions then become

$$\psi_1'(x) = \left(1 - \frac{1}{x^2}\right)\sin x + \frac{\cos x}{x}, \tag{3.39}$$

and

$$\xi_1^{(1)'} = -\left(i - \frac{1}{x} - \frac{i}{x^2}\right)e^{ix} = \left(\frac{1}{x} + i\left(\frac{1}{x^2} - 1\right)\right)e^{ix}. \tag{3.40}$$

The coefficients A_{11} and B_{11} are (inserting $l = 1$)

$$A_{11} = -\frac{1}{\alpha^2}\sqrt{6\pi}, \quad B_{11} = \frac{i}{\alpha^2}\sqrt{6\pi}. \tag{3.41}$$

With all these expressions, the coefficients c_{11} and d_{11} can be found. Later, when inserting them into the expression for Q, only the absolute value of c_{11} and d_{11} will be used, so there are no problems with them being complex coefficients. In order to keep a sense of

tidiness, the products of the Riccati-Bessel functions will first be investigated.

$$\begin{aligned}\psi_l(n_{12}\alpha)\xi_1^{(1)'}(\alpha) &= \Big(\frac{\sin(n_{12}\alpha)}{n_{12}\alpha} - \cos(n_{12}\alpha)\Big)\Big(\frac{1}{\alpha} + i\big(\frac{1}{\alpha^2} - 1\big)\Big)e^{i\alpha} \\ &= \left\{\Big[\frac{\sin(n_{12}\alpha)}{n_{12}\alpha^2} - \frac{\cos(n_{12}\alpha)}{\alpha}\Big] + i\Big[\frac{\sin(n_{12}\alpha)}{n_{12}\alpha} - \cos(n_{12}\alpha)\Big]\Big(\frac{1}{\alpha^2} - 1\Big)\right\}e^{i\alpha}, \end{aligned} \tag{3.42}$$

$$\begin{aligned}\psi_l'(n_{12}\alpha)\xi_1^{(1)}(\alpha) &= -\left(\Big(1 - \frac{1}{(n_{12}\alpha)^2}\Big)\sin(n_{12}\alpha) + \frac{\cos(n_{12}\alpha)}{n_{12}\alpha}\right)\Big(1 - \frac{i}{\alpha}\Big)e^{i\alpha} \\ &= -\left\{\left[\Big(1 - \frac{1}{(n_{12}\alpha)^2}\Big)\sin(n_{12}\alpha) + \frac{\cos(n_{12}\alpha)}{n_{12}\alpha}\right] - \right. \\ &\quad \left. - i\left[\Big(1 - \frac{1}{(n_{12}\alpha)^2}\Big)\frac{\sin(n_{12}\alpha)}{\alpha} + \frac{\cos(n_{12}\alpha)}{n_{12}\alpha^2}\right]\right\}e^{i\alpha}. \end{aligned} \tag{3.43}$$

Then, the coefficient c_{11} can be written as

$$\begin{aligned}c_{11} &= -\frac{i\sqrt{6\pi}}{\alpha^2 n_{12}}\Big(n_{12}\psi_1(n_{12}\alpha)\xi_1^{(1)'}(\alpha) - \psi_1'(n_{12}\alpha)\xi_1^{(1)}(\alpha)\Big)^{-1} \\ &= \frac{\sqrt{6\pi}}{\alpha^2 n_{12}e^{i\alpha}}\left\{\left[\Big(\frac{1}{\alpha^4} + \frac{1}{n_{12}^2\alpha^3} - \frac{1}{\alpha^2} - \frac{1}{\alpha}\Big)\sin(n_{12}\alpha) + \Big(n_{12} - \frac{1}{n_{12}\alpha^2} - \frac{n_{12}}{\alpha^2}\Big)\cos(n_{12}\alpha)\right] + \right. \\ &\quad \left. + i\left[\Big(1 + \frac{1}{\alpha^2} - \frac{1}{(n_{12}\alpha)^2}\Big)\sin(n_{12}\alpha) + \Big(\frac{1}{n_{12}\alpha} - \frac{n_{12}}{\alpha}\Big)\cos(n_{12}\alpha)\right]\right\}^{-1}, \end{aligned} \tag{3.44}$$

so that the absolute value squared becomes

$$\begin{aligned}|c_{11}|^2 = \frac{6\pi}{\alpha^4 n_{12}^2}\left\{\left[\Big(\frac{1}{\alpha^4} + \frac{1}{n_{12}^2\alpha^3} - \frac{1}{\alpha^2} - \frac{1}{\alpha}\Big)\sin(n_{12}\alpha) + \Big(n_{12} - \frac{1}{n_{12}\alpha^2} - \frac{n_{12}}{\alpha^2}\Big)\cos(n_{12}\alpha)\right]^2 + \right. \\ \left. + \left[\Big(1 + \frac{1}{\alpha^2} - \frac{1}{(n_{12}\alpha)^2}\Big)\sin(n_{12}\alpha) + \Big(\frac{1}{n_{12}\alpha} - \frac{n_{12}}{\alpha}\Big)\cos(n_{12}\alpha)\right]^2\right\}^{-1}. \end{aligned} \tag{3.45}$$

Next, the coefficient d_{11} reads:

$$\begin{aligned}d_{11} = -\frac{\sqrt{6\pi}}{\alpha^2 e^{i\alpha}}\left\{\left[\Big(\frac{1}{n_{12}\alpha^2} + n_{12} - \frac{1}{n_{12}\alpha^2}\Big)\sin(n_{12}\alpha) + \Big(\frac{1}{\alpha^2} - \frac{1}{\alpha}\Big)\cos(n_{12}\alpha)\right] + \right. \\ \left. + i\left[\Big(\frac{2}{n_{12}\alpha^3} - \frac{1}{n_{12}\alpha} - \frac{n_{12}}{\alpha}\Big)\sin(n_{12}\alpha) + \Big(1 - \frac{2}{\alpha^2}\Big)\cos(n_{12}\alpha)\right]\right\}^{-1} \end{aligned} \tag{3.46}$$

Taking the absolute value gives:

$$|d_{11}|^2 = \frac{6\pi}{\alpha^4}\Bigg\{\Bigg[\Big(\frac{1}{n_{12}\alpha^2}+n_{12}-\frac{1}{n_{12}\alpha^2}\Big)\sin(n_{12}\alpha)+\Big(\frac{1}{\alpha^2}-\frac{1}{\alpha}\Big)\cos(n_{12}\alpha)\Bigg]^2+$$
$$+\Bigg[\Big(\frac{2}{n_{12}\alpha^3}-\frac{1}{n_{12}\alpha}-\frac{n_{12}}{\alpha}\Big)\sin(n_{12}\alpha)+\Big(1-\frac{2}{\alpha^2}\Big)\cos(n_{12}\alpha)\Bigg]^2\Bigg\}^{-1}. \tag{3.47}$$

If the first term in Q (the case of $l=1$) is called Q_1, then one has

$$Q_1 = -\frac{3}{64}(n_{12}-1)\Bigg\{n_{in}|c_{11}|^2\Big[3\alpha^2\Big(\psi_1'(n_{12}\alpha)\Big)^2+4\Big(\psi_1(n_{12}\alpha)\Big)^2\Big]+3\alpha^2|d_{11}|^2\Big(\psi_1(n_{12}\alpha)\Big)^2\Bigg\}. \tag{3.48}$$

Now, the parameters n_{12}, α and n_{in} need to be determined in order to find a numerical solution of the first term Q_1 (as well as the terms of higher degree l). In the experiments of Casner and Delville, an argon (Ar^+) laser was used. The wavelength of this laser is $\lambda_0 = 5\,145$ Å[24]. In addition, the refractive index n_{in} is assumed to be quite close to n_{out}, such that

$$n_{out} \approx n_{in} \approx n = 1.464 \tag{3.49}$$

The value of n_{12} is then slightly above one, as $\Delta n/\Delta\rho = -1.22\cdot10^{-4}$ [16]. For $T-T_c =$ 2K, the difference in mass density $\Delta\rho = 55.4\frac{\text{kg}}{\text{m}^3}$ [24], which gives a value Δn = -0.00676. Note that a temperature of $T-T_c = 2.5$ K is used in the experiments of Casner and Delville, but the table in [24] does not contain this value. Then, n_{12} can be found:

$$\frac{n_{out}-n_{in}}{n_{out}} = 1-n_{12} \qquad \Longrightarrow\ n_{12} \approx 1-\frac{\Delta n}{n} \approx 1.0046. \tag{3.50}$$

The values used above lead to a value α of $\alpha \approx a_0\cdot 2.44\cdot10^7$. The radius a_0 is not known, as discussed earlier, so it has to be estimated from the experimental results of Casner and Delville in order to find the maximum deformation h_{max}. Using a beam waist of $4.8\,\mu$m and $T-T_c = 2.5$ K, the radius will be estimated to 2.5 μm (see table 3.1). Then, $\alpha \approx 44.70$ and the first term in Q has a numerical value of

$$Q_1 = -2.921317760\cdot10^{-5} \tag{3.51}$$

In the expression for F_{RAD} (equation (3.33)), the electric field amplitude E_0 can be replaced by

$$E_0^2 = \frac{I}{\epsilon_0 n_{out} c} = \frac{2P}{\pi\omega_0^2\epsilon_0 n_{out} c}, \tag{3.52}$$

so that

$$F_{RAD} = \frac{2Pa_0^2Q}{\pi\omega_0^2 n_{out} c}. \tag{3.53}$$

Using the case of $T-T_c = 2.5$ K, $\omega_0 = 4.8\mu$m and $P = 1200$ mW (again, see table 3.1), the contribution from Q_1 to the radiation force is

$$F_{RAD1} = \frac{2Pa_0^2Q_1}{\pi\omega_0^2 n_{out} c} = -0.0138\,\text{pN} \tag{3.54}$$

In order to compare the size of this force relative to the whole force balance of this system, the left hand sider of equation (3.33) can also be estimated numerically. Inserting 72 μm for h_{max} (table 3.1) and $\sigma = 1.8 \cdot 10^{-7} \frac{\mathrm{N}}{\mathrm{m}}$ (Casner, page 85 [24]):

$$\begin{aligned} LHS &= \Delta\rho g \pi a_0^2 h_{max} + \Delta\rho g \frac{2}{3}\pi a_0^3 + 2\pi a_0 \sigma \\ &= 0.768\,\mathrm{pN} + 0.0178\,\mathrm{pN} + 2.827\,\mathrm{pN} \\ &= 3.613\,\mathrm{pN} \end{aligned} \tag{3.55}$$

This means that the first term in Q represents about 0.4 % of the total radiation force if this model is representative for the liquid-liquid system. To answer this question, more terms in Q must be included.

Finding Q and F_{RAD}, $l > 1$

The first term in Q has been calculated analytically and estimated numerically. Now, the rest of the terms will be obtained numerically for in order to investigate whether the model is describing the bottom part of the liquid-liquid deformation. Due to the complexity of each term, this will be done numerically (using the software Maple 15). The input parameters that can be adjusted to give different values of Q are α, n_{12} and n. In order to find the corresponding radiation force, F_{RAD}, the radius a_0, the beam waist ω_0 and the laser power P must also be given. Since the model has to be checked against the experimental values of a_0 and h_{max} before it can be used to predict these values for arbitrary inputs and parameters, the left hand side of equation (3.33) will first be compared to the right hand side for the cases given in table 3.1. The stability of Q with respect to the input parameters will also be investigated.

It seems reasonable to start where the last subsection ended, using the same parameters as for the term Q_1. Summing up all the terms up to $l = 100$ gives a numerical value of

$$Q(\alpha = 44.7, n_{12} = 1.0046, n = 1.464) = \sum_{l=1}^{100} Q_l = -0.8080427735. \tag{3.56}$$

Summing l up to 200 also gives $Q = -0.8080427735$, so the first 100 terms is assumed to be sufficient. This corresponds to a radiation force of

$$F_{RAD}(\alpha = 44.7, n_{12} = 1.0046, n = 1.464) = 381.3\,\mathrm{pN}, \tag{3.57}$$

which in fact is more than 100 times the estimated value of the forces on the left hand side (as above, $P = 1.2$ W, $a_0 = 2.5\,\mu$m and $\omega_0 = 4.8\,\mu$m). Some of this deviation may be explained by the uncertainties in the measurements of the experimental results, but most likely there are some problems with the model itself. All the terms in the sum are plotted in figure 3.3. As can be seen, the terms from $l = 10$ to $l = 50$ are dominating, with term values up to 0.095 ($l \approx 40$). This term alone represents a 10 times larger force than the whole left hand side of equation (3.33). The terms from $l \approx 60$ and above are

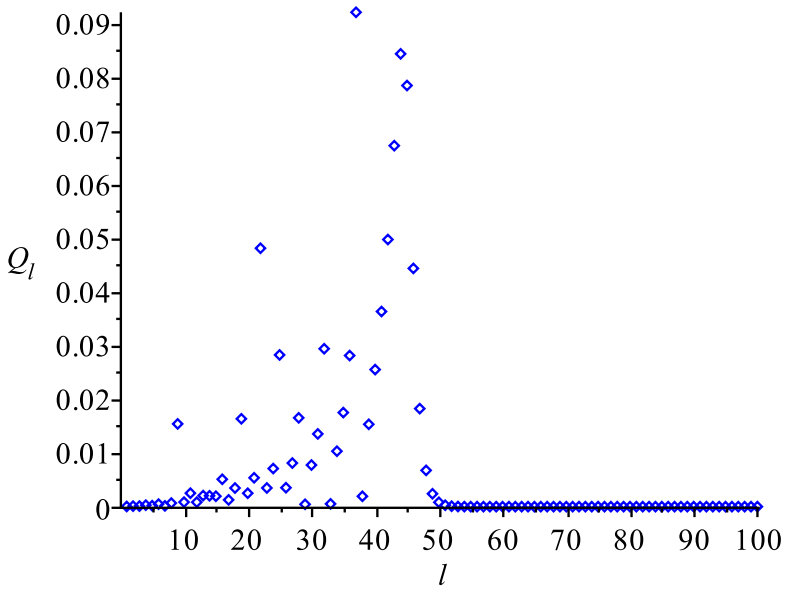

Figure 3.3: Figure showing the absolute value of the terms Q_l for l from 0 to 100 with parameters $\alpha = 44.7$, $n_{12}\alpha = 44.9$ and $n = 1.464$. The total sum Q of the terms Q_l is -0.8080427735 and corresponds to a total radiation force of $|F_{RAD}| = 381.3\,\text{pN}$.

close to zero, which is also confirmed by comparing the sum of $\sum_{l=1}^{100} Q_l$ and $\sum_{l=1}^{200} Q_l$. Before concluding and dismissing the model, also the other some other parameter sets will be checked. The parameter values are taken from Casner's doctoral thesis (table 3.1), and the numerically estimated values for F_{RAD} and the corresponding left hand side of equation (3.33) can be found in table 3.3. The imbalance of the left hand side

ω_0 [μm]	P [mW]	h_{max} [μm]	a_0 [μm]	α	$\lvert Q\rvert$	$\lvert F_{RAD}\rvert$ [pN]	LHS [pN]
6.3	1 200	70	3.2	57.2	1.72061611	772.2	4.880
6.3	600	40	3.8	67.9	3.48691702	1103.3	5.345
4.8	1 200	72	2.5	44.7	0.808042774	381.3	3.613
4.8	600	42.5	2.6	46.5	1.10666415	887.2	3.452

Table 3.3: Table showing the numerically estimated values for $|F_{RAD}|$ and the left hand side of equation (3.33) based on the four measured cases from Casner and Delville [24]. Here, $T - T_c = 2.5$ K, $\Delta\rho = 55.4\,\frac{\text{kg}}{\text{m}^3}$, $n = 1.464$, $\lambda_0 = 5\ 145$ Å, $n_{12} = 1.0046$ and $\sigma = 1.8 \cdot 10^{-7}\,\frac{\text{N}}{\text{m}}$. As can be seen in all cases, the left hand side and the radiation force are not in balance. The size of each term in the four cases are given in figure 3.4.

and the radiation force is too large to accept the model for this system. But what are

the reasons for this model failing? In order to find a model that fits the system better, this question should be tried answered.

How Q depends on n_{12}, α and n.

As mentioned previously, Q is a function of the parameters α, n and n_{12}. In the last subsection, the only parameter that changed was α. This dimensionless parameter is a wave number $\alpha = (2\pi a_0 n)/\lambda_0$ [27]. It contains the relation between the radius a_0 of the hemisphere and the wavelength λ_0 of the laser beam. The case of $\alpha > 100$ is referred to as the region of geometrical optics (λ_0 much smaller than a_0), whereas $\alpha < 10$ is the region of wave optics (λ_0 about the same order as a_0) [27]. The Rayleigh-region occurs when $\alpha < 1$. Here, only low degrees l will contribute to the sum, whereas higher degree terms must be included for geometrical optics (see the article of Brevik and Almaas on radiation force on a sphere [27]). This description fits the present model, as higher degree terms seem to be more important for α around 60–70 (figure 3.4a and 3.4b) than for $\alpha \approx 45$ (figure 3.4c and 3.4d). Note that the last term in Q that contributes to the sum, $Q_{l_{max}}$, (not equal to zero) is related to α. Judging by figure 3.4, it seems like $l_{max} \approx \alpha$. Also, the sum Q itself seem somewhat larger for high values of α than lower. This may be explained by the value of the radius a_0, as lower laser powers (and larger beam waists, ω_0) seem to result in a wider bottom part of the liquid-liquid interface deformation, hence a larger value of a_0. It is reasonable to assume that the total force of a big hemisphere is larger than the total force on a smaller hemisphere.

Now, what happens if the value of n_{12} changes? Going back to the case first investigated, with a power $P = 1\,200\,\mathrm{mW}$ and beam waist $\omega_0 = 4.8\,\mu\mathrm{m}$, what is Q with a slightly larger n_{12}? Remembering that $\Delta n = -1.22 \cdot 10^{-4}\,\frac{\mathrm{m}^3}{\mathrm{kg}} \cdot \Delta\rho(T - T_c)$, a change in temperature and hence mass density $\Delta\rho$ will lead to a change in n_{12}. For instance, two examples from Casner can be used [24]:

$$\Delta\rho(T - T_c = 3\,\mathrm{K}) = 63.3\,\frac{\mathrm{kg}}{\mathrm{m}^3} \quad \Longrightarrow\ n_{12} = 1 - \frac{\Delta n}{n} = 1.0053 \tag{3.58}$$

and

$$\Delta\rho(T - T_c = 10\,\mathrm{K}) = 93.5\,\frac{\mathrm{kg}}{\mathrm{m}^3} \quad \Longrightarrow\ n_{12} = 1 - \frac{\Delta n}{n} = 1.0078. \tag{3.59}$$

These changes in n_{12} (but keeping $\alpha = 44.7$ and $n = 1.464$) will lead to new values of Q:

$$Q(\alpha = 44.7, n_{12} = 1.0053, n = 1.464) = -0.9425797598 \tag{3.60}$$

$$Q(\alpha = 44.7, n_{12} = 1.0078, n = 1.464) = -2.255140355 \tag{3.61}$$

The corresponding terms can be seen in figure 3.5. As both the plots and sums imply (recall figure 3.3), a larger value of n_{12} leads to a higher radiation force. Remembering the expression for the radiation force per volume from chapter 2, equation (2.10), it depends on the change in the permittivity ϵ. In other words, the bigger difference between the

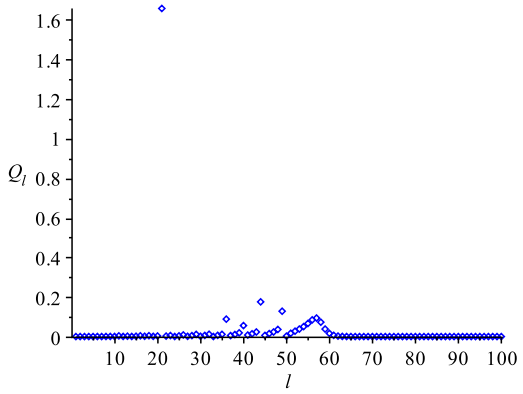

(a) Figure showing the terms Q_l for l from 0 to 100 with parameters $\alpha = 57.2$, $n_{12}\alpha = 57.5$ and $n = 1.464$. The total sum Q of the terms Q_l is -1.720616108.

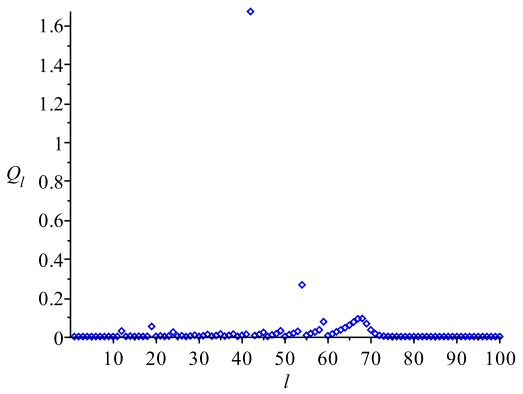

(b) Figure showing the terms Q_l for l from 0 to 100 with parameters $\alpha = 67.9$, $n_{12}\alpha = 68.2$ and $n = 1.464$. The total sum Q of the terms Q_l is -3.486917023.

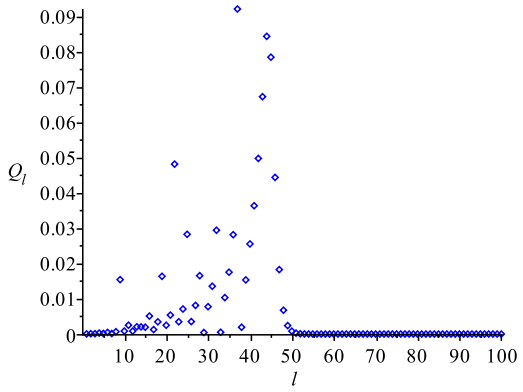

(c) Figure showing the terms Q_l for l from 0 to 100 with parameters $\alpha = 44.7$, $n_{12}\alpha = 44.9$ and $n = 1.464$. The total sum Q of the terms Q_l is -0.8080427735.

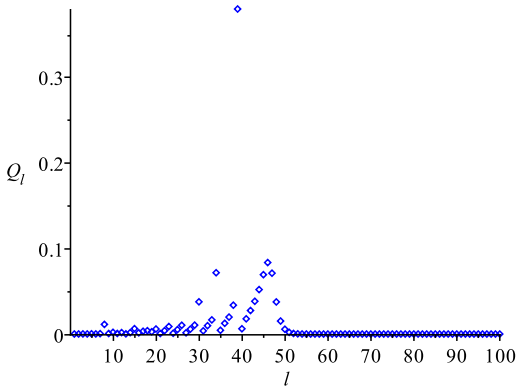

(d) Figure showing the terms Q_l for l from 0 to 100 with parameters $\alpha = 46.5$, $n_{12}\alpha = 46.7$ and $n = 1.464$. The total sum Q of the terms Q_l is -1.106664151.

Figure 3.4: Plots of the terms in Q (y-axis) as a function of the degree l (x-axis). The input parameters are given below each plot and the total sum and corresponding radiation force are given in table 3.3.

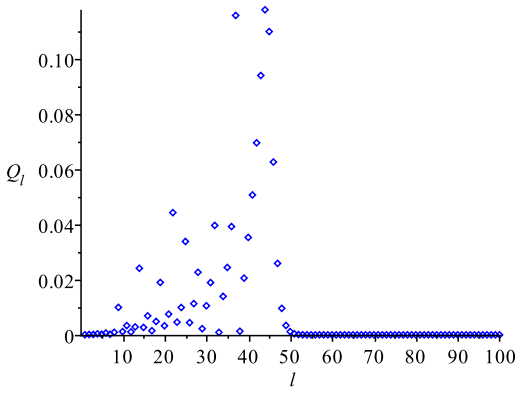

(a) Figure showing the terms Q_l for l from 0 to 100 with parameters $\alpha = 44.7$, $n_{12} = 1.0053$ and $n = 1.464$. The total sum Q of the terms Q_l is -0.9425797598.

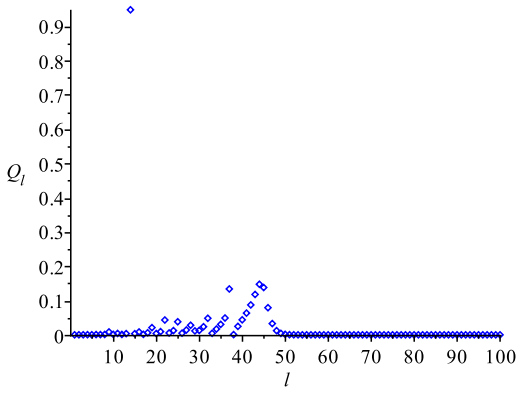

(b) Figure showing the terms Q_l for l from 0 to 100 with parameters $\alpha = 44.7$, $n_{12} = 1.0078$ and $n = 1.464$. The total sum Q of the terms Q_l is -2.255140355.

Figure 3.5: Plots of the terms in Q (y-axis) as a function of the degree l (x-axis). The input parameter n_{12} in figure 3.5b is slightly larger than the value of n_{12} in figure 3.5a, resulting in higher values for the terms Q_l.

refractive indices of medium *in* and medium *out*, the larger the radiation force becomes. The n_{12}-dependence can also be investigated directly by studying the expression for Q (equation (3.34)). If $n_{12} = 1$, Q will go to zero as it contains the factor $(n_{12}^2 - 1)$. The larger n_{12} is, the larger this factor will be, and it is reasonable to expect a larger value of Q.

Lastly, the parameter n will be discussed. This parameter is not a function of the temperature, but is set by the liquids used in the experiment. A change in n will affect both the wave number α and the factor n_{12}. As this parameter is not likely to change during the experiments, and since it changes both the parameters α and n_{12}, it will not be investigated further.

Conclusions on the model for the bottom part of the deformation.

By assuming that the bottom part of the liquid-liquid interface deformation has the shape of a hemisphere, the force balance for the buoyancy, surface tension and radiation force can be found as function of the bottom radius a_0 and the maximum deformation height h_{max}. By estimating one of them, the other can be predicted from theory without needing experimental measurements. It seems, however, that the model used above is not describing the liquid-liquid interface deformation satisfactorily, as the radiation force turns out to be at least 100 times larger than the counterforces (buoyancy and surface tension), indicating that the deformations should be much larger than what is observed in the experiments of Casner and Delville.

By investigating the factor Q in the expression of the radiation force factor Q, it seems like the terms behave like expected for the laser radiation force as the input parameters α and n_{12} change. The absolute value of the terms, however, are too large compared to the expected values of the surface tension and the buoyancy.

The reason, or reasons, to why this model does not fit this system is not known. But some explanations could be:

– The assumption of a hemisphered shape for the bottom part of the deformation is not valid, it may be too simple (remember that the boundary conditions at $r \to 0$ lead to an analytical approximation for this region that is different to a circle (see equation (3.31))).

– The theory leading to the expression Q does not fit the case of a hemisphere (it should be correct in the case of a full sphere, see article by Brevik and Almaas [27]). For instance, the assumption that only the case of $l = l'$ contributes to the sum may be correct for a sphere, but not for the hemisphere.

– Calculation errors can have occured, either in this section or in the derivation of equation (3.33).

These possible explanations should be investigated further in order to find a new model, or make changes to this model. The consequence of finding the relation between the bottom width of the deformation and the maximum depth h_{max} from theory would be that this relation could be predicted, and not only found after performing experiments.

3.5 First order differential equation

The last section of this chapter contains the final preparations before the numerical solving. Because a computer will be used to solve the differential equation, the differential equation describing the liquid-liquid interface deformation has to be fitted to a standard form and converted into first order. Because the differential equation is of second order, it has to be converted to a set of first order equations. Then, a new variable can be introduced:

$$G(H) = R_H(H), \tag{3.62}$$

so that

$$G_H(H) = R_{HH}(H). \tag{3.63}$$

Inserting this into the differential equation (3.6) results in:

$$B_0H - \frac{1}{R\sqrt{R_H^2 + \frac{1}{B_0}}} - \frac{2R_{HH}}{\left(R_H^2 + \frac{1}{B_0}\right)^{\frac{3}{2}}} = -\frac{AN}{B_0}e^{-2R^2}f(a, B_0, R_H)$$
$$B_0H - \frac{1}{R\sqrt{G^2 + \frac{1}{B_0}}} - \frac{2G_H}{\left(G^2 + \frac{1}{B_0}\right)^{\frac{3}{2}}} = -\frac{AN}{B_0}e^{-2R^2}f'(a, B_0, G), \tag{3.64}$$

where

$$f'(a, B_0, G) = \frac{(1+a^2)G^4\left[B_0^2G^4 + (2-a^2)B_0G^2 - aB_0G\sqrt{\left(G^2 + \frac{(1-a^2)}{B_0}\right)} + 1\right]}{\left(aG^2 - G\sqrt{\left(G^2 + \frac{(1-a^2)}{B_0}\right)}\right)^2\left(\frac{a}{B_0} - G\sqrt{\left(G^2 + \frac{(1-a^2)}{B_0}\right)}\right)^2}. \tag{3.65}$$

Equation (3.64) can then be solved for G_H:

$$G_H = \frac{1}{2}\left(B_0H + \frac{AN}{B_0}e^{-2R^2}f'(a, B_0, G)\right)\left(G^2 + \frac{1}{B_0}\right)^{\frac{3}{2}} - \frac{G^2}{2R} - \frac{1}{2B_0R}. \tag{3.66}$$

Then, the set of differential equations to be solved are

$$\begin{cases} R_H = G \\ G_H = \frac{1}{2}\left(B_0H + \frac{AN}{B_0}e^{-2R^2}f'(a, B_0, G)\right)\left(G^2 + \frac{1}{B_0}\right)^{\frac{3}{2}} - \frac{G^2}{2R} - \frac{1}{2B_0R} \end{cases}, \tag{3.67}$$

with $f'(a, B_0, G)$ given in equation (3.65). The boundary conditions are:

$$\begin{cases} R(0) = \infty \\ G(0) = -\infty \\ R(H_{max}) = 0 \end{cases} \tag{3.68}$$

Now, as the differential equation (or set of differential equations) is dimensionless, of first order and the boundary conditions are set, it is time to try solving it numerically.

Chapter 4

Numerical solution

In this chapter, the differential equation will be solved numerically in order to search for the shoulder-shaped nonlinear solution that has been observed during the experiments of the Bordeaux group. The numerical solutions depend on the given boundary conditions in addition to the differential equation itself. Not least, whether or not a solution is found at all depends on the method used for solving and the initial parameters and trial functions that are fed into the computer. Both the inputs and the corresponding outputs will be discussed in this chapter.

4.1 Solving method

The software that will be used to solve the differential equation is MATLAB® (7.6.0.324, R2008a). This is the same software that was used by Hallanger in his M.Sc. thesis in 2003 [16]. There will be, however, some differences in the approach of finding the solution, as Hallanger searched for the solution $H(R)$, whereas here, the differential equation will be solved for $R(H)$. In addition, as will be investigated later, the trial solution function will be different. Different inputs may lead to finding other solutions to the differential equation (if there are any), even though the boundary conditions of the systems are the same.

bvp4c

An built-in solver called bvp4c for boundary value problems will be used (again, the same as used by Hallanger in 2003). Here follows a short description of the solver, but a full description can be found in [25].

The bvp4c solver is a finite difference method solver. In order to solve a boundary value problem in MATLAB (bvp4c), the differential equation has to be of first order. If the differential equation is of second or higher order, the differential equation can be rearranged to a set of first order differential equations. In addition to the differential equation itself, two other types of inputs must be given before the solving can begin.

The first are the boundary conditions. The boundary conditions should be arranged to the form $b.c.(a) = 0$, meaning that a function describing the boundary condition at the limit a is zero. The last input is a trial function, an initial guess. Due to the complexity and high nonlinearity of the differential equation that is to be solved, whether or not the solution to the differential equation is found using the bvp4c method depends on how good this initial guess is. This trial function will be derived in the next section.

4.2 Trial function

As mentioned above, the trial function used here will be slightly different than the one Hallanger used in order to obtain his numerical results (see [16]). Hallanger used the analytical approximative solution for large R-values, the same as derived in subsection 3.2. At $R \to 0$, a simple function was derived to fit the boundary conditions. First, the differential equation was solved for low laser powers P. Then, the solutions for low laser powers was used as the trial solution for a slightly larger laser power. This iterative process was then repeated up to $P = 1\ 200$ mW. This may be one of the reasons why Hallanger did not find the shoulder-shaped nonlinear solution to the differential equation, as his trial function did not include this shape. If there are more than one solution to the differential equation with the given boundary conditions, it seems reasonable that the initial guess should be as close to the wanted solution as possible. Therefore, a more complex trial function will be searched for in order to investigate the possibility of finding the shoulder-shaped nonlinear solution.

The analytical approximations for the two boundaries from chapter 3 will be used. Then, the boundary conditions of the system are satisfied. But as mentioned before, the two approximative functions put together do not contain the special middle region shape of the nonlinear cases. Therefore, an extra function must be introduced.

Hyperbolic tangent

The hyperbolic tangent function is qualitatively similar to the middle region of the nonlinear deformations; keeping a constant value until a critical point, where the function suddenly changes to another value. Therefore, this function will be introduced in order to make a trial function that qualitatively (if not quantitatively) is similar to the observed liquid-liquid interface deformations for larger laser powers. In contrast to the two analytical approximations, this part of the trial function has not been derived from the differential equation itself, but is purely chosen by the shape of the function.

Figure 4.1 shows the the three functions for $R(H)$ that are to form the trial function, as well as the three functions put together. The first (yellow) is the Lambert W-function, and is dominating at low H-values ($R \to \infty$). The second (green) is the hyperbolic tangent function. The position of the sudden change as well as the amplitude and the speed of the change can be adjusted from a total of three parameters in order to fit

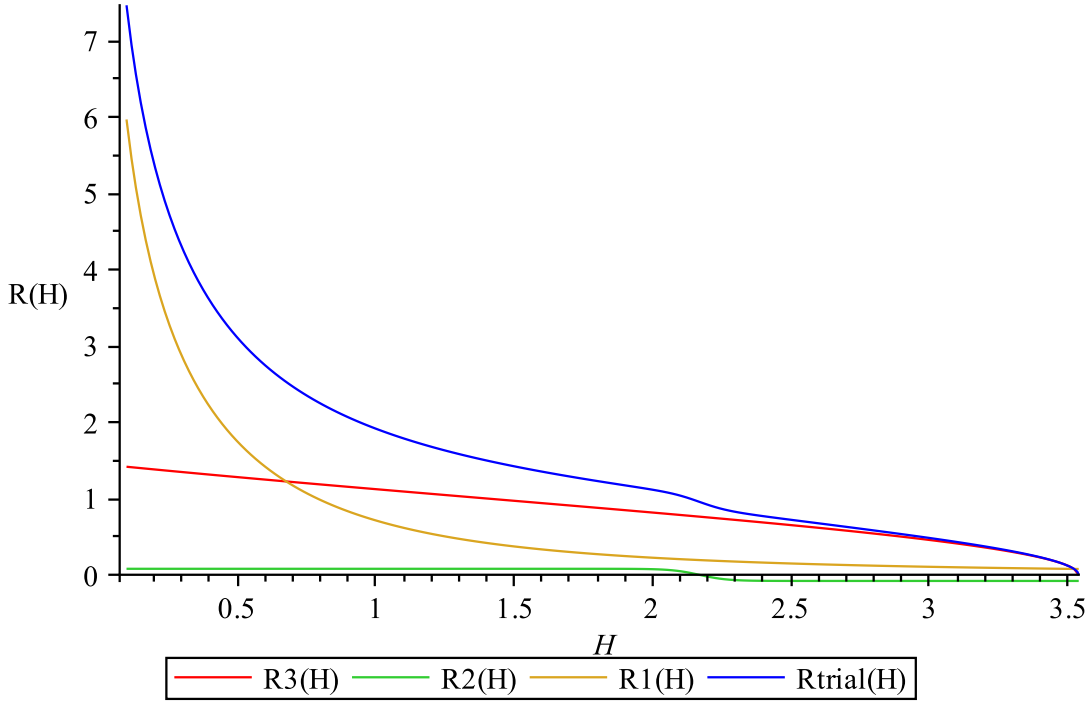

Figure 4.1: The trial function for the case of $P = 1\ 200$ W, $\omega_0 = 4.8\,\mu$m and $T - T_c = 2.5$ K. The maximum value of H is estimated from the experiments in [24], as well as the position of the middle region bend.
– R1(H): The Lambert function, analytical approximation for $R \to \infty$.
– R2(H): A hyperbolic tangent function fitted to the nonlinear shape seen in the experiments of Casner and Delville.
– R3(H): Analytical approximation for $R \to 0$.
– Rtrial(H): R1(H) + R2(H) + R3(H).

each experiment performed by Casner and Delville. The third (red) is the analytical approximation for $R \to 0$. Also this function has an adjustable parameter, namely the maximum deformation depth H_{max}. Because the model for estimating this value from theory was not accurate enough, this parameter will be measured from the experiments of the Bordeaux group. Note that this parameter may have a slight error, due to the inaccuracy during measurements. This means that the solution to the differential equation may be affected by this possible error in the boundary.

The trial function from figure 4.1 (blue) is used as the initial guess for the numerical solver. It is the sum of the three functions mentioned above. The advantage of making this sum is that one function can describe the whole deformation, and both the derivative and the double derivative of the function is continuous. This means that it can easily be

put back into the differential equation in order to investigate the deviation between the actual solution and the trial function. This will be done later in this chapter. In addition, both ends are derived from the differential equation itself, meaning that it satisfies the boundary conditions of the system.

To summarise, the trial function that will be used can be written as:

$$R_{trial}(H) = \frac{W\left(\frac{2\sqrt{B_0}}{H^2}\right)}{2\sqrt{B_0}} + \sqrt{2\left|\ln\frac{(C+B_0H)}{(C+B_0H_{max})}\right|} - \frac{1}{b}\tanh\left(\kappa(H-H_1)\right), \tag{4.1}$$

where $C = (P\Delta n)/(\pi c\sigma\omega_0)$, b is a parameter to adjust the amplitude of the hyperbolic tangent function, κ is a parameter determining how fast the hyperbolic tangent function changes and H_1 is the depth of the middle region sudden change. The parameters b, κ and H_1 will be adjusted to fit each parameter set.

4.3 Results

The numerical solutions will be presented in the following subsections, one for each input parameter set. The input parameters will be chosen to fit some of the experiments performed by Casner and Delville (from the Ph.D. thesis of Casner [24]). By doing this, the numerical solutions can be compared to the experimental results. For each parameter set, two types of boundary condition sets will be used. While Hallanger used that $H \to 0$ as $R \to \infty$ and $H_R \to 0$ as $R \to 0$ as boundary conditions [16], these are not as convenient when solving for $R(H)$. Instead, three boundary conditions will be used in two different combinations.

Boundary conditions, type 1

The first set of the boundary conditions is

$$\begin{cases} R_H \to -\infty & \text{when } H \to 0 \\ R \to 0 & \text{when } H \to H_{max} \end{cases} \tag{4.2}$$

In reality, the computer cannot deal with singularities. Therefore, the boundary conditions are depending on the trial function. Instead of using $-\infty$ for R_H when $H \to 0$, the corresponding value of the trial function will be used:

$$R_H \to \frac{\mathrm{d}}{\mathrm{d}H}(R_{trial}), \quad \text{as } H \to 0. \tag{4.3}$$

A H-value of ≈ 0.05 will be used instead of 0, so that $\frac{\mathrm{d}}{\mathrm{d}H}\big(R_{trial}(0.05)\big)$ is finite. At the other end, the value of R_{trial} will also be used as a boundary condition when $H \to H_{max}$.

Note that a differential equation can have infinitely many solutions, it is the boundary conditions that narrows it down. This means that errors in the boundary conditions

may lead to unwanted solutions. This has to be taken into account when comparing the numerical solutions of the differential equation to the experimental results. The boundary H_{max} itself is also inaccurate, because it has been estimated from the experimental data.

Boundary conditions, type 2

The other set of boundary conditions that will be used is

$$\begin{cases} R \to \infty & \text{when } H \to 0 \\ R \to 0 & \text{when } H \to H_{max} \end{cases} \tag{4.4}$$

Compared to the type 1 conditions, the first boundary condition is replaced with the function $R(H)$ instead of the derivative, $R_H(H)$. The trial function will be used to find corresponding values for ∞ as $H \to 0$.

Comment: what will the depth of the numerical solution be if only the functions $R(0)$ and $R_H(0)$ are given as boundary conditions? An attempt to solve the differential equation with these boundary conditions has also been performed, leaving no information about the case of $H \to H_{max}$. By doing this, the inaccuracy of estimating the value of H_{max} is avoided. However, it turned out be difficult to solve the differential equation for $R(H)$. In fact, only when the differential was rearranged to be a differential equation for $H(R)$ (same as Hallanger), this was made possible. As can be seen from figure 4.2, only the

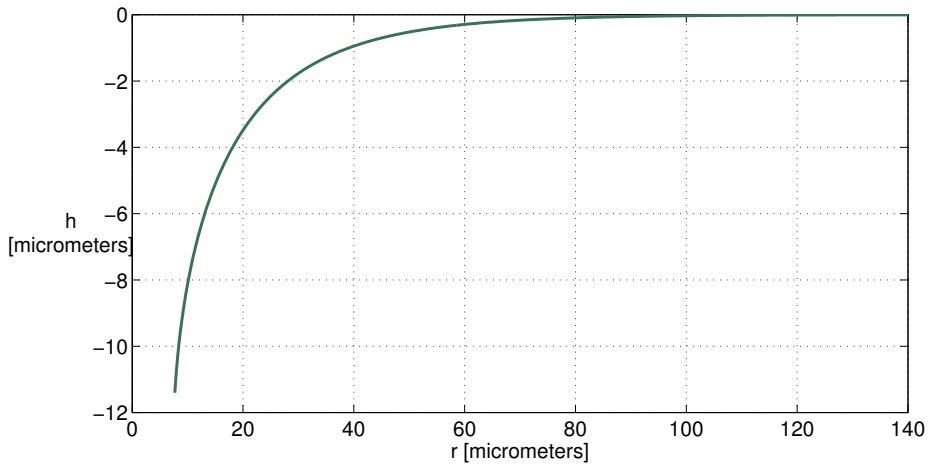

Figure 4.2: Numerical solution of $H(R)$ for $P = 1\,200$ mW, $\omega_0 = 4.8\,\mu$m and $T - T_c = 2.5$ K. Only the boundary conditions for H and H_R at $R \to \infty$ are given (the plot has been converted to h of r). The Lambert function (or inverse) is used as an initial guess. The differential equation could not be solved for smaller values of R with the given boundary conditions.

upper part of the deformation was found with the given boundary conditions, leaving no information of the total depth of the deformation.

Input parameters

As mentioned earlier, different input parameter sets will be used to fit five different experimental setups and results. Some of the parameters are determined by the setup of the experiments (P, ω_0, $T - T_c$, etc.), other are measured from the experimental results.

Below follows a table (table 4.1) with the numerical values of the input parameters.

Set	P	ω_0	$T - T_c$	l_c	B_0	h_{max}	h_1	H_{max}	H_1	κ	b
1	1 200	4.8	2.5	20.3	0.0558	72	44	3.54	2.17	10	4π
2	890	8.9	2.5	20.3	0.1919	54	30	2.66	1.48	10	4π
3	600	4.8	2.5	20.3	0.0558	42.5	17.5	2.10	0.86	10	2π
4	1 200	6.3	2.5	20.3	0.0962	70	42.7	3.45	2.10	10	4π
5	600	6.3	2.5	20.3	0.0962	40	14.4	1.97	0.71	10	π

Table 4.1: Table containing some of the input parameters for the different sets. The laser power P and beam waist ω_0 can be adjusted before the experiment. The liquid-liquid properties are controlled by the temperature difference $T - T_c$. The capillary length l_c, as well as the mass density $\Delta\rho$, the surface tension coefficient σ and the refractive indices are functions of the temperature. The bond number B_0 is the relation between the laser beam waist and the capillary length (squared). The parameters h_{max} and h_1 are measured from the experimental results, and the trial function parameters κ and b, both dimensionless, are set to match the trial function to the experimental results.

4.3.1 Parameter set 1

This and the following subsections include some of the results from the numerical solutions. The green and purple plots are the results using boundary conditions of type 1, while the other plots (yellow and turquoise) are the results using boundary conditions of type 2. All the axes are adjusted to give the deformation in micrometers, meaning that the dimensionless variables R and H are converted back to r and h, respectively.

As can be seen from figure 4.3, the numerical solution gives a much wider deformation than is suggested by the trial function, not least the corresponding experimental results (figure 4.4a). The boundary condition only restricts the deformation to have the same derivative $R_H(H)$ for low H-values (type 1 conditions), and this has resulted in a much broader deformation. The characteristic nonlinear shape for the middle region, which is present in the trial function, is not included in the numerical solution. The depth of the deformation is determined by the boundary condition $R(H_{max}) = 0$. This estimated value is smaller than the maximum depth from the numerical results of Hallanger [16].

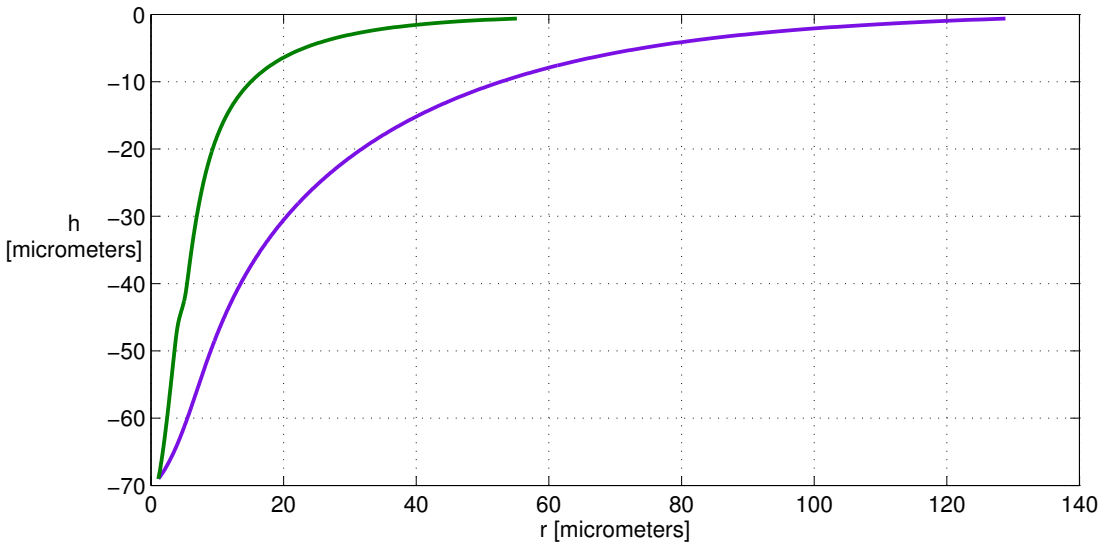

Figure 4.3: Figure showing the numerical results when solving the differential equation from (3.6) with the type 1 boundary conditions and parameter set 1 from table 4.1. The green plot is the trial function, and the purple plot is the numerical solution to the differential equation.

Figure 4.4 shows both a photograph of the deformation from the experiments of Casner and Delville [24] and the numerical results of parameter set 1 and boundary conditions type 2. Compared to the numerical solution in figure 4.3, the deformation is not as wide. The reason is that the boundary condition at $H \to 0$ controls the value of $R(0)$, not $R_H(0)$. However, it may look as the deformation will continue beyond the $H = 0$ limit, which is physically not acceptable. This means that the numerical solution using the type 1 conditions seems to be the most reasonable one.

In the next subsections, the numerical results from the four other parameter sets from table 4.1 are presented. The results are not discussed separately, but a summarise of observations from all the numerical solutions (both boundary condition types and all the parameter sets) are included.

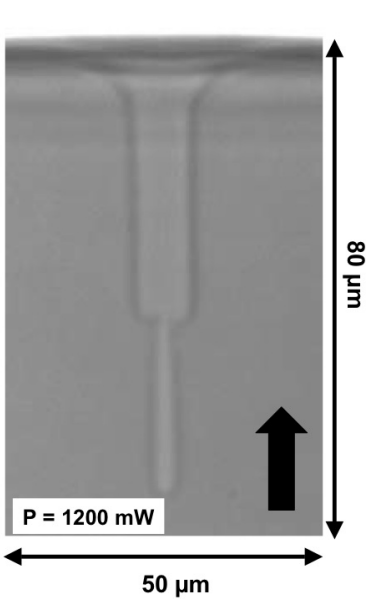

(a) Photograph of the liquid-liquid interface deformation in the case of $P = 1\ 200$ mW, $\omega_0 = 4.8\,\mu$m and $T - T_c = 2.5$ K. From the Ph.D. thesis of Casner [24].

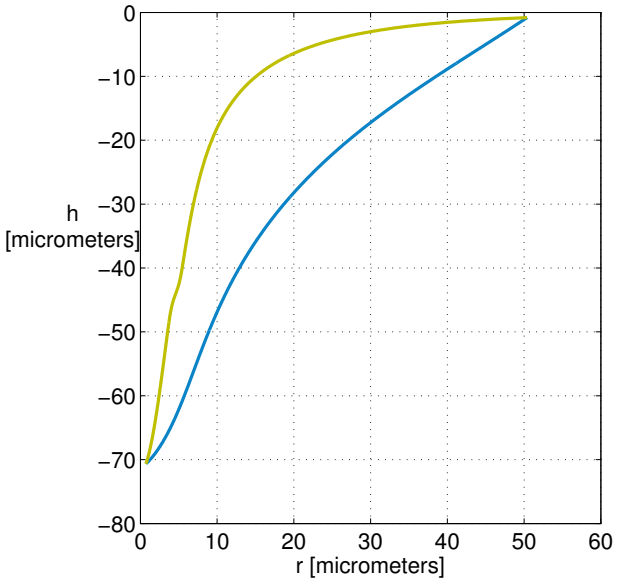

(b) Figure showing the numerical results when solving the differential equation (3.6) with the type 2 boundary conditions and parameter set 1 from table 4.1. The yellow plot is the trial function, and the turquoise plot is the numerical solution.

Figure 4.4

4.3.2 Parameter set 2

Here follows the numerical results of parameter set 2.

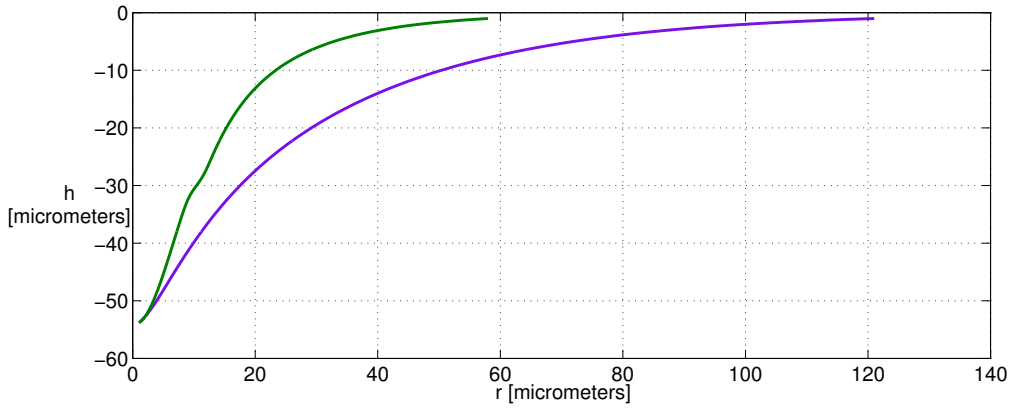

Figure 4.5: Figure showing the trial function (green) and the numerical solution of equation (3.6) for parameter set 2 and boundary conditions type 1. The corresponding experimental result can be seen in figure 4.6a.

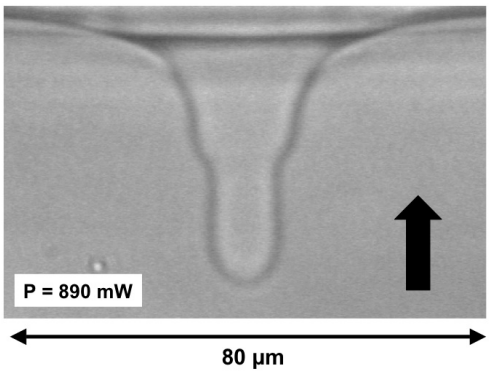

(a) Photograph of interface deformation experiment with laser power $P = 890$ mW, $\omega_0 = 8.9\,\mu$m and $T - T_c = 2.5$ K. From Casner [24].

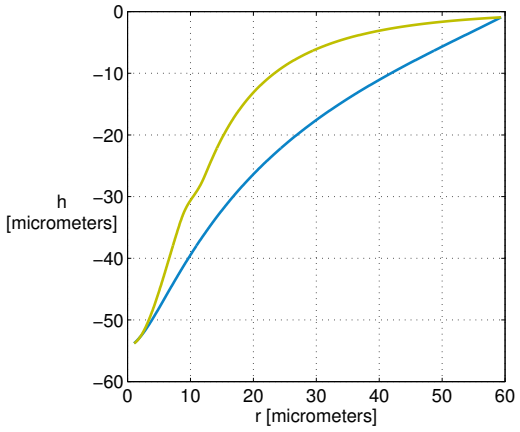

(b) Numerical results using parameter set 2 and boundary conditions type 2. The trial function is yellow and the numerical solution is turquoise.

Figure 4.6

4.3.3 Parameter set 3

Here follows the numerical results of parameter set 3.

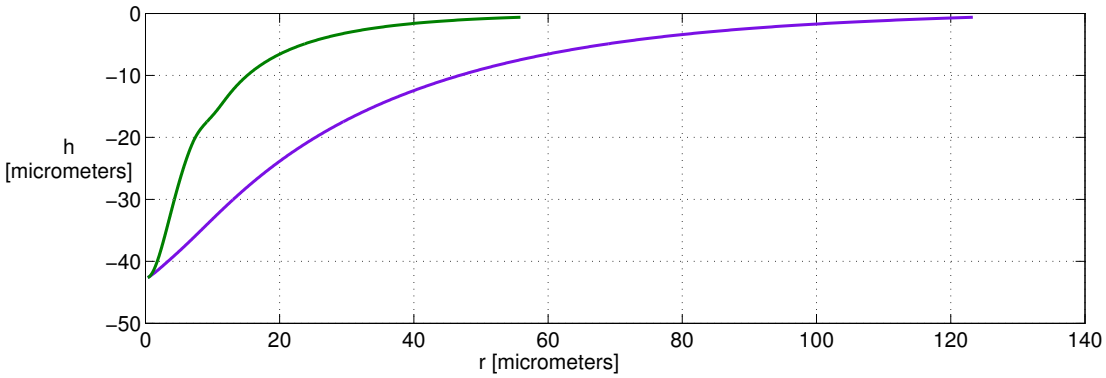

Figure 4.7: Figure showing the trial function (green) and the numerical solution of equation (3.6) for parameter set 3 and boundary conditions type 1. The corresponding experimental result can be seen in figure 4.8a.

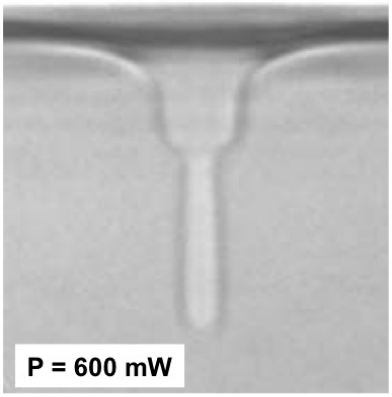

(a) Photograph of interface deformation experiment with laser power $P = 600$ mW, $\omega_0 = 4.8\,\mu$m and $T - T_c = 2.5$ K. From Casner [24].

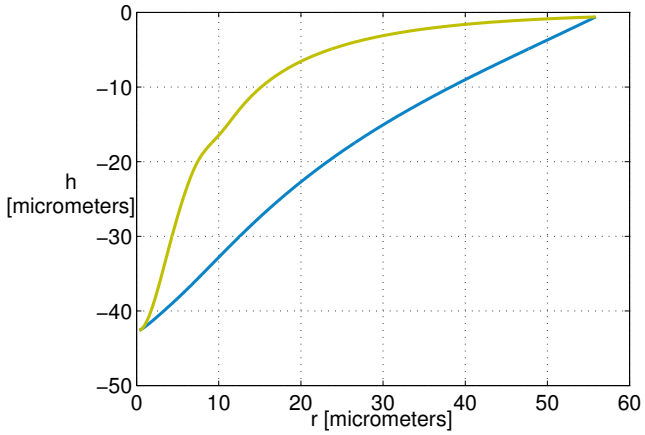

(b) Numerical results using parameter set 3 and boundary conditions type 2. The trial function is yellow and the numerical solution is turquoise.

Figure 4.8

4.3.4 Parameter set 4

Here follows the numerical results of parameter set 4.

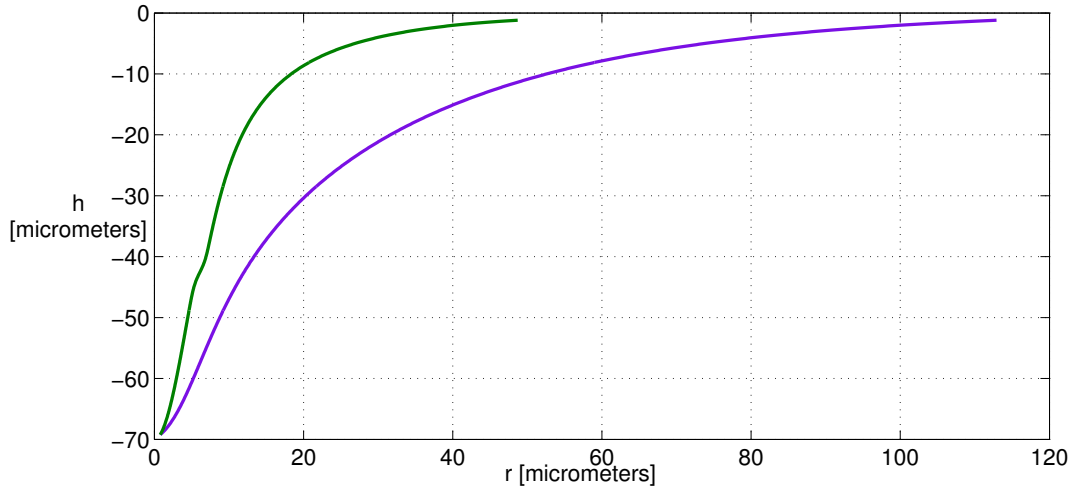

Figure 4.9: Figure showing the trial function (green) and the numerical solution of equation (3.6) for parameter set 4 and boundary conditions type 1. The corresponding experimental result can be seen in figure 4.10a.

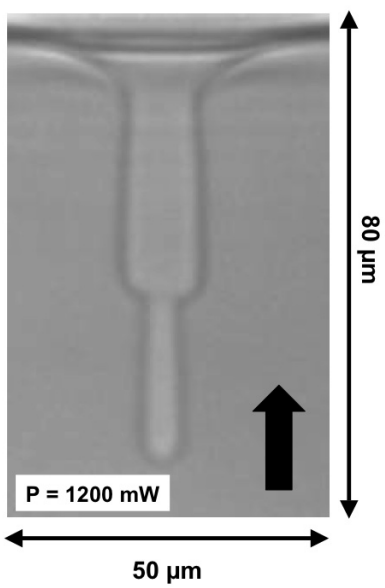

(a) Photograph of interface deformation experiment with laser power P = 1 200 mW, $\omega_0 = 6.3\,\mu$m and $T - T_c$ = 2.5 K. From Casner [24].

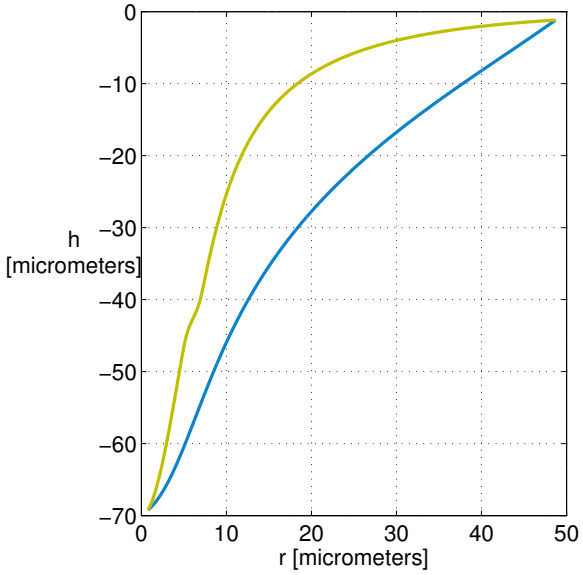

(b) Numerical results using parameter set 4 and boundary conditions type 2. The trial function is yellow and the numerical solution is turquoise.

Figure 4.10

4.3.5 Parameter set 5

Here follows the numerical results of parameter set 5.

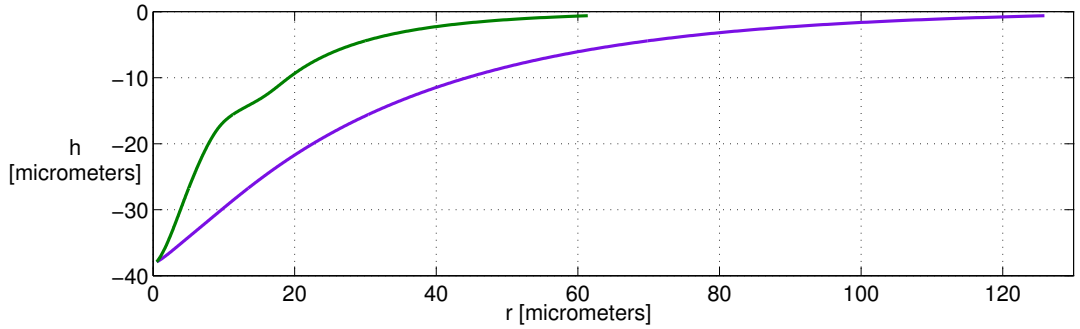

Figure 4.11: Figure showing the trial function (green) and the numerical solution of equation (3.6) for parameter set 5 and boundary conditions type 1. The corresponding experimental result can be seen in figure 4.12a.

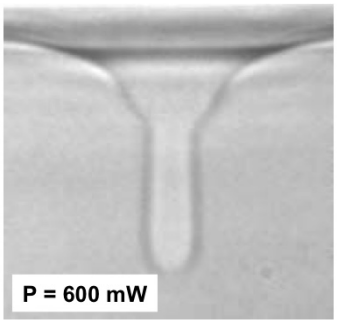

(a) Photograph of interface deformation experiment with laser power $P = 600$ mW, $\omega_0 = 6.3\,\mu$m and $T - T_c = 2.5$ K. From Casner [24].

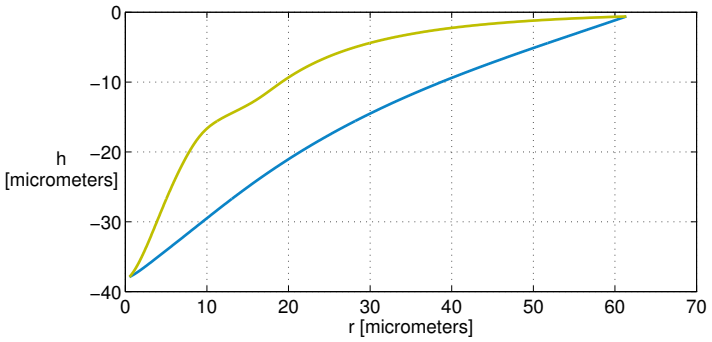

(b) Numerical results using parameter set 5 and boundary conditions type 2. The trial function is yellow and the numerical solution is turquoise.

Figure 4.12

As can be seen from the results presented above, the observations made for the numerical solutions for parameter set 1 are also observable at the other sets. The numerical solutions with boundary condition type 2 may be invalid as it looks like the boundary condition $\lim_{H\to 0} R = \infty$ is not satisfied. It seems like (although the numerical solutions for smaller H-values than is plotted above has not been found) the deformation does not

converge towards $R \to \infty$ for $H \to 0$, as is required by the boundary condition, not least the physical properties of the liquid-liquid system.

Another observation is that the numerical deformations are too wide compared to the experimental results. This is the case for both the boundary condition types (1 & 2), even though the maximum width is restricted in the boundary condition type 2.

The last, and maybe most important observation for the purpose of the present text, is that the numerical solutions do not include the "shoulder" in the middle region, even though this is present in the trial function (initial guess). Further investigations are therefore needed in order to find the class of solutions to the differential equation which contains this "shoulder". There is also a possibility that the nonlinear shoulder-shaped deformation is not a solution to the presented differential equation that is assumed to describe the liquid-liquid interface deformations.

The next two sections contain a brief discussion of both possibilities, that further investigations can lead to another solution with the observed middle region shoulder, and that it is not possible to find this solution from the differential equation in (3.6).

4.4 Dependence of the middle region in the trial function

This section investigates the possibility of finding a numerical solution containing the middle region "shoulder" by changing the trial function. The boundary conditions will be kept the same as before. The hyperbolic tangent component of the trial function has three parameters that can be adjusted in order to change the appearance of middle region "shoulder" in the trial function (equation (4.1)). The first is b, a parameter that determines the amplitude of the hyperbolic tangent function. The second, κ, determines how fast the middle region changes (how sharp the "shoulder" is). The third parameter, H_1, determines at which H-value the "shoulder" is placed. These parameters have been adjusted in order to make the trial function qualitatively (if not completely quantitatively) look like the corresponding experimental result. But these parameters can also be adjusted freely (one by one, or simultaneously) in order to see if the numerical result depends on these parameters in the initial guess. In other words; can a change in the part of the trial function that describes the middle region "shoulder" result in a different numerical solution?

In the following subsections, the three different parameters κ, b and H_1 will be varied, and the numerical solutions will be compared to each other. Parameter set 1 and boundary condition type 1 will be used as a starting point, and then one middle region parameter at a time will be changed.

Changing κ

First, the parameter that controls how sharp the "shoulder" in the trial function is, κ, will be investigated further. According to parameter set 1, κ has a value of 10. A higher value will lead to a sharper change in the middle region, whereas a smaller value leads to a slow change. Figure 4.13 shows the trial function with three different values of κ (10, 25 and 0), and the corresponding numerical solutions.

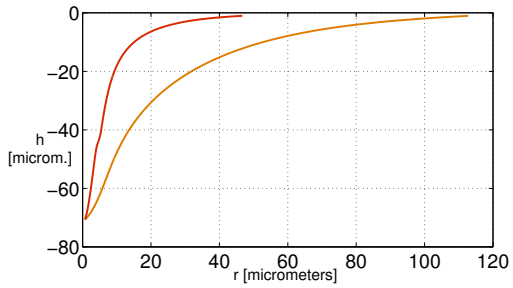

(a) $\kappa = 10$ (standard)

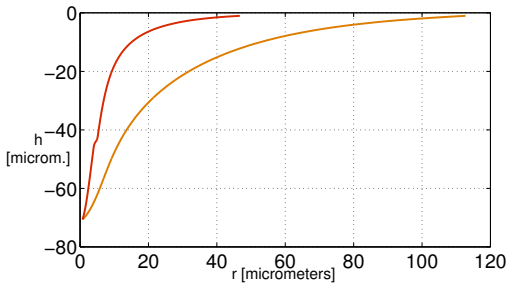

(b) $\kappa = 25$

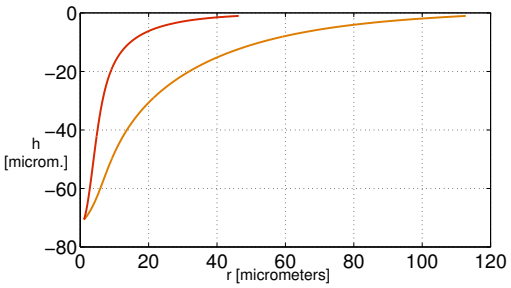

(c) $\kappa = 0$

Figure 4.13: Figure showing the trial function (red) with three different values of κ, the parameter that changes the sharpness of the middle region "shoulder" and the corresponding numerical solutions (orange). In the first plot (4.13a), the standard parameters (parameter set 1) is used. In the second (4.13b), κ is increased to 25. The last plot shows the case of $\kappa = 0$, meaning that there are no shoulder in the trial function.

As can be seen from figure 4.13, the numerical solutions are the same independent of how sharp the "shoulder" in the trial function is. This was also confirmed by solving for other values of κ than those used to obtain the results presented here, as well as changing the boundary condition type to 2 (and then solve for different values of κ). The nonlinear numerical solution containing the middle region "shoulder" can in other words not be found by changing the trial function parameter κ.

Changing b

The second parameter to be changed is b. This parameter controls the amplitude or range of the hyperbolic tangent function. The smaller b is, the larger the amplitude becomes. This parameter will ultimately also have a minor impact on the value H_{max}, slightly changing the boundary condition for $R = 0$. The numerical solutions for different values of b are therefore expected to be slightly different. The question is, however, if a change in b can result in a different type of numerical solution, a type that includes the middle region "shoulder".

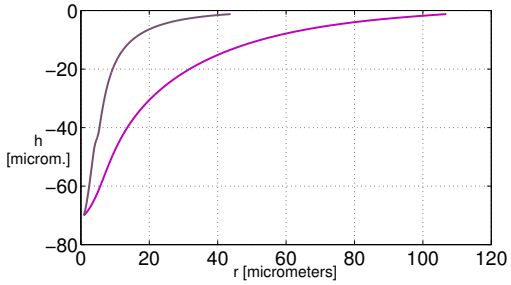

(a) $b = 4\pi$ (standard)

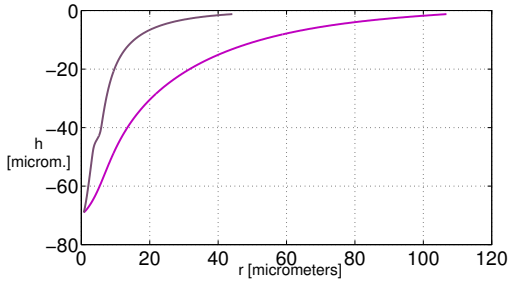

(b) $b = 2\pi$

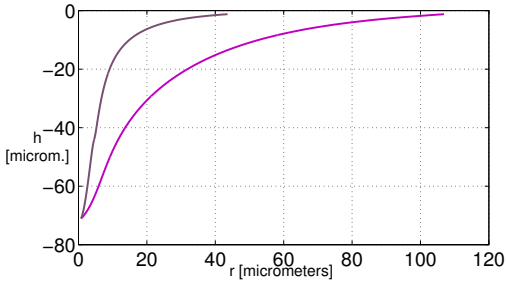

(c) $b = 8\pi$

Figure 4.14: The trial function (dark purple) with three different amplitudes in the hyperbolic tangent function and the corresponding numerical solutions (pink / purple). A change in the amplitude is adjusted by the parameter b in equation (4.1). A change in b will also change the point where R is 0, namely the value of H_{max} slightly. In the three plots, the parameter b varies from 2π to 8π, where 2π results in the largest amplitude.

By investigating figure 4.14, it can be seen that the point where $R = 0$ varies somewhat, as expected. There is, however, no change in the type of shape of the numerical solutions. None of the plots in this figure (or other plots that are not included here) have a "shoulder" present in the numerical solutions. There is therefore no reason to believe that a change in the amplitude of the hyperbolic tangent function in the trial function will lead to a different type of numerical solution of the differential equation (3.6).

Changing H_1

The last parameter that will be investigated more closely controls the position (H-value) of the "shoulder" in the trial function, namely H_1. The standard value for H_1 in parameter set 1 is 2.17 (plot 4.15a), but the case of $H_1 = 1.5$ and $H_1 = 2.8$ are also included (plot 4.15b and 4.15c, respectively).

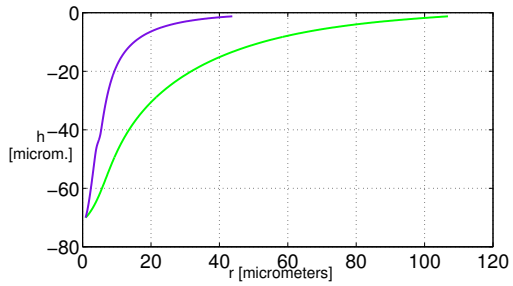

(a) $H_1 = 2.17$ (standard)

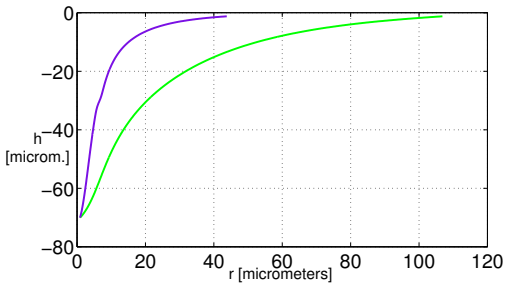

(b) $H_1 = 1.5$

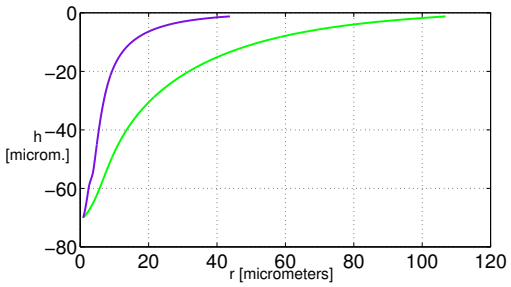

(c) $H_1 = 2.8$

Figure 4.15: Figure showing the trial function (purple) with corresponding numerical solution (green) in three different cases. Parameter set 1 with boundary condition type 1 is used, but the parameter H_1 changes in order to move the position (H-value) of the middle region "shoulder" in the trial function.

The observation from changing the position of the "shoulder" (parameter H_1) is the same as for the change of κ; the numerical solution to the differential equation (3.6) is not depending on the parameter H_1, the position of the "shoulder", in the trial function. The same result was obtained using boundary type 2 (not shown here).

After investigating the parameters that controls the shape of the middle region in the trial function more closely, it can be concluded that the type of numerical solution to the differential equation (3.6) does not depend on the middle region of the trial function from equation (4.1) and the middle region "shoulder". This does not mean that there are no chance of finding a numerical solution to the given differential equation that do include the complex shape of the middle region that is observed in the experiments of the

Bordeaux group. It is, however, reason to believe that this solution (if it exists) only can be found by changing the trial function (initial guess) entirely or by changing the way the boundary conditions are given. This attempt will not be performed in this present text, but may be a suggestion for further work.

4.5 Numerical solutions with the middle region "shoulder"

Now, as it may look like the trial function used is not capable of leading to the type of numerical solution that is searched for, it seems reasonable to investigate what may be the main problem with the initial guess. By doing this, two answers will be searched for. Is there a solution to the differential equation in (3.6) that contains the middle region "shoulder"? What should the trial function look like in order to find this solution?

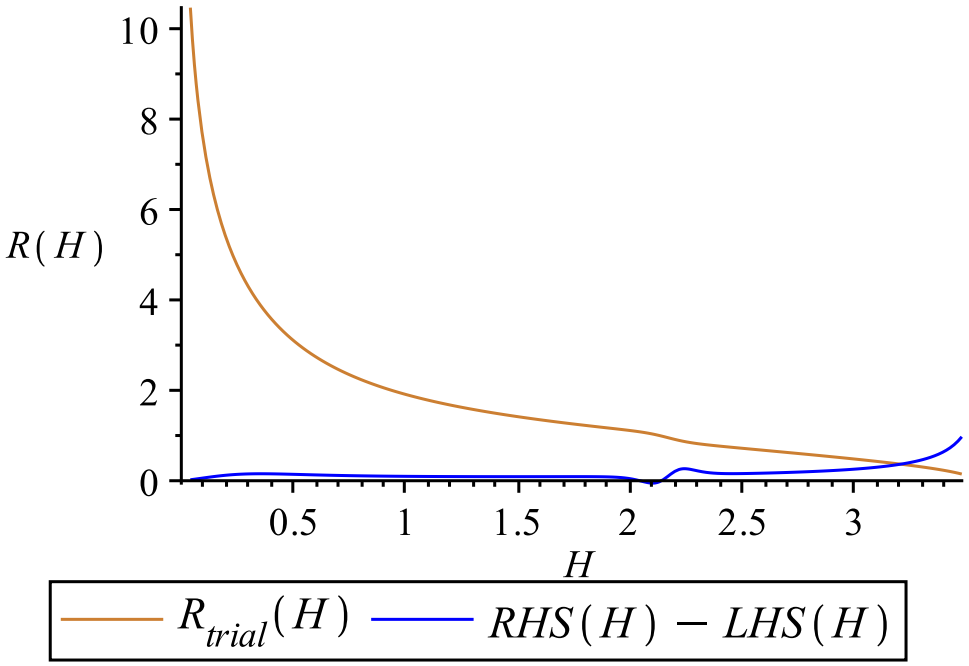

Figure 4.16: Figure showing the trial function (gold) and the right hand side minus the left hand side of the differential equation from (3.6) with the trial function inserted (blue) for parameter set 1. The height (or depth) H is along the x-axis, and the radius R follows the y-axis. As can be seen, the difference between the right hand side and the left hand side of the equation increases at the middle region "shoulder" of the trial function. At $H \to 0$, the difference goes to 0.

The method that will be used to check the trial function is based on the advantage of the

trial function given in (4.1), that one continuous function describes the whole deformation. Then, the derivative of the trial function (and the second derivative) can be found and put back into the differential equation in (3.6). By taking the difference between right hand side and the left hand side of the differential equation (with the trial function put into it), an estimate on how wrong the trial function is can be achieved. A function that satisfies the differential equation will give $RHS(H) - LHS(H) = 0$ for all H-values.

Figure 4.16 shows the trial function for parameter set 1 (gold) and the difference $RHS(H) - LHS(H)$ with the trial function put in (blue). The difference is close to zero for low H-values, up to the middle region "shoulder". In fact, it converges to zero as $H \to 0$, meaning that the trial function satisfies the differential equation at $H \to 0$. At $H = H_1$, where there is a sudden change in the trial function (the "shoulder"), the difference $RHS - LHS$ increases. This may indicate that the differential equation does not tolerate the shape of a "shoulder", but it can also mean that the "shoulder" should be placed differently, that the amplitude or sharpness of it should be changed, or that the hyperbolic tangent function is not suitable to describe the middle region of the deformation (there are other functions with the same shape, for instance $\arctan(x)$).

The corresponding plots for parameter set 2 – 5 are given in figure 4.17. Also here, it seems like the difference between the right hand side and the left hand side of equation (3.6) increases where the "shoulder" is placed. Another observation is that the difference $RHS - LHS$ increases towards the bottom of the trial function deformation, at $H \to H_{max}$. This may indicate that the parameter H_{max} is measured inaccurately from the experimental results in [24]. It may also indicate that the approximative analytical solution for this area is not accurate.

The two areas of interest from the plots in figure 4.16 and 4.17, the middle region and the end, will be investigated a bit more closely in the following subsections.

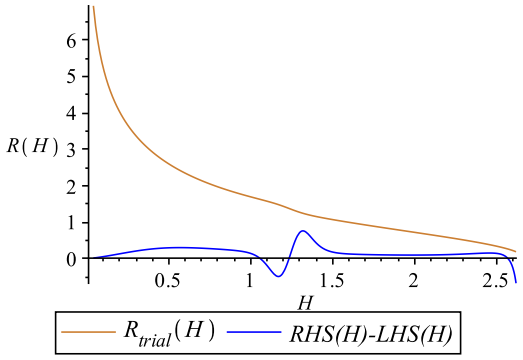

(a) Parameter set 2

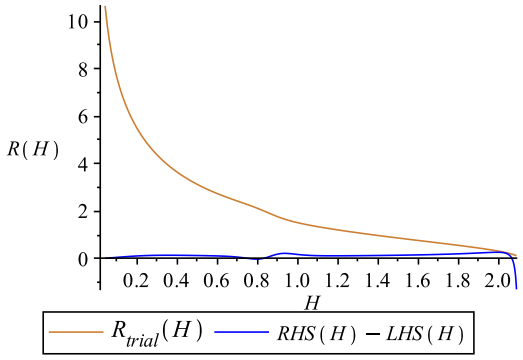

(b) Parameter set 3

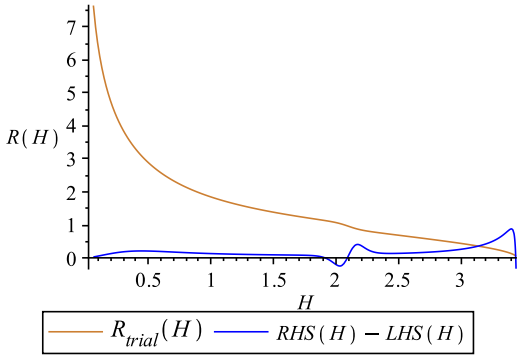

(c) Parameter set 4

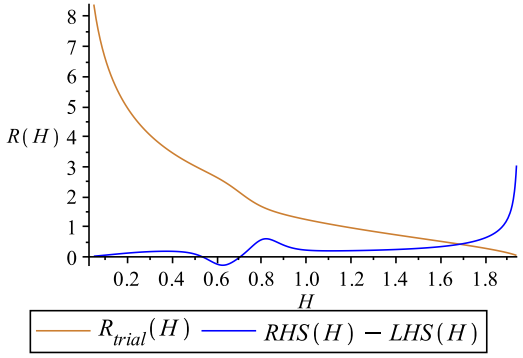

(d) Parameter set 5

Figure 4.17: Figure showing the trial function (gold) and the right hand side minus the left hand side of the differential equation from (3.6) with the trial function inserted (blue) for parameter set 2 to 5 (see table 4.1). The height (or depth), H, is along the x-axis, and the radius R follows the y-axis. As can be seen, the difference between the right hand side and the left hand side of the equation increases at the middle region "shoulder" of the trial function. At $H \to 0$, the difference goes to 0.

4.5.1 The middle region "shoulder"

Again, parameter set 1 will be used as a starting point. Similar to section 4.4, the three parameters that controls the middle region of the trial function will be changed one by one in order to see how the difference between the right hand side and the left hand side of the differential equation depends on these parameters.

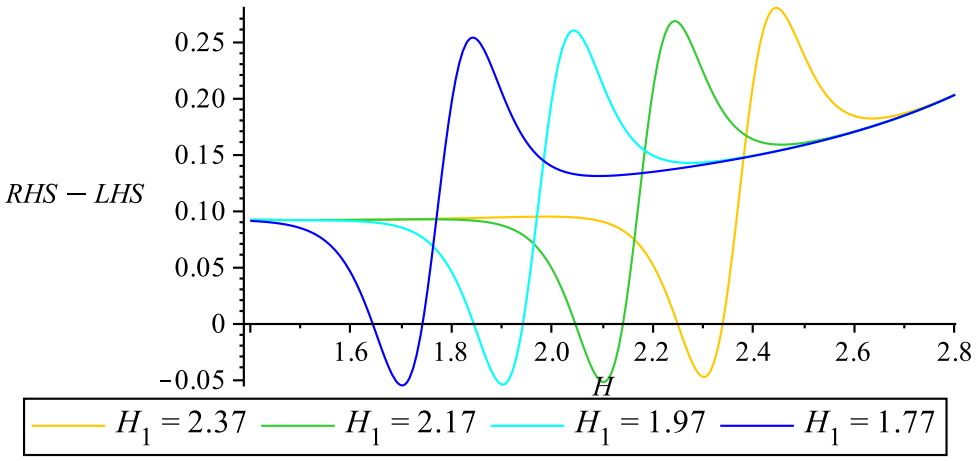

Figure 4.18: Figure showing the function $RHS(H) - LHS(H)$ with the trial function in equation (4.1) put in. Parameter set 1 is used as a starting point, buth the middle region paramter H_1, which controls the position of the middle region "shoulder", varies from 1.77 to 2.37 ($H_1 = 2.17$ is used for the numerical solution).

Figure 4.18 shows the function $RHS(H) - LHS(H)$ with the trial function from equation (4.1) put in, using four different values of H_1 (the rest of the parameters from set 1). The parameter H_1 controls the position of the middle region "shoulder" in the trial function, and the shown H-values are close to H_1 (see figure 4.16 for a larger H-range). As can be seen, a change in H_1 does not lead to a larger deviation between the right hand side and the left hand side of the differential equation (3.6), but only changes the position of the "shoulder" response observed in figure 4.16.

The next parameter to investigate is κ. This parameter controls the sharpness of the "shoulder" in the trial function. In figure 4.19, κ varies between 0 and 30, and four plots of the difference between the right hand side and the left hand side of the differential equation (3.6) are shown. The red plot shows the case of $\kappa = 0$, which corresponds to no middle region "shoulder" in the trial function. As can be seen, this case shows more agreement between the right hand side and the left hand side for the middle region than the other plots. The case of $\kappa = 30$ gives the largest deviation, meaning that the trial function is farther away from satisfying the differential equation in the case of large κ-

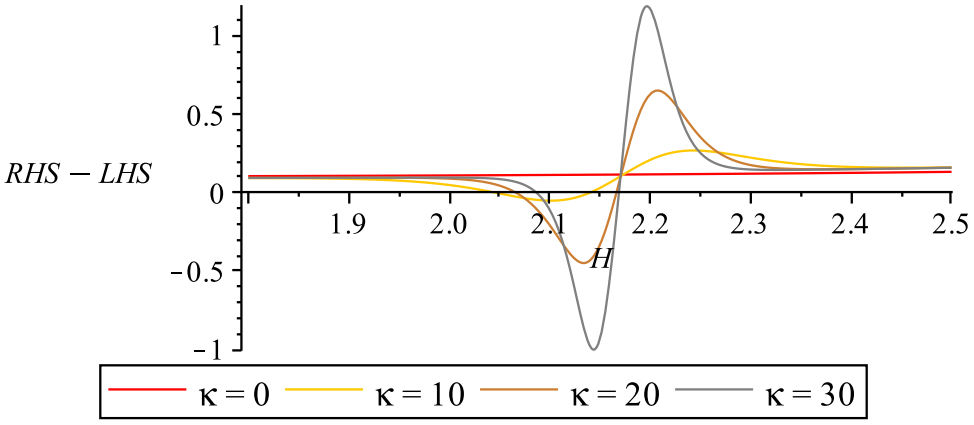

Figure 4.19: Figure showing the function $RHS(H) - LHS(H)$ with the trial function in equation (4.1) put in. Parameter set 1 is used as a starting point, buth the middle region paramter κ, which controls the sharpness of the middle region "shoulder", varies from 0 to 30 ($\kappa = 10$ is used for the numerical solution). Note that $\kappa = 0$ corresponds to no middle region "shoulder".

values. The width of the middle region "shoulder" deviation in the four plots are almost the same, but a small value of κ gives a slightly broader middle region deviation than a larger κ-value.

The last parameter is b, the amplitude of the middle region "shoulder". Figure 4.20 shows four plots of $RHS - LHS$ with parameter set 1, but with b varying from π to 8π. Remember that a larger value of b corresponds to a smaller value of the amplitude (see equation (4.1)). As can be seen, the larger the amplitude of the trial function "shoulder" is, the larger and wider the difference $RHS - LHS$ is for the same area.

After investigating how the difference between the right hand side and the left hand side of the differential equation in (3.6) with the trial function from (4.1) put in varies with the three parameters b, κ and H_1, some conclusions can be made. The trial function does not satisfy the differential equation in the middle region with the "shoulder" parameters given in set 1. If the amplitude $(1/b)$ and the sharpness (κ) of the hyperbolic tangent function increases, the difference $RHS - LHS$ grows larger for the middle region. In fact, the difference is smallest if $\kappa = 0$, meaning that there is no "shoulder" in the middle region of the trial function. In other words, it may seem like the differential equation does not allow any shoulder-shaped solutions. It should be stressed that the middle region of the trial function is based on a function that is chosen based on the looks; it is chosen to make the trial function look (qualitatively) like the experimental results of Casner and Delville. This may explain why it does not satisfy the differential equation,

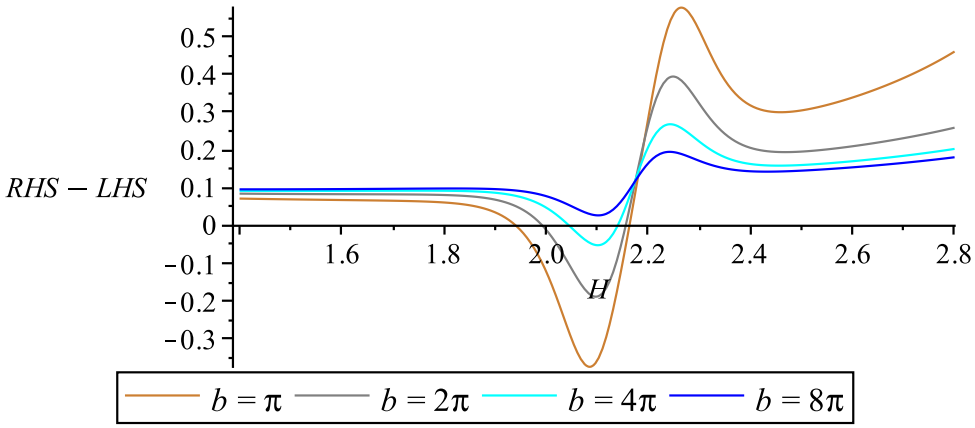

Figure 4.20: Figure showing the function $RHS(H) - LHS(H)$ with the trial function in equation (4.1) put in. Parameter set 1 is used as a starting point, buth the middle region paramter b, which controls the amplitude of the middle region "shoulder", varies from π to 8π ($b = 4\pi$ is used for the numerical solution).

because it is not derived directly from the differential equation as the two other parts of the trial function. The difference $RHS - LHS$ is a function on R_H and R_{HH} as well as R, so a small error in R may escalate to larger errors in the derivatives. There is, however, some reason to believe that the trial function is closest to a solution of the differential equation without the "shoulder" that has been observed in the experiments of the Bordeaux group.

4.5.2 The analytical approximation at H_{max}

The last investigation of this section, as well as the chapter, is to briefly check what happens if the parameter H_{max} is changed. This value is approximated from measuring the experimental results in [24], but it can be chosen freely in order to check whether the difference between the right hand side and the left hand side of the differential equation in (3.6) becomes smaller. In figure 4.21, the function $RHS - LHS$ is shown for four different H_{max}-values in the trial function. All four H_{max}-values are in the vicinity of the H_{max}-value estimated in table 4.1. Based on these plots, it seems like the size of the deviation observed and discussed near H_{max} in figure 4.16 is not depending on the parameter H_{max}, it just changes position. This means that the deviation may come from the second term in the trial function, the analytical approximation for $H \to H_{max}$. This approximation may not be as accurate as hoped for, but the numerical results from section 4.3 behaves satisfactorily towards $R \to 0$ and $H \to H_{max}$. There is therefore no reason to change this part of the trial function.

Comment: what if the second term in the trial function is removed? Can the parameter

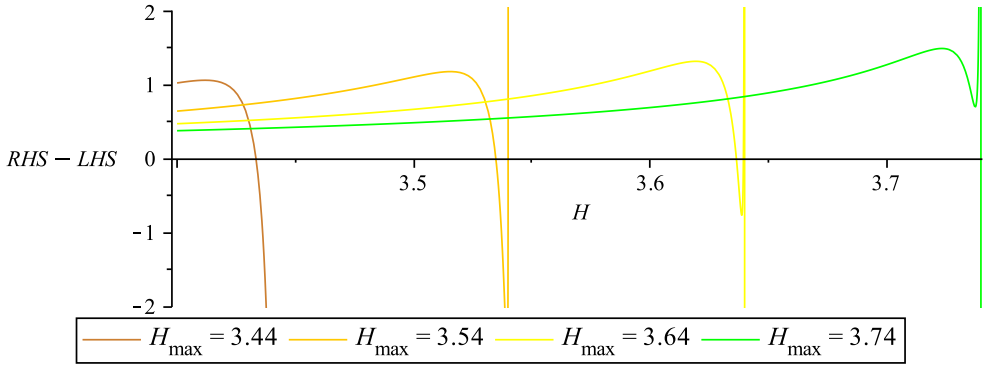

Figure 4.21: Figure showing the difference between the right hand side and the left hand side of the differential equation in (3.6) with the trial function in (4.1) put in. Parameter set 1 is used, but the value of H_{max} is varied from 3.44 to 3.74.

H_{max} then be estimated from the difference $RHS - LHS$? In figure 4.22, the second term of the trial function is removed so that

$$R_{trial}(H) = \frac{W\left(\frac{2\sqrt{B_0}}{H^2}\right)}{2\sqrt{B_0}} - \frac{1}{b}\tanh\left(\kappa(H - H_1)\right) + 0.5. \tag{4.5}$$

The constant 0.5 is put in to avoid that $R(H)$ is 0 for several values of H. Then, the right hand side minus the left hand side of the differential equation in figure 4.22 is behaving differently compared to the previous case (see figure 4.16). The difference seems to be changing at a constant rate for $H > 3$, and there are still no indication of where the end (maximum depth) of the deformation should be.

4.6 Conclusions to the numerical solutions

There may be several types of functions that describe the middle region of the deformation containing the "shoulder" more satisfactorily than the hyperbolic tangent function used here. The same can be said about the analytical approximation used for $H \to H_{max}$, not least the resulting trial function itself. It should be mentioned, however, that by using the boundary condition type 1, the numerical solutions are behaving as wanted in the two boundaries; the converge towards $H \to 0$ for $R \to \infty$ and $R_H \to -\infty$ at $H \to H_{max}$ (these properties are not given in boundary condition type 1, but are boundary conditions of the system).

There are two main deviations between the numerical solution obtained in this chapter and the corresponding experimental results. The first is that the numerical deformation is too wide compared to the experimental results. The other is that the observed middle region "shoulder" is not included in the numerical results, even though it is present in

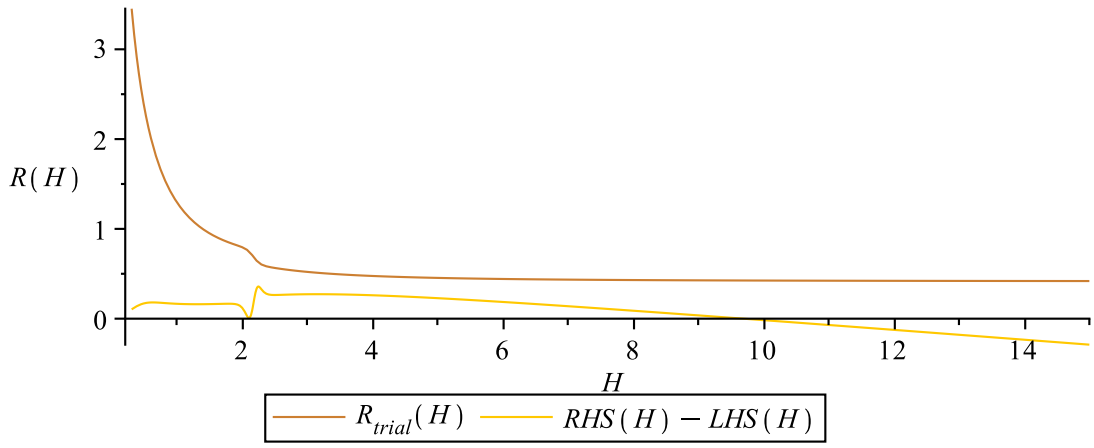

Figure 4.22: Figure showing the trial function from (4.5) and the corresponding $RHS - LHS$ of the differential equation in (3.6) with the trial function put in. There are no clear indication to where the maximum depth H_{max} should be, based on investigation of the difference $RHS - LHS$.

the initial guess (trial function). Further investigations by putting the trial function used (equation (4.1)) into the differential equation in (3.6) have suggested that there is a possibility that the differential equation does not accept a middle region "shoulder". This means that the differential equation used for the liquid-liquid interface system may be too simple to describe the nonlinear deformations. If this is the case, a new and more extensive differential equation must be derived before further numerical investigations can be performed. There may, for instance, be some laser-induced local temperature variations, causing a change in the surface tension coefficient σ, the mass densities and the refractive indices. All these parameters are temperature dependent. Whether or not the laser is causing temperature variations can be checked by performing the liquid-liquid interface bending experiments while using heat sensitive cameras.

It should be stressed, however, that it has not been proven that the differential equation does not have any solutions containing the nonlinear shoulder-shape observed in the experiments of Casner and Delville.

Chapter 5

Conclusions

In the previous chapters, the theory of laser-induced liquid-liquid interface deformation has been presented and used to derive a differential equation describing the system. Then, this differential equation has been investigated and prepared for numerical solution. Finally, the differential equation has been solved numerically and the results are compared to the experimental results of the Bordeaux group [24]. The main focus has been the cases where a nonlinear shoulder-shaped deformation is observed from experiments, and which have not been reproduced numerically (or analytically) from theory. The numerical results from this present text have also been compared to the numerical results of Hallanger [16]. A model (see appendix B) that describes what the maximum depth H_{max} of the deformation is given the bottom width of the deformation has also been tested. The model is based on the theory of a sphere (or hemisphere) in an electric field.

5.1 Finding H_{max} from theory

If the bottom part of the liquid-liquid interface deformation is assumed to have the shape of a hemisphere, the total radiation force can be calculated by using the theory of the forces on a hemisphere from an incoming electric field. Then, the total depth of the deformation can be estimated by balancing the calculated radiation force with the buoyancy and the surface tension. A model developed by Iver Brevik during the spring 2011 (appendix B) has been tested for some of the parameter sets used in the Ph.D. thesis of Casner [24] in order to find the maximum depth H_{max} from theory rather than measuring it from experimental results. It seems, however, like the model is not in good agreement with the experimental results, as the calculated H_{max} turns out to be at least 100 times larger than the measured value. A parameter dependence investigation showed that the sum Q given in (B.96) or (3.34) (in other words, the radiation force) behaves as expected for the laser-induced liquid-liquid interface deformation system.

The main problem with the model is believed to be that some of the assumptions made are not valid for hemispheres, although they seem to be correct for spheres. One example is

the assumption that only $l = l'$ will contribute to the sum (see equation (B.79)). There may also be some resonance terms in Q that should not be included (see figure 3.3). Further investigations to why the model does not work should be performed in order to make improvements to the model. There are (to this writer's knowledge) no other models available that leads to the parameter H_{max} from theory.

5.2 Numerical results and the appearance of a middle region "shoulder"

A differential equation was derived based on the theory of the forces that play an important role in the liquid-liquid interface deformations. This differential equation was then solved numerically with the given boundary conditions (presented in two different ways, type 1 and 2) and a trial function. Five parameter sets were used based on five different experiments from the Ph.D. thesis of Casner [24]. The obtained numerical solutions were found to give too wide deformations compared to the corresponding experimental results. In addition, the shoulder-shape that is observed for the middle region of the deformation in nonlinear cases is not present in the numerical solutions.

Further investigations showed that the numerical solution to the differential equation with the given boundary conditions does not depend on the middle region of the trial function and the parameters determining the properties of the shoulder-shape. In fact, when putting the trial function into the differential equation and studying the difference between the right hand side and the left hand side of the equation, there is best agreement when the trial function is given without the "shoulder" (the case of $\kappa = 0$). This may indicate that the differential equation does not have any solutions containing the middle region shoulder-shape that is observed in the experiments. If this is the case, the differential equation believed to describe the liquid-liquid interface deformations may not be valid for nonlinear deformations, even though it seems to be describing the linear deformations satisfactorily: The numerical solutions of the differential equation (same as used here) achieved by Hallanger et al. ([16], [15]) are in good agreement with the experiments using low laser powers ($P < 200$ mW), but as the power increases, the numerical results do not match the experimental deformations.

The nonlinear deformations with larger laser powers may be more complex, requiring more details and locally adjusted parameters. One possibility, as was also mentioned by Hallanger, Brevik, Haaland & Sollie [15], is that there may be some thermal effects. The liquid properties are closely related to the temperature, meaning that a slight change in temperature leads to different surface tension, mass densities and refractive indices. There is a possibility that the laser beam will cause local variations in the liquid temperature, meaning that the liquid properties will change along the deformation so that

$$\sigma \to \sigma(r), \qquad \Delta\rho \to \Delta\rho(r), \qquad \Delta n \to \Delta n(r). \tag{5.1}$$

Then, the differential equation in (3.6) must be modified and becomes even more complex. There may also be other reasons to why the differential equation does not contain any shoulder-shaped solutions, if this is the case. The laser intensity distribution may be too simple, or there may be some other effects making an influence on the liquid-liquid system with an incoming laser beam. Whether or not there are significant laser-induced temperature variations, can be checked by performing liquid-liquid interface bending experiments with heat sensitive cameras to check if the temperature is constant or not.

Note that the investigations in this text has not shown that the differential equation used to describe the laser-induced liquid-liquid interface deformation does not include a nonlinear shoulder-shaped solution. The numerical results and further investigations have only suggested the possibility that the differential equation may be too simple in order to describe the nonlinear deformations satisfactorily.

5.3 Further work

Further work should include a review of the model tested in chapter 3 (see also appendix B). The possibility that not only the $l = l'$ terms in Q contribute to the total radiation force on a hemisphere should be investigated more closely. There may also be other factors that make the model unsuitable for estimating the value of H_{max}. If the maximum depth of the deformation can be predicted from theory, this will be a large step towards making a full theoretical description of the laser-induced liquid-liquid interface deformations.

As the numerical solutions including the nonlinear shoulder-shape were not found in this work, further effort should be put into this task. This may be done by performing the numerical calculations in a more elegant way than is presented here, but there may also be a chance that the differential equation itself is not describing the liquid-liquid interface deformations for nonlinear cases (laser power $P > 300$ mW). If this is the case, a more complex differential equation must be derived including more details concerning local temperature variations and possibly other aspects.

Appendix A

Calculations from the theory section

In this appendix, detailed calculations of some of the equations are presented.

A.1 $\sigma^{AM}(\theta_i, \theta_t) \to \sigma^{AM}(h_r)$, equation (2.30).

$$
\begin{aligned}
\sigma^{AM} &= -\frac{I}{2c}\frac{n_{in}^2 - n_{out}^2}{n_{in}}\frac{\cos\theta_i}{\cos\theta_t}\left[(\cos^2\theta_t + \sin^2\theta_i)T_{\parallel}\cos^2\alpha + T_{\perp}\sin^2\alpha\right] \\
&= -\frac{I}{2c}\frac{n_{in}^2 - n_{out}^2}{n_{in}}\frac{4a\cos^2\theta_i\cos\theta_t}{\cos\theta_t(\cos\theta_t + a\cos\theta_i)^2}\left[\frac{(\cos^2\theta_t + \sin^2\theta_i)\cos^2\alpha}{(\cos\theta_i\cos\theta_t + a\sin^2\theta_i)^2} + \sin^2\alpha\right] \\
&= -\frac{2I}{c}\frac{n_{in}^2 - n_{out}^2}{n_{in}^2}\frac{n_{out}}{\left(\frac{\cos\theta_t}{\cos\theta_i} + a\right)^2}\left[\frac{(1 + h_r^2(1-a^2) + h_r^2)(1+h_r^2)\cos^2\alpha}{\left(\sqrt{1+h_r^2(1-a^2)} + ah_r^2\right)^2} + \sin^2\alpha\right] \\
&= -\frac{2I}{c}\frac{n_{in}^2 - n_{out}^2}{n_{in}^2}\frac{n_{out}}{\left(a + \sqrt{1+h_r^2(1-a^2)}\right)^2}\left[\frac{\left(1 + (1-a^2+1+1)h_r^2 + (1+1-a^2)h_r^4\right)\cos^2\alpha}{\left(ah_r^2 + \sqrt{1+h_r^2(1-a^2)}\right)^2} + \sin^2\alpha\right] \\
&= -\frac{2I}{c}\frac{n_{in}^2 - n_{out}^2}{n_{in}^2}\frac{n_{out}}{\left(a + \sqrt{1+h_r^2(1-a^2)}\right)^2}\left[\frac{1 + (3-a^2)h_r^2 + (2-a^2)h_r^4}{\left(ah_r^2 + \sqrt{1-h_r^2(1-a^2)}\right)^2}\cos^2\alpha + \sin^2\alpha\right]
\end{aligned}
\tag{A.1}
$$

A.2 $\sin^2\alpha = \cos^2\alpha = \frac{1}{2}$, equation (2.34).

$$
\begin{aligned}
f(a,h_r,\alpha) &= \frac{(1+a^2)}{\big(a+\sqrt{1+h_r^2(1-a^2)}\big)^2}\left[\frac{1+(3-a^2)h_r^2+(2-a^2)h_r^4}{\big(ah_r^2+\sqrt{1+h_r^2(1-a^2)}\big)^2}\cos^2\alpha+\sin^2\alpha\right]\\
&= \frac{(1+a^2)}{2\big(a+\sqrt{1+h_r^2(1-a^2)}\big)^2}\cdot\\
&\cdot\left[\frac{1+(3-a^2)h_r^2+(2-a^2)h_r^4+a^2h_r^4+2ah_r^2\sqrt{1+h_r^2(1-a^2)}+1+h_r^2(1-a^2)}{\big(ah_r^2+\sqrt{1+h_r^2(1-a^2)}\big)^2}\right]\\
&= \frac{(1+a^2)}{2\big(a+\sqrt{1+h_r^2(1-a^2)}\big)^2}\left[\frac{2+2(2-a^2)h_r^2+2h_r^4+2ah_r^2\sqrt{1+h_r^2(1-a^2)}}{\big(ah_r^2+\sqrt{1+h_r^2(1-a^2)}\big)^2}\right]\\
&= \frac{(1+a^2)\Big[h_r^4+(2-a^2)h_r^2+ah_r^2\sqrt{1+h_r^2(1-a^2)}+1\Big]}{\big(a+\sqrt{1+h_r^2(1-a^2)}\big)^2\big(ah_r^2+\sqrt{1+h_r^2(1-a^2)}\big)^2}
\end{aligned}
\tag{A.2}
$$

A.3 $f(a,h_r)\to f(a,r_h)$, equation (2.38).

$$
\begin{aligned}
f(a,h_r) &= \frac{(1+a^2)\Big[1+(2-a^2)h_r^2+h_r^4+ah_r^2\sqrt{1+h_r^2(1-a^2)}\Big]}{\big(a+\sqrt{1+h_r^2(1-a^2)}\big)^2\big(ah_r^2+\sqrt{1+h_r^2(1-a^2)}\big)^2}\\
&= \frac{(1+a)^2\Big[1+(2-a^2)\frac{1}{r_h^2}+\frac{1}{r_h^4}+\frac{a}{r_h^2}\sqrt{1+h_r^2(1-a^2)}\Big]}{\Big(a+\sqrt{1+\frac{1}{r_h^2}(1-a^2)}\Big)^2\Big(\frac{a}{r_h^2}+\sqrt{1+\frac{1}{r_h^2}(1-a^2)}\Big)^2}\\
&= \frac{(1+a^2)r_h^4\big[r_h^4+(2-a^2)r_h^2+1-ar_h\sqrt{r_h^2+(1-a^2)}\big]}{\big(ar_h^2-r_h\sqrt{r_h^2+(1-a^2)}\big)^2\big(a-r_h\sqrt{r_h^2+(1-a^2)}\big)^2}
\end{aligned}
\tag{A.3}
$$

Remember that $r_h<0$, so that the square root of r_h^2 becomes $\sqrt{r_h^2}=-|r_h|$.

A.4 $LHS(h(r))\to LHS(r(h))$, equation (2.39).

Using that

$$
\begin{aligned}
h_r &= \frac{\mathrm{d}h}{\mathrm{d}r}=\frac{1}{\mathrm{d}h/\mathrm{d}r}=\frac{1}{r_h},\\
h_{rr} &= \frac{\mathrm{d}}{\mathrm{d}r}\Big(\frac{\mathrm{d}h}{\mathrm{d}r}\Big)=\frac{\mathrm{d}}{\mathrm{d}r}\Big(\frac{1}{r_h}\Big)=\frac{\mathrm{d}}{\mathrm{dh}}\frac{\mathrm{d}h}{\mathrm{d}r}\Big(\frac{1}{r_h}\Big)=\frac{\mathrm{d}}{\mathrm{d}h}\Big(\frac{1}{r_h^2}\Big)=-2\frac{r_{hh}}{r_h^3}:
\end{aligned}
\tag{A.4}
$$

$$
\begin{aligned}
LHS &= \Delta\rho g h - \frac{\sigma}{r}\frac{\mathrm{d}}{\mathrm{d}r}\Big(\frac{r h_r}{\sqrt{1+h_r^2}}\Big) \\
&= \Delta\rho g h - \frac{\sigma}{r}\left[\frac{h_r + r h_{rr}}{\sqrt{1+h_r^2}} - \frac{1}{2}\frac{2 r h_r^2 h_{rr}}{(1+h_r^2)^{\frac{3}{2}}}\right] \\
&= \Delta\rho g - \frac{\sigma}{r\sqrt{1+\frac{1}{h_r^2}}} + \sigma\frac{h_{rr}(1+h_r^2) - h_r^2 h_{rr}}{(1+h_r^2)^{\frac{3}{2}}} \\
&= \Delta\rho g - \frac{\sigma}{r\sqrt{1+\frac{1}{h_r^2}}} + \frac{\sigma h_{rr}}{(1+h_r^2)^{\frac{3}{2}}} \\
&= \Delta\rho g - \frac{\sigma}{r\sqrt{1+r_h^2}} - \frac{2\sigma r_{hh}}{(1+r_h^2)^{\frac{3}{2}}}
\end{aligned} \tag{A.5}
$$

A.5 $f(a, r_h) \to f(a, B_0, R_H)$, equation (3.3).

$$
\begin{aligned}
f(a, r_h) &= \frac{(1+a^2) r_h^4 \big[r_h^4 + (2-a^2) r_h^2 - a r_h \sqrt{r_h^2 + 1 - a^2} + 1\big]}{\big(a r_h^2 - r_h\sqrt{r_h^2+1-a^2}\big)^2 \big(a - r_h\sqrt{r_h^2+1-a^2}\big)^2} \\
&= \frac{(1+a^2) B_0^2 R_H^4 \big[B_0^2 R_H^4 + (2-a^2) B_0 R_H^2 - a\sqrt{B_0} R_H \sqrt{B_0 R_H^2 + 1 - a^2} + 1\big]}{\big(a B_0 R_H^2 - \sqrt{B_0} R_H\sqrt{B_0 R_H^2+1-a^2}\big)^2 \big(a - \sqrt{B_0} R_H\sqrt{B_0 R_H^2+1-a^2}\big)^2} \\
&= \frac{(1+a^2)\frac{1}{B_0}\left[B_0^2 R_H^4 + (2-a^2) B_0 R_H^2 - a B_0 R_H \sqrt{R_H^2 + \frac{(1-a^2)}{B_0}} + 1\right]}{\left(a R_H^2 - R_H\sqrt{R_H^2 + \frac{(1-a^2)}{B_0}}\right)^2 \left(\frac{a}{B_0} - R_H\sqrt{R_H^2 + \frac{(1-a^2)}{B_0}}\right)^2}
\end{aligned} \tag{A.6}
$$

Appendix B

Radiation force on a liquid-liquid interface curved as a sphere

The following calculations are adapted from the work of Iver Brevik during the spring, 2011. This work has not been published, and is therefore rewritten as a whole in this appendix.

Force balance

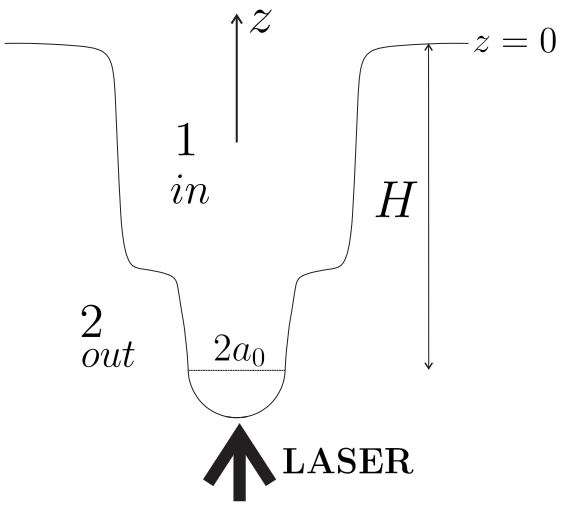

Figure B.1: Figure showing the liquid-liquid system. Medium *in* has index 1, and medium *out* has index 2. The laser beam is coming from below.

The force balance of the bottom hemisphere with radius a_0 will be investigated. The pressure force difference between the bottom side and the top of the hemisphere can be

written as

$$\gamma_2(H+d) - \gamma_1 H. \tag{B.1}$$

The subscripts 1 and 2 stands for the inner and the outer medium, respectively. Then, the resulting net force working upwards on an area dA_x of the hemisphere becomes (see figure B.2)

$$[\gamma_2(H+d) - \gamma_1 H] \cdot dA_x = (\gamma_2 - \gamma_1)H \cdot dA_x + \gamma_2 \cdot dA_x \tag{B.2}$$

Integrating this expression over the hemisphere results in

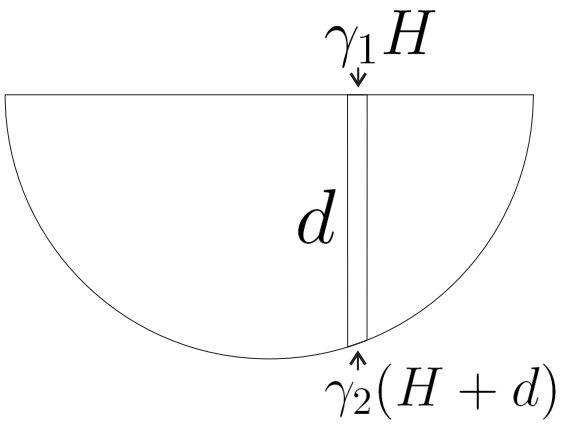

Figure B.2: Figure showing the bottom part of the liquid-liquid interface deformation. It is assumed to have the shape of a hemisphere with radius a_0.

$$(\gamma_2 - \gamma_1)H \cdot dA_x \to (\gamma_2 - \gamma_1)\pi a_0^2 H, \tag{B.3}$$

$$\gamma_2 d \cdot dA_x \to \gamma_2 V = \gamma_2 \frac{2}{3}\pi a_0^3. \tag{B.4}$$

The buoyancy force F_B can then be written as

$$F_B = (\gamma_2 - \gamma_1)\pi a_0^2 H + \gamma_2 \frac{2}{3}\pi a_0^3 \tag{B.5}$$

with upwards direction. The weight of the hemisphere (acting downwards) is

$$W = g\rho_1 \frac{2}{3}\pi a_0^3 = \gamma_1 \frac{2}{3}\pi a_0^3. \tag{B.6}$$

Next, the surface tension force, F_σ, needs to be calculated. The liquid-liquid interface is convex and hence the surface tension force is acting upwards.

$$F_\sigma = 2\pi a_0 \sigma \tag{B.7}$$

The last force in the balance is the radiation force F_{RAD}. Because $n_1 > n_2$, this force is acting downwards ($F_{RAD} < 0$). Then the force balance can be written as

$$\begin{aligned} F_B + F_\sigma &= W + |F_{RAD}| \\ (\gamma_2 - \gamma_1)\pi a_0^2 H + \gamma_2 \frac{2}{3}\pi a_0^3 + 2\pi a_0 \sigma &= \gamma_1 \frac{2}{3}\pi a_0^3 + |F_{RAD}| \\ (\gamma_2 - \gamma_1)\pi a_0^2 H + (\gamma_2 - \gamma_1)\frac{2}{3}\pi a_0^3 + 2\pi a_0 \sigma &= |F_{RAD}| \end{aligned} \tag{B.8}$$

Radiation pressure on a hemisphere

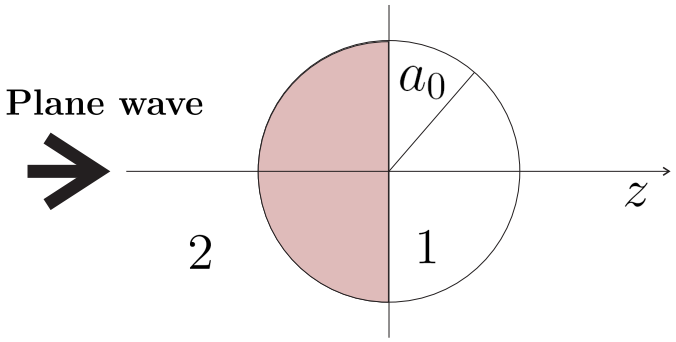

Figure B.3: A plane wave hits a hemisphere from the left. The outer medium is 2 and the inner is 1. Only the left side of the drawn sphere will be included in the calculations.

The complex representation for a circularly polarised incoming wave can be written as

$$\vec{E}^{(i)} = E_0 \vec{\Lambda} e^{i(k_z z - \omega t)}, \quad \vec{\Lambda} = \vec{e_x} + i\vec{e_y}, \tag{B.9}$$

where the superscript (i) denotes the incoming wave. The real field components $\mathcal{E}_x$ and $\mathcal{E}_y$ are:

$$\mathcal{E}_x^{(i)} = \Re(E_x^{(i)}) = E_0 \cos(k_z z - \omega t) \tag{B.10}$$

$$\mathcal{E}_y^{(i)} = \Re(E_y^{(i)}) = E_0 \cos(k_z z - \omega t + \frac{\pi}{2}) = -E_0 \sin(k_z z - \omega t) \tag{B.11}$$

Assuming a non-magnetic medium: $\vec{D} = \epsilon_0 \epsilon_r \vec{E} = \epsilon_0 n^2 \vec{E}$ and $\vec{B} = \mu_0 \vec{H}$. The energy density in the incoming electromagnetic field is:

$$\begin{aligned} w &= \frac{1}{2}\epsilon_0 n^2 \langle \vec{\mathcal{E}}^2 \rangle + \frac{1}{2}\mu_0 \langle \vec{\mathcal{H}}^2 \rangle = \epsilon_0 n^2 \langle \vec{\mathcal{E}}^2 \rangle \\ &= \frac{1}{2}\epsilon_0 n^2 \Re(\vec{E}\vec{E}^*) = \frac{1}{2}\epsilon_0 n^2 E_0^2 \end{aligned} \tag{B.12}$$

The intensity, I, can be written as

$$I = w \cdot \frac{c}{n_2} = \frac{1}{2}\epsilon c n_2 E_0^2 = \epsilon_0 c n_2 \langle \mathcal{E}^2 \rangle. \tag{B.13}$$

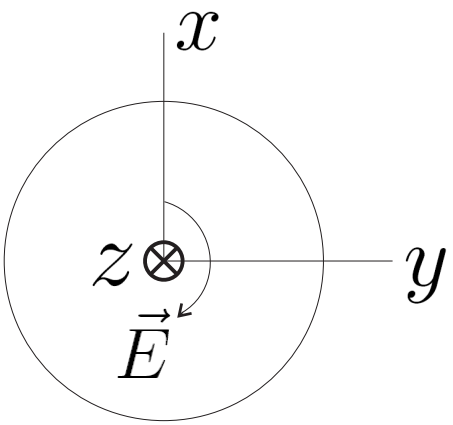

Figure B.4: The hemisphere seen from below. The electric field is assumed to be circularly polarised.

General representation of the incoming electromagnetic field

The general representation of the incoming electromagnetic field in spherical coordinates is [26]

$$E_r^{(i)} = \frac{E_0}{\tilde{r}^2}\sum_{l=1}^{\infty}\sum_{m=-l}^{l} l(l+1)A_{lm}\psi_l(\alpha\tilde{r})Y_{lm} \tag{B.14}$$

$$E_\theta^{(i)} = \frac{\alpha E_0}{\tilde{r}}\sum_{l=1}^{\infty}\sum_{m=-l}^{l}\Big[A_{lm}\psi_l'(\alpha\tilde{r})\frac{\partial Y_{lm}}{\partial\theta} - \frac{m}{n_2}B_{lm}\psi_l(\alpha\tilde{r})\frac{Y_{lm}}{\sin\theta}\Big] \tag{B.15}$$

$$E_\phi^{(i)} = \frac{\alpha E_0}{\tilde{r}}\sum_{l=1}^{\infty}\sum_{m=-l}^{l}\Big[imA_{lm}\psi_l'(\alpha\tilde{r})\frac{Y_{lm}}{\sin\theta} - \frac{i}{n_2}B_{lm}\psi_l(\alpha\tilde{r})\frac{\partial Y_{lm}}{\partial\theta}\Big] \tag{B.16}$$

Here, $\alpha = k_2 a_0 = n_2\frac{\omega}{c}a_0 = \frac{2\pi}{\lambda}$, λ being the wavelength in medium 2. Also, $\tilde{r} = \frac{r}{a_0}$. Introducing two new constants n_{12} and n_{21} as the relative refractive index:

$$n_{12} = \frac{n_1}{n_2} = \frac{n_{in}}{n_{out}} > 1, \quad n_{21} = \frac{n_2}{n_1} = \frac{n_{out}}{n_{in}} < 1. \tag{B.17}$$

With these expressions, the internal electric field components can be written as

$$E_r^{(w)} = \frac{E_0}{\tilde{r}^2}\sum_{l=1}^{\infty}\sum_{m=-l}^{l} l(l+1)c_{lm}\psi_l(n_{12}\alpha\tilde{r})Y_{lm} \tag{B.18}$$

$$E_\theta^{(w)} = \frac{\alpha E_0}{\tilde{r}}\sum_{l=1}^{\infty}\sum_{m=-l}^{l}\Big[n_{12}c_{lm}\psi_l'(n_{12}\alpha\tilde{r})\frac{\partial Y_{lm}}{\partial\theta} - \frac{m}{n_2}d_{lm}\psi_l(n_{12}\alpha\tilde{r})\frac{Y_{lm}}{\sin\theta}\Big] \tag{B.19}$$

$$E_\phi^{(w)} = \frac{\alpha E_0}{\tilde{r}}\sum_{l=1}^{\infty}\sum_{m=-1}^{l}\Big[imn_{12}c_{lm}\psi_l'(n_{12}\alpha\tilde{r})\frac{Y_{lm}}{\sin\theta} - \frac{i}{n_2}d_{lm}\psi_l(n_{12}\alpha\tilde{r})\frac{\partial Y_{lm}}{\partial\theta}\Big] \tag{B.20}$$

The Riccati-Bessel functions are given by:

$$\psi_l(x) = xj_l(x), \quad \xi_l^{(1)}(x) = xh_l^{(1)}(x). \tag{B.21}$$

For the special case of $l = 1$, the Riccati-Bessel functions can be written as:

$$\psi_1(x) = xj_1(x) = \frac{\sin x}{x} - \cos x \tag{B.22}$$

$$\chi_1(x) = -xn_1(x) = \frac{\cos x}{x} + \sin x \tag{B.23}$$

$$\xi_1^{(1)}(x) = \psi_1 - i\chi_1 = -\big(1 + \frac{i}{x}\big)e^{ix}. \tag{B.24}$$

Taking the Wronskian:

$$W\{\psi_l, \xi_l^{(1)}\} = \psi_l \xi_l'^{(1)} - \psi_l' \xi_l^{(1)} = i \tag{B.25}$$

All Riccati- Bessel functions w satisfies [20] (page 445):

$$x^2 w'' + [x^2 - l(l+1)]w = 0, \ l = 0, \pm 1, \pm 2, ... \tag{B.26}$$

General expressions for the magnetic field components for a incoming wave can be written as:

$$H_r^{(i)} = \frac{H_0}{\tilde{r}^2} \sum_{l=1}^{\infty} \sum_{m=-l}^{l} l(l+1) B_{lm} \psi_l(\alpha\tilde{r}) Y_{lm} \tag{B.27}$$

$$H_\theta^{(i)} = \frac{\alpha H_0}{\tilde{r}} \sum_{l=1}^{\infty} \sum_{m=-l}^{l} \Big[B_{lm} \psi_l'(\alpha\tilde{r}) \frac{\partial Y_{lm}}{\partial \theta} + m n_2 A_{lm} \psi_l(\alpha\tilde{r}) \frac{Y_{lm}}{\sin\theta} \Big] \tag{B.28}$$

$$H_\phi^{(i)} = \frac{\alpha H_0}{\tilde{r}} \sum_{l=1}^{\infty} \sum_{m=-l}^{l} \Big[im B_{lm} \psi_l'(\alpha\tilde{r}) \frac{Y_{lm}}{\sin\theta} + i n_2 A_{lm} \psi_l(\alpha\tilde{r}) \frac{\partial Y_{lm}}{\partial \theta} \Big]. \tag{B.29}$$

The corresponding components of the inner field are:

$$H_r^{(w)} = \frac{H_0}{\tilde{r}^2} \sum_{l=1}^{\infty} \sum_{m=-l}^{l} l(l+1) d_{lm} \psi_l(n_{12}\alpha\tilde{r}) Y_{lm} \tag{B.30}$$

$$H_\theta^{(w)} = \frac{\alpha H_0}{\tilde{r}} \sum_{l=1}^{\infty} \sum_{m=-l}^{l} \Big[n_{12} d_{lm} \psi_l'(n_{12}\alpha\tilde{r}) \frac{\partial Y_{lm}}{\partial \theta} + m n_2 n_{12}^2 c_{lm} \psi_l(n_{12}\alpha\tilde{r}) \frac{Y_{lm}}{\sin\theta} \Big] \tag{B.31}$$

$$H_\phi^{(w)} = \frac{\alpha H_0}{\tilde{r}} \sum_{l=1}^{\infty} \sum_{m=-l}^{l} \Big[im n_{12} d_{lm} \psi_l'(n_{12}\alpha\tilde{r}) \frac{Y_{lm}}{\sin\theta} + i n_2 n_{12}^2 c_{lm} \psi_l(n_{12}\alpha\tilde{r}) \frac{\partial Y_{lm}}{\partial \theta} \Big], \tag{B.32}$$

where $\alpha = n_2 \frac{\omega a}{c}$, $n_{12} = \frac{n_1}{n_2}$ and $H_0 = \sqrt{\frac{\epsilon_0}{\mu_0}} E_0$. When $E_r^{(i)}$ and $H_r^{(i)}$ are known, the coefficients A_{lm} and B_{lm} can be found by [27]

$$A_{lm} = \frac{1}{E_0 l(l+1)\psi_l(\alpha)} \int_{sphere} E_r^{(i)}(a, \theta, \phi) Y_{lm}^*(\theta, \phi) \, \mathrm{d}\Omega \tag{B.33}$$

$$B_{lm} = \frac{1}{H_0 l(l+1)\psi_l(\alpha)} \int_{sphere} H_r^{(i)}(a,\theta,\phi) Y_{lm}^*(\theta,\phi)\, \mathrm{d}\Omega \tag{B.34}$$

In order to find F_{RAD}, also the coefficients $\{c_{lm}, d_{lm}\}$ need to be determined. These coefficients can be found by using the electromagnetic boundary conditions at $r = a_0$. [26]

$$c_{lm} = \frac{i}{n_{12}^2 \psi_l(n_{12}\alpha)\xi_l^{(1)'}(\alpha) - n_{12}\psi_l'(n_{12}\alpha)\xi_l^{(1)}(\alpha)} \cdot A_{lm} \tag{B.35}$$

$$d_{lm} = \frac{i}{\psi_l(n_{12}\alpha)\xi_l^{(1)'}(\alpha) - n_{12}\psi_l'(n_{12}\alpha)\xi_l^{(1)}(\alpha)} \cdot B_{lm} \tag{B.36}$$

Circularly polarised plane wave

The incoming electric and magnetic field of a circularly polarised plane wave can be written as:

$$\vec{E}^{(i)} = E_0(\vec{e_x} + i\vec{e_y})e^{ik_z z - i\omega t} \tag{B.37}$$

and

$$\vec{H}^{(i)} = \frac{n_2 E_0}{c\mu_0}(\vec{e_x} + i\vec{e_y})e^{ik_z z - i\omega t}. \tag{B.38}$$

A useful relation from Jackson (1975, page 771) [28] is that:

$$\nabla \times j_l(kr)\vec{X}_{lm} = \frac{i\vec{n}\sqrt{l(l+1)}}{r} j_l(kr) Y_{lm} + \frac{1}{r}\frac{\partial}{\partial r}\big[r j_l(kr)\big]\vec{n} \times \vec{X}_{lm}, \tag{B.39}$$

where $\vec{n} = \hat{r}$. In the hemisphere, there will only be contributions from $m = +1$ (positive helicity of the polarisation). Then,

$$E_0\vec{\Lambda}e^{ik_z z} = E_0 \sum_{l=1}^{\infty} i^l \sqrt{4\pi(2l+1)}\Big[j_l(kr)\vec{X}_{l1} + \frac{1}{k}\nabla \times j_l(kr)\vec{X}_{l1}\Big]. \tag{B.40}$$

Here, $\vec{X}_{lm}(\theta,\phi)$ denotes the spherical harmonics:

$$\begin{aligned}
\vec{X}_{lm} &= \frac{\vec{L}Y_{lm}}{l(l+1)}, \quad \vec{L} = \frac{1}{i}\vec{r} \times \nabla, \quad L^2 Y_{lm} = l(l+1)Y_{lm} \\
\nabla^2 Y_{lm} &= -\frac{L^2}{r^2}Y_{lm} = -\frac{l(l+1)}{r^2}Y_{lm} \\
\sum_{m=-l}^{l} |\vec{X}_{lm}|^2 &= \frac{2l+1}{4\pi} = \sum_{m=-l}^{l} |Y_{lm}|^2.
\end{aligned} \tag{B.41}$$

Some useful relations are:

$$\begin{aligned}
\hat{r}\vec{e_x} &= \sin\theta\cos\phi, & \hat{r}\vec{e_y} &= \sin\theta\sin\phi, & \hat{r}\vec{e_z} &= \cos\theta \\
\hat{\theta}\vec{e_x} &= \cos\theta\cos\theta, & \hat{\theta}\vec{e_y} &= \cos\theta\sin\phi, & \hat{\theta}\vec{e_z} &= -\sin\theta \\
\hat{\phi}\vec{e_x} &= -\sin\phi, & \hat{\phi}\vec{e_y} &= \cos\phi, & \hat{\phi}\vec{e_z} &= 0.
\end{aligned} \tag{B.42}$$

From the vector $\vec{\Lambda} = \vec{e_x} + i\vec{e_y}$ and the expressions in (B.42), it follows that

$$\Lambda_r = \vec{e_x}\hat{r} + i\vec{e_y}\hat{r} = \sin\theta e^{i\phi} \tag{B.43}$$

$$\Lambda_\theta = \vec{e_x}\hat{\theta} + i\vec{e_y}\hat{\theta} = \cos\theta\cos\phi + i\cos\theta\sin\phi = \cos\theta e^{i\phi} \tag{B.44}$$

$$\Lambda_\phi = \vec{e_x}\hat{\phi} + i\vec{e_y}\hat{\theta} = -\sin\phi + i\cos\phi = ie^{i\phi}. \tag{B.45}$$

One needs the expression for e^{ikz}:

$$e^{i\vec{k}\vec{r}} = e^{ikz} = \sum_{l=0}^{\infty} i^l(2l+1)j_l(kr)Y_{l0}(\theta) = \sum_{l=0}^{\infty} i^l\sqrt{4\pi(2l+1)}j_l(kr)Y_{l0}(\theta), \tag{B.46}$$

where

$$Y_{l0}(\theta,\phi) = Y_{l0} = \sqrt{\frac{2l+1}{4\pi}}P_l(cos\theta), \tag{B.47}$$

$$Y_{l1}(\theta,\phi) = \sqrt{\frac{2l+1}{4\pi}\frac{(l-1)!}{(l+1)!}}P_l^1(\cos\theta)e^{i\phi} = \sqrt{\frac{2l+1}{4\pi(l+1)l}}P_l^1(\cos\theta)e^{i\phi}. \tag{B.48}$$

Taking the r-component from equation (B.40):

$$E_0\Lambda_r e^{ikz} = E_0\sum_{l=1}^{\infty} i^l\sqrt{4\pi(2l+1)}\frac{1}{k}\frac{i}{r}\sqrt{l(l+1)}j_l(kr)Y_{l1}(\Omega)$$

$$\sin\theta e^{i\phi}\sum_{l=0}^{\infty} i^l\sqrt{4\pi(2l+1)}j_l(kr)Y_{l0}(\theta) = \sum_{l=1}^{\infty}\frac{i^{l+1}}{kr}\sqrt{4\pi(2l+1)(l(l+1)}j_l(kr)\sqrt{\frac{2l+1}{4\pi(l+1)l}}P_l^1(\cos\theta)e^{i\phi}$$

$$\sin\theta\sum_{l=1}^{\infty} i^l\sqrt{4\pi(2l+1)}j_l(kr)Y_{l0}(\theta) = \frac{1}{kr}\sum_{l=1}^{\infty} i^{l+1}(2l+1)j_l(kr)P_l^1(\cos\theta)$$

$$\sin\theta\sum_{l=0}^{\infty} i^l(2l+1)j_l(kr)P_l(\cos\theta) = \frac{1}{kr}\sum_{l=1}^{\infty} i^{l+1}(2l+1)j_l(kr)P_l^1(\cos\theta). \tag{B.49}$$

The electric field of a circularly polarised incoming beam

From Jackson (1999, page 472, [29]), the incoming electric field when assuming circularly polarisation can be written as:

$$\vec{E}^{(i)} = E_0\sum_{l=1}^{\infty}\left[a_+ j_l(kr)\vec{X}_{lm} + \frac{i}{k}b_+\nabla\times j_l kr\vec{X}_{lm}\right]$$

$$\vec{X}_{lm}(\Omega) = \frac{\vec{L}Y_{lm}(\Omega)}{\sqrt{l(l+1)}},\quad \vec{L} = \frac{1}{i}\vec{r}\times\nabla,\quad L^2Y_{lm} = l(l+1)Y_{lm}$$

$$\sum_{m=-l}^{l}|\vec{X}_{lm}(\Omega)|^2 = \frac{2l+1}{4\pi} = \sum_{m=-l}^{l}|Y_{lm}|^2 \tag{B.50}$$

When the helicity $m = +1$ (and circular polarisation) [29],

$$a_+ = i^l\sqrt{4\pi(2l+1)}, \quad b_+ = -ia_+, \tag{B.51}$$

so that

$$\vec{E}^{(i)} = E_0\sum_{l=1}^{\infty} i^l\sqrt{4\pi(2l+1)}\Big[j_l(kr)\vec{X}_{l1}(\Omega) + \frac{1}{k}\nabla\times j_l(kr)\vec{X}_{l1}(\Omega)\Big]. \tag{B.52}$$

Because $[\nabla\times j_l(kr)\vec{X}_{lm}]_r = \frac{i}{r}\sqrt{l(l+1)}j_l krY_{lm}$ (equation (B.39)), the radial component of the incoming electric field becomes:

$$E_r^{(i)} = E_0\sum_{l=1}^{\infty} i^{l+1}\sqrt{4\pi(2l+1)l(l+1)}\frac{j_l(kr)}{kr}Y_{l1}. \tag{B.53}$$

With $\psi_l(kr) = krj_l(kr)$, equation (B.53) becomes:

$$E_r^{(i)} = \frac{E_0}{(kr)^2}\sum_{l=1}^{\infty} i^{l+1}\sqrt{4\pi(2l+1)l(l+1)}\psi_l(kr)Y_{l1} \tag{B.54}$$

From the general form

$$Y_{lm} = \sqrt{\frac{2l+1}{4\pi}\frac{(l-m)!}{(l+m)!}}P_l^m(\cos\theta)e^{im\phi}, \tag{B.55}$$

follows that

$$Y_{l1} = \sqrt{\frac{2l+1}{4\pi}\frac{1}{l(l+1)}}P_l^1(\cos\theta)e^{i\phi}, \tag{B.56}$$

where $P_l^m(\cos\theta)$ is the associated Legendre function. Inserting the expression for Y_{l1} into equation (B.54) results in

$$E_r^{(i)} = \frac{E_0e^{i\phi}}{(kr)^2}\sum_{l=1}^{\infty} i^{l+1}(2l+1)\psi_l(kr)P_l^1(\cos\theta) \tag{B.57}$$

for cases of circular polarisation. Comparing equation (B.14) and equation (B.54), with $m = +1$ gives

$$E_0\sum_{l=1}^{\infty} l(l+1)A_{l1}\psi_l(kr)Y_{l1} = E_0\sum_{l=1}^{\infty} i^{l+1}\sqrt{4\pi(2l+1)l(l+1)}\psi_l(kr)Y_{l1}, \tag{B.58}$$

where

$$A_{l1} = \frac{i^{l+1}}{\alpha^2}\sqrt{\frac{4\pi(2l+1)}{l(l+1)}}, \quad l = 1,2,3,... \quad B_{l1} = \frac{A_{l1}}{i}. \tag{B.59}$$

The magnetic field of a circularly polarised incoming beam

The magnetic field (circular polarisation) of an incoming wave can be written as (Jackson, [29])

$$\vec{H}^{(i)} = H_0 \sum_{l=1}^{\infty} \Big[-\frac{i}{k} a_+ \nabla \times j_l(kr)\vec{X}_{l1} + b_+ j_l(kr)\vec{X}_{l1} \Big], \tag{B.60}$$

where $H_0 = \sqrt{\frac{\epsilon_0}{\mu_0}} E_0$.

$$\vec{H}^{(i)} = -H_0 \sum_{l=1}^{\infty} i^{l+1}\sqrt{4\pi(2l+1)} \Big[\frac{1}{k} \nabla \times j_l(kr)\vec{X}_{l1} + j_l(kr)\vec{X}_{l1} \Big]. \tag{B.61}$$

The radial component of the magnetic field becomes

$$\begin{aligned} H_r^{(i)} &= -H_0 \sum_{l=1}^{\infty} i^{l+1}\sqrt{4\pi(2l+1)} \frac{i}{kr} \sqrt{l(l+1)} j_l(kr) Y_{l1}(\Omega) \\ &= \sum_{l=1}^{\infty} i^l \sqrt{4\pi(2l+1)l(l+1)} \frac{j_l(kr)}{kr} Y_{l1}(\Omega) \\ &= \frac{H_0}{(kr)^2} \sum_{l=1}^{\infty} i^l \sqrt{4\pi(2l+1)l(l+1)} \psi_l(kr) Y_{l1}(\Omega). \end{aligned} \tag{B.62}$$

Again, by inserting $Y_{l1} = \sqrt{\frac{2l+1}{4\pi} \frac{1}{l(l+1)}} P_l^1(\cos\theta) e^{i\phi}$ the following expression is achieved:

$$H_r^{(i)} = \frac{H_0 e^{i\phi}}{(kr)^2} \sum_{l=1}^{\infty} i^l (2l+1) \psi_l(kr) P_l^1(\cos\theta). \tag{B.63}$$

Comparing this expression to the earlier one from equation (B.27):

$$\frac{H_0}{\alpha} \sum_{l=1}^{\infty} i^l \sqrt{4\pi(2l+1)l(l+1)} \psi_l(kr) Y_{lm}(\Omega) = H_0 \sum_{l=1}^{\infty} l(l+1) B_{lm} \psi_l(\alpha\tilde{r}) Y_{lm}(\Omega). \tag{B.64}$$

Hence, the coefficients B_{l1} and A_{l1} must be

$$B_{l1} = \frac{i^l}{\alpha^2} \sqrt{\frac{4\pi(2l+1)}{l(l+1)}}, \;\; l = 1, 2, 3, ..., \quad A_{l1} = iB_{l1}l. \tag{B.65}$$

Radiation force on the sphere

The surface force density σ^{AM} at $r = a_0$ can be found by integrating the radial force density across the surface from right outside the hemisphere, a_{0-}, to the inside at a_{0+}:

$$\sigma^{AM} = -\frac{1}{2}\epsilon \int_{a_{0-}}^{a_{0+}} E^2 \frac{\mathrm{d}\epsilon_\mathrm{r}}{\mathrm{d}r}\,\mathrm{d}r = -\frac{1}{2}\epsilon_0 \int_{a_{0-}}^{a_{0+}} \left[E_t^2 + E_r^2\right] \frac{\mathrm{d}\epsilon_\mathrm{r}}{\mathrm{d}r}\,\mathrm{d}r. \tag{B.66}$$

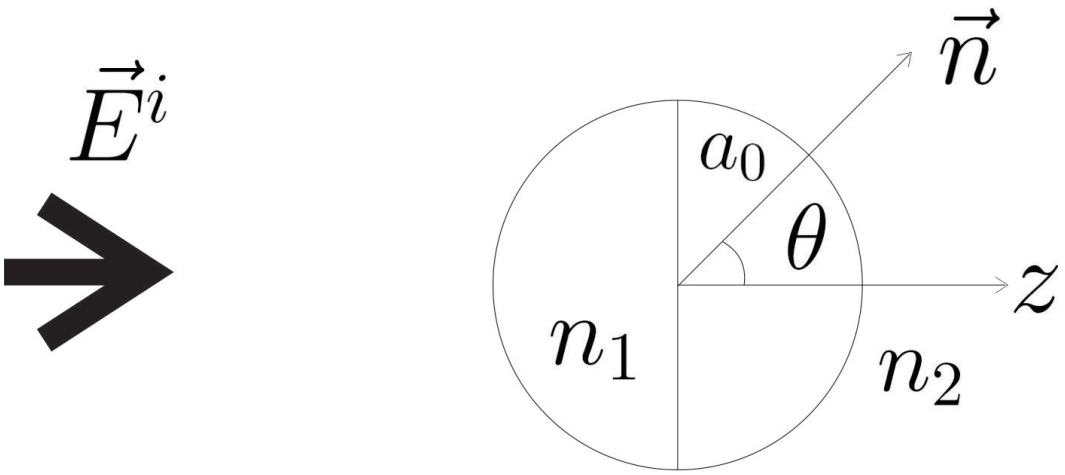

Figure B.5: Figure showing the incoming electric field and the hemisphere with radius a_0.

Both E_t and $D_r = \epsilon E_r$ are continuous:

$$\begin{aligned}\sigma^{AM} &= -\frac{1}{2}\epsilon_0 E_t^2(\epsilon_2 - \epsilon_1) - \frac{1}{2\epsilon_0}\int_{a_{0-}}^{a_{0+}} \frac{D_r^2}{\epsilon_r^2}\frac{\mathrm{d}\epsilon_\mathrm{r}}{\mathrm{dr}}\,\mathrm{dr} \\ &= -\frac{1}{2}\epsilon_0 E_t^2(\epsilon_2 - \epsilon_1) + \frac{1}{2\epsilon_0} D_r^2\big(\frac{1}{\epsilon_2} - \frac{1}{\epsilon_1}\big) \\ &= -\frac{1}{2}\epsilon_0 n_2^2 E_t^2(1 - n_{12}^2) + \frac{1}{2\epsilon_0} n_1^2 E_r^2(a_{0-})\big(\frac{\epsilon_1}{\epsilon_2} - 1\big). \end{aligned} \tag{B.67}$$

Here, E_t and E_r are real fields components. Then,

$$\sigma^{AM} = \frac{1}{2}\epsilon_0 n_2^2(n_{12}^2 - 1)(E_t^2 + n_{12}^2 E_r^2)|_{a_{0-}}. \tag{B.68}$$

The radiation force is pointing utwards when $n_1 > n_2$. The radial force on an area $\mathrm{d}A = a_0^2 \sin\theta \mathrm{d}\theta \mathrm{d}\phi$ is $\sigma^{AM}\mathrm{dA}$. The total radiation force on the hemisphere is then ($F_{RAD} < 0$)

$$F_{RAD} = a_0^2 \int_0^{2\pi} \mathrm{d}\phi \int_{\frac{\pi}{2}}^{\pi} \sigma^{AM}|_{a_{0-}} \cos\theta \sin\theta \,\mathrm{d}\theta \tag{B.69}$$

The internal electric field components at $r = a_{0-}$ are (from (B.18))

$$E_r^{(w)} = E_0 \sum_{l=1}^{\infty} l(l+1) c_{l1} \psi_l(n_{12}\alpha) Y_{l1}, \quad Y_{l1} = \sqrt{\frac{2l+1}{4\pi} \frac{1}{l(l+1)}} P_l^1(\cos\theta) e^{i\phi},$$
$$E_\theta^{(w)} = \alpha E_0 \sum_{l=1}^{\infty} \Big[n_{12} c_{l1} \psi_l'(n_{12}\alpha) \frac{\partial Y_{l1}}{\partial \theta} - \frac{1}{n_2} d_{l1} \psi_l(n_{12}\alpha) \frac{Y_{l1}}{\sin\theta} \Big],$$
$$E_\phi^{(w)} = \alpha E_0 \sum_{l=1}^{\infty} \Big[i n_{12} c_{l1} \psi_l'(n_{12}\alpha) \frac{Y_{l1}}{\sin\theta} - \frac{i}{n_2} d_{l1} \psi_l(n_{12}\alpha) \frac{\partial Y_{l1}}{\partial \theta} \Big], \tag{B.70}$$

where

$$c_{l1} = \frac{i}{n_{12}^2 \psi_l(n_{12}\alpha) \xi_l^{(1)'}(\alpha) - n_{12} \psi_l'(n_{12}\alpha) \xi_l^{(1)}(\alpha)} A_{l1}, \quad A_{l1} = \frac{i^{l+1}}{\alpha^2} \sqrt{\frac{4\pi(2l+1)}{l(l+1)}}, \tag{B.71}$$

$$d_{l1} = \frac{i}{\psi_l(n_{12}\alpha) \xi_l^{(1)'}(\alpha) - n_{12} \psi_l'(n_{12}\alpha) \xi_l^{(1)}(\alpha)} B_{l1}, \qquad B_{l1} = \frac{i^l}{\alpha^2} \sqrt{\frac{4\pi(2l+1)}{l(l+1)}}. \tag{B.72}$$

The function $\psi_l(x) = x j_l(x)$ is real and $\xi_l^{(i)}(x) = x h_l^{(1)}(x)$ is complex, where $h_l^{(1)}(x) = j_l(x) + i n_l(x)$ is the spherical Hankel function ($n_l(x)$ is the spherical Neumann function). With a physical electric field $\vec{\mathcal{E}}$, then

$$\sigma^{AM} = \frac{1}{2} \epsilon_0 n_2^2 (n_{12}^2 - 1) [\mathcal{E}_t^2 + n_{12}^2 \mathcal{E}_r^2], \tag{B.73}$$

where $\mathcal{E}_t^2 = \mathcal{E}_\theta^2 + \mathcal{E}_\phi^2$. Taking the contribution from $\mathcal{E}_r^2$ results in:

$$a_0^2 \int_{FRONT} \mathcal{E}_r^2 \cos\theta \, \mathrm{d}\Omega = \frac{a_0^2}{2} \int_{FRONT} |E_r|^2 \cos\theta \, \mathrm{d}\Omega$$
$$= \frac{a_0^2}{2} E_0^2 \sum_{l,l'=1}^{\infty} l(l+1) l'(l'+1) c_{l1} c_{l'1}^* \psi_l(n_{12}\alpha) \psi_l'(n_{12}\alpha) \int_{FRONT} Y_{l1}(\Omega) Y_{l'1}^*(\Omega) \cos\theta \, \mathrm{d}\Omega, \tag{B.74}$$

where the integral from equation (B.74) is:

$$\int_{FRONT} Y_{l1}(\Omega) Y_{l'1}^*(\Omega) \cos\theta \, \mathrm{d}\Omega = \int_0^{2\pi} \sin\theta \cos\theta \mathrm{Y}_{\mathrm{l1}}(\Omega) \mathrm{Y}_{\mathrm{l'1}}^*(\Omega) \, \mathrm{d}\theta. \tag{B.75}$$

Inserting that $Y_{l1}(\Omega) = \sqrt{\frac{2l+1}{4\pi(l+1)l}} P_l^1(\cos\theta) e^{i\phi}$ results in:

$$\int_F Y_{l1}(\Omega) Y_{l'1}^*(\Omega) \cos\theta \, \mathrm{d}\Omega = 2\pi \sqrt{\frac{2l+1}{4\pi(l+1)l}} \sqrt{\frac{2l'+1}{4\pi(l'+1)l'}} \int_{\frac{\pi}{2}}^{\pi} \sin\theta \cos\theta P_l^1(\cos\theta) P_{l'}^1(\cos\theta) \, \mathrm{d}\theta, \tag{B.76}$$

where integral in equation (B.76) can be written as:

$$\int_{\frac{\pi}{2}}^{\pi} \sin\theta\cos\theta P_l^1(\cos\theta)P_{l'}^1(\cos\theta)\,\mathrm{d}\theta = -\int_0^{-1} xP_l^1(x)P_{l'}^1(x) = -\int_0^1 xP_l^1(-x)P_{l'}^1(-x)\,\mathrm{d}\theta \tag{B.77}$$

Since $P_l(-x) = (-1)^l P_l^1(x)$, and $P_l^1(x) = -\sqrt{1-x^2}\frac{\mathrm{d}}{\mathrm{d}x}P_l^1(x)$ [29],

$$P_l^1(-x) = (-1)^{l-1}P_l^1(x). \tag{B.78}$$

As usual (for spheres), there will only be contributions from the case when $l' = l$. Then,

$$\int_{\frac{\pi}{2}}^{\pi} \sin\theta\cos\theta[P_l^1(\cos\theta)]^2\,\mathrm{d}\theta = -\int_0^1 x[P_l^1(\cos\theta)]^2\,\mathrm{d}x < 0. \tag{B.79}$$

The contribution on this side of the sphere has same, but different direction, to the other hemisphere:

$$\int_0^{\frac{\pi}{2}} \sin\theta\cos\theta[P_l^1(\cos\theta)]^2\,\mathrm{d}\theta = +\int_0^1 x[P_l^1(x)]^2\,\mathrm{d}x > 0. \tag{B.80}$$

From the front side of the sphere:

$$\begin{aligned}\int_{FRONT} Y_{l1}(\Omega)Y_{l1}^*(\Omega) &= 2\pi\frac{2l+1}{4\pi(l+1)l}\Big[-\int_0^1 x[P_l^1(x)]^2\,\mathrm{d}x\Big] \\ &= -\frac{2l+1}{2(l+1)l}\int_0^1 x[P_l^1(x)]^2\,\mathrm{d}x,\end{aligned} \tag{B.81}$$

which then gives

$$\begin{aligned}\int_{FRONT}\mathcal{E}_r^2\cos\theta\,\mathrm{d}\Omega &= \frac{a_0^2}{2}E_0^2\sum_{l=1}^{\infty}[l(l+1)]^2|c_{l1}|^2\psi_l^2(n_{12}\alpha)\Big[-\frac{2l+1}{2(l+1)l}\Big]\int_0^1 x[P_l^1(x)]^2\,\mathrm{d}x \\ &= -\frac{a_0^2}{4}E_0^2\sum_{l=1}^{\infty}\big[l(l+1)(2l+1)\big]|c_{l1}|^2\psi_l^2(n_{12}\alpha)\int_0^1 x[P_l^1(x)]^2\,\mathrm{d}x.\end{aligned} \tag{B.82}$$

Then, it is time for the contribution from $E_t^2 = E_\theta^2 + E_\phi^2$. The integral $\int_{FRONT}\mathcal{E}_t^2\cos\theta\,\mathrm{d}\Omega$ needs to be calculated.

$$\begin{aligned}\int_{FRONT}\mathcal{E}_\theta^2\cos\theta\,\mathrm{d}\Omega &= \frac{a^2}{2}\int_{FRONT}|E_\theta|^2\,\mathrm{d}\Omega \\ &= \frac{a^2}{2}\alpha^2E_0^2\sum_{l=1}^{\infty}\int_{FRONT}\Big[n_{12}c_{l1}\psi_l'(n_{12}\alpha)\frac{\partial Y_{l1}^*}{\partial\theta} - \frac{1}{n_{12}}d_{l1}^*\psi_l(n_{12}\alpha)\frac{Y_{l1}}{\sin\theta}\Big]\cdot \\ &\cdot\Big[n_{12}c_{l1}^*\psi_l'(n_{12}\alpha)\frac{\partial Y_{l1}^*}{\partial\theta} - \frac{1}{n_2}d_{l1}^*\psi_l(n_{12}\alpha)\frac{Y_{l1}}{\sin\theta}\Big]\cos\theta\,\mathrm{d}\Omega\end{aligned} \tag{B.83}$$

The expression for $Y_{l1} = \sqrt{\frac{2l+1}{4\pi l(l+1)}} P_l^1 e^{i\phi}$ gives

$$\Big|\frac{\partial Y_{l1}}{\partial \theta}\Big|^2 = \frac{2l+1}{4\pi l(l+1)}\Big(\frac{\mathrm{d}P_l^1}{\mathrm{d}\theta}\Big)^2, \tag{B.84}$$

$$|Y_{l1}|^2 = \frac{2l+1}{4\pi l(l+1)}[P_l^1]^2. \tag{B.85}$$

Then, the integral from equation (B.83) can be reformulated as:

$$\begin{aligned} &a_0^2 \int_{FRONT} \mathcal{E}_\theta^2 \cos\theta \,\mathrm{d}\Omega \\ &= \frac{a_0}{2}\alpha^2 E_0^2 \sum_{l=1}^{\infty} \int_{FRONT} \frac{2l+1}{4\pi l(l+1)} \Big\{ n_{12}^2 |c_{l1}|^2 (\psi_l')^2 \Big[\frac{\mathrm{d}P_l^1}{\mathrm{d}\theta}\Big]^2 + \frac{1}{n_2^2}|d_{l1}|^2 \psi_l^2 \frac{[P_l^1]^2}{\sin^2\theta}\Big\} \cos\theta \,\mathrm{d}\Omega \end{aligned} \tag{B.86}$$

Next, the integral for $\mathcal{E}_\phi$ needs to be investigated (only including $l' = l$):

$$\begin{aligned} &\int_{FRONT} \mathcal{E}_\phi^2 \cos\theta \,\mathrm{d}\Omega = \frac{a_0^2}{2} \int_{FRONT} |E_\phi|^2 \cos\theta \,\mathrm{d}\Omega = \\ &= \frac{a_0^2}{2}\alpha^2 E_0^2 \sum_{l=1}^{\infty} \int_{FRONT} \Big[i n_{12} c_{l1} \psi_l'(n_{12}\alpha) \frac{Y_{l1}^*}{\sin\theta} + \frac{i}{n_2} d_{l1}^* \psi_l(n_{12}\alpha) \frac{\partial Y_{l1}^*}{\partial \theta}\Big] \cdot \\ &\cdot \Big[- i n_{12} c_{l1}^* \psi_l'(n_{12}\alpha) \frac{Y_{l1}^*}{\sin\theta} - \frac{i}{n_2} d_{l1}^* \psi_l(n_{12}\alpha) \frac{\partial Y_{l1}^*}{\partial \theta}\Big] \cos\theta \,\mathrm{d}\Omega \\ &= \frac{a_0^2}{2}\alpha^2 E_0^2 \sum_{l=1}^{\infty} \int_{FRONT} \Big\{ n_{12}^2 |c_{l1}|^2 [\psi_{l1}']^2 \frac{|Y_{l1}|^2}{\sin^2\theta} + \frac{1}{n_2^2}|d_{l1}|^2 \psi_l^2 \Big|\frac{\partial Y_{l1}}{\partial \theta}\Big|^2 \Big\} \cos\theta \,\mathrm{d}\Omega \\ &= \frac{a_0^2}{2}\alpha^2 E_0^2 \sum_{l=1}^{\infty} \int_{FRONT} \frac{2l+1}{4\pi l(l+1)} \Big\{ n_{12}^2 |c_{l1}|^2 (\psi_l')^2 \frac{[P_l^1]^2}{\sin^2\theta} + \frac{1}{n_2^2}|d_{l1}|^2 \psi_l^2 \Big[\frac{\mathrm{d}P_l^1}{\mathrm{d}\theta}\Big]^2 \Big\} \cos\theta \,\mathrm{d}\Omega \end{aligned} \tag{B.87}$$

Then, the contributions from E_θ^2 and E_ϕ can be put together:

$$\begin{aligned} &a_0^2 \int_{FRONT} \mathcal{E}_t^2 \cos\theta \,\mathrm{d}\Omega = a_0^2 \int_{FRONT} (\mathcal{E}_\theta^2 + \mathcal{E}_\phi^2) \cos\theta \,\mathrm{d}\Omega = \\ &= \frac{a_0^2}{2}\alpha^2 E_0^2 \sum_{l=1}^{\infty} \frac{2l+1}{4\pi l(l+1)} \big[n_{12}^2 |c_{l1}|^2 (\psi_l')^2 + \frac{1}{n_2^2}|d_{l1}|^2 \psi_l^2 \big] \int_{FRONT} \Big[\big(\frac{\mathrm{d}P_l^1}{\mathrm{d}\theta}\big)^2 + \frac{(P_l^1)^2}{\sin^2\theta}\Big] \cos\theta 2\pi \sin\theta \,\mathrm{d}\theta \\ &= \frac{a_0^2}{4}\alpha^2 E_0^2 \sum_{l=1}^{\infty} \frac{2l+1}{l(l+1)} \big[n_{12}^2 |c_{l1}|^2 (\psi_l')^2 + \frac{1}{n_2^2}|d_{l1}|^2 \psi_l^2 \big] \int_{\frac{\pi}{2}}^{\pi} \Big[\big(\frac{\mathrm{d}P_l^1}{\mathrm{d}\theta}\big)^2 + \frac{(P_l^1)^2}{\sin^2\theta}\Big] \cos\theta \sin\theta \,\mathrm{d}\theta. \end{aligned} \tag{B.88}$$

Here, $\psi_l = \psi_l(n_{12}\alpha)$, $n_{12} = \frac{n_1}{n_2}$ and $\alpha = k_2\frac{\omega a_0}{c}$. Also, $P_l^1(x) = -\sqrt{1-x^2}\frac{\mathrm{d}P_l(x)}{\mathrm{d}x}$. Focusing on the θ-integral gives:

$$\begin{aligned}\frac{\mathrm{d}P_l^1(\cos\theta)}{\mathrm{d}\theta} &= -\sin\theta\frac{\mathrm{d}P_l^1(\cos\theta)}{\mathrm{d}(\cos\theta)} = -\sqrt{1-x^2}\frac{\mathrm{d}P_l(x)}{\mathrm{d}x},\\ \frac{P_l^1(\cos\theta)}{\sin\theta} &= \frac{-\sqrt{1-x^2}}{\sqrt{1-x^2}}\frac{\mathrm{d}P_l^1(x)}{\mathrm{d}x} = -\frac{\mathrm{d}P_l(x)}{\mathrm{d}x}\end{aligned} \tag{B.89}$$

Since

$$\int_0^\pi \left[\Big(\frac{\mathrm{d}P_l^1}{\mathrm{d}\theta}\Big)^2 + \frac{(P_l^1)^2}{\sin^2\theta}\right]\cos\theta\sin\theta\,\mathrm{d}\theta = 0, \tag{B.90}$$

and $\int_{\frac{\pi}{2}}^{\pi} = -\int_0^{\frac{\pi}{2}}$, the integral from equation (B.88) can be written as:

$$\begin{aligned}a_0^2\int_{FRONT}\mathcal{E}_t^2\cos\theta\,\mathrm{d}\Omega = -\frac{a^2}{4}\alpha^2E_0^2\sum_{l=1}^{\infty}\frac{2l+1}{l(l+1)}\big[n_{12}^2|c_{l1}|^2(\psi_l')^2 + \frac{1}{n_2^2}|d_{l1}|^2\psi_l^2\big]\cdot\\ \cdot\int_0^1\Big[(1-x^2)\Big(\frac{\mathrm{d}P_l^1}{\mathrm{d}x}\Big)^2 + \frac{(P_l^1)^2}{1-x^2}\Big]x\,\mathrm{d}x.\end{aligned} \tag{B.91}$$

Finally, all the result for E_ϕ, E_θ and E_r and be put back into the original integral for F_{RAD} (equation (B.73)):

$$\begin{aligned}F_{RAD} &= \frac{a_0^2}{2}\epsilon_0n_2^2(n_{12}-1)\int_{FRONT}\big[\mathcal{E}_t^2 + n_{12}^2\mathcal{E}_r^2\big]\cos\theta\,\mathrm{d}\Omega\\ &= -\frac{a_0^2}{8}\epsilon_0E_0^2n_2^2(n_{12}^2-1)\sum_{l=1}^{\infty}\frac{2l+1}{l(l+1)}\Big\{\big[\alpha^2n_{12}^2|c_{l1}|^2(\psi_l')^2 + \frac{\alpha^2}{n_2^2}|d_{l1}|^2\psi_l^2\big]\cdot I_t +\\ &+ [l(l+1)]^2n_{12}^2|c_{l1}|^2\psi_l^2\cdot I_r\Big\},\end{aligned} \tag{B.92}$$

where

$$I_t = \int_0^1\Big[(1-x^2)\Big(\frac{\mathrm{d}P_l^1}{\mathrm{d}x}\Big)^2 + \frac{(P_l^1)^2}{1-x^2}\Big]x\,\mathrm{d}x, \tag{B.93}$$

$$I_r = \int_0^1(P_l^1)^2x\,\mathrm{d}x. \tag{B.94}$$

Defining the dimensionless $Q = \frac{F_{RAD}}{\epsilon_0E_0^2a_0^2}$:

$$\begin{aligned}Q = -\frac{1}{8}(n_{12}^2-1)\sum_{l=1}^{\infty}\frac{2l+1}{l(l+1)}\Big\{\big[\alpha^2n_1^2|c_{l1}|^2(\psi_l')^2 + \alpha^2|d_{l1}|^2\psi_l^2\big]\cdot I_t +\\ = [l(l+1)]^2n_1^2|c_{l1}|^2\psi_l^2\cdot I_r\Big\}\end{aligned} \tag{B.95}$$

Here, $\psi_l = \psi_l(n_{12}\alpha) = \psi_l(n_1\alpha_0)$, if α_0 is defined as $\alpha_0 = \frac{\omega a_0}{c}$. The coefficients c_{l1} and d_{l1} are given in equations (B.35) and (B.36). Q can also be expressed as

$$Q = -\frac{1}{8}(n_{12}^2 - 1)\sum_{l=1}^{\infty}\frac{2l+1}{l(l+1)}\Big\{n_1^2|c_{l1}|^2\big[\alpha^2(\psi_l')^2 I_t + \big(l(l+1)\big)^2\psi_l^2 I_r\big] + \\ + \alpha^2|d_{l1}|^2\psi_l^2 I_t\Big\}. \tag{B.96}$$

This expression is found based on two assumptions. The first assumption is that only the $l' = l$ terms are included. The second is that cross terms can be neglected.

Using the definition of α_0:

$$Q = -\frac{1}{8}(n_{12}^2 - 1)\sum_{l=1}^{\infty}\frac{2l+1}{l(l+1)}\Big\{n_1^2|c_{l1}|^2\big[n_2^2\alpha_0^2[\psi_l'(n_1\alpha_0)]^2 I_t + [l(l+1)]^2\psi_l^2(n_1\alpha_0) I_r\big] + \\ + n_2^2\alpha_0^2|d_{l1}|^2\psi_l^2(n_1\alpha_0) I_t\Big\}. \tag{B.97}$$

Also, remembering the equation from (B.8):

$$(\gamma_2 - \gamma_1)\pi a_0^2 H + (\gamma_2 - \gamma_1)\frac{2}{3}\pi a_0^3 + 2\pi a_0\sigma = \big|Q\epsilon_0 E_0^2 a_0^2\big|. \tag{B.98}$$

Bibliography

[1] A. Ashkin, *Applications of Laser Radiation Pressure*, Science, Vol. 210 no. 4474 pp. 1081-1088 (1980).

[2] A. Ashkin, *Optical Trapping and Manipulation of Neutral Particles Using Laser – A Reprint Volume with Commentaries*, World Scientific Publishing Co. Pte. Ltd., Singapore (2006).

[3] A. Casner & J.P. Delville, *Laser-sustained Liquid Bridges*, Europhys. Lett., 65 (3), pp. 337-343 (2004).

[4] E. Brasselet, R. Wunenburger & J.P. Delville, *Liquid Optical Fibres with a Multistable Core Actuated by Light Radiation Pressure*, Phys. Rev. Lett. 101, 014501 (2008).

[5] C. N. Baroud, M. R. de Saint Vincent & J. P. Delville, *An Optical Toolbox for Total Control of Droplet Microfluids*, Lab on a Chip v. 7, pp. 1029-1033, (2007).

[6] R. D. Schroll, R. Wunenberger, A. Casner, W. W. Zhang & J. P. Delville, *Liquid Transport due to Light Scattering*, Phys. Rev. Lett. 98, 133601 (2007).

[7] R. Wunenburger, B. Issenmann, E. Brasselet, C. Loussert, V. Hourtane & J. P. Delville, *Fluid Flows Driven by Light Scattering*, J. Fluid Mech., vol. 666. pp. 273-307 (2011).

[8] H. Chraibi, D. Lasseux, R. Wunenburger, E. Arquis & J. P. Delville, *Optohydrodynamics of Soft Fluid Interfaces: Optical and Viscous Nonlinear Effects*, Eur. Phys. J. E 32, pp. 43-52 (2010).

[9] F. M. White, *Fluid Mechanics*, McGraw-Hill, fifth edition, New York (2003).

[10] J. A. Stratton, *Electromagnetic Theory*, McGraw-Hill Book Company, New York (1941).

[11] D. J. Griffiths. *Introduction to Electrodynamics*, Pearson Education Inc., International third edition, San Francisco (2008).

[12] A. Casner, J.P. Delville & I. Brevik, *Asymmetric Optical Radiation Pressure Effects on Liquid Interfaces Under Intense Illumination*, J. Opt. Soc. Am., B20 2355 (2003).

[13] I. Brevik & R. Kluge, *Oscillations of a Water Droplet Illuminated by a Linearly Polarized Laser Pulse*, J. Opt. Soc. Am. B16, No. 6, June (1999).

[14] I. Brevik, *Experiments in Phenomenological Electrodynamics and the Electromagnetic Energy-Momentum Tensor*, Phys. Rep., Volume 52, Issue 2, pp. 133-201 (1973).

[15] A. Hallanger, I. Brevik, S. Haaland & R. Sollie, *Nonlinear Deformations of Liquid-Liquid Interfaces Induced by Electromagnetic Radiation Pressure*, Phys. Rev. E 71, 056601 (2005).

[16] A. Hallanger, *Non-Linear Deformations of Liquid-Liquid Interfaces Induced by Electromagnetic Radiation Pressure*, M.Sc. thesis, NTNU, Trondheim, (2003).

[17] J.P. Delville, A. Casner, R. Wunenburger & I. Brevik, *Optical Deformability of Fluid Interfaces*, physics/0407008 (2004).

[18] R. Wunenburger, A. Casner & J. P. Delville, *Light-Induced Deformation and Instability of a Liquid Interface. I. Statics*, Phys. Rev. E 73, 036314 (2006).

[19] R. Wunenburger, A. Casner & J. P. Delville, *Light-Induced Deformation and Instability of a Liquid Interface. II. Dynamics*, Phys. Rev. E 73, 036315 (2006).

[20] M. Abramowitz & I. A. Stegun, *Handbook of Mathematical Functions With Formulas, Graphs , and Mathematical Tables*, National Bureau of Standards, Applied Mathematics Series 55, tenth printing (1972).

[21] E. W. Weisstein, *Lambert W-function*, From Math-World - A Wolfram Web Resource, http://mathworld.wolfram.com/LambertW-Function.html.

[22] P. B. Brito, F. Fabiao & A. Staubyn, *Euler, Lambert, and the Lambert W Function Today*, Applied Probability Trust, The Mathematical Scientist, Issue 33.2 (2008).

[23] O. J. Birkeland & I. Brevik, *Nonlinear Laser-Induced Deformations of Liquid-Liquid Interfaces: An Optical Fiber Model*, Phys. Rev. E78, 066314 (2008).

[24] A. Casner, *Déformations, Manipulations et Instabilités D'interfaces Liquides Induites par la Pression de Radiation D'une Onde Laser*, PhD thesis, University of Bordeaux, Bordeaux, France (2001), Available at the URL address http://tel.ccsd.cnrs.fr/documents/archives0/00/00/16/37/index.html.

[25] MathWorks, *Product Documentation: bvp4c*, URL address http://www.mathworks.com/help/techdoc/ref/bvp4c.html (2011).

[26] I. Brevik, T. A. Sivertsen & E. Almaas, *Radiation Forces on an Absorbing Micrometer-sized Sphere in an Evanescent Field*, J. Opt. Soc. Am. B 20, 1739-1749 (2003).

[27] I. Brevik & E. Almaas, *Radiation Forces on a Micrometer-sized Sphere in an Evanescent Field*, J. Opt. Soc. Am. B 12, 2429-2438 (1995).

[28] J. D. Jackson, *Classical Electrodynamics*, John Wiley & Sons, Inc., 2nd edition (1975).

[29] J. D. Jackson, *Classical Electrodynamics*, John Wiley & Sons, Inc., 3rd edition (1999).